DISSERTATION

COEXISTENCE OF WEATHER RADARS AND COMMUNICATION SYSTEMS: MODEL TO IDENTIFY INTERFERING SOURCES AND MITIGATION SOLUTIONS

Submitted by
Mattia Vaccarono
Department of Electrical and Computer Engineering

In partial fulfillment of the requirements
For the Degree of Doctor of Philosophy
Colorado State University
Fort Collins, Colorado
Summer 2023

Doctoral Committee:

Advisor: Chandra V. Chandrasekar

Margaret Cheney
Anura Jayasumana
Ketul Popat

ABSTRACT

COEXISTENCE OF WEATHER RADARS AND COMMUNICATION SYSTEMS: MODEL TO IDENTIFY INTERFERING SOURCES AND MITIGATION SOLUTIONS

Electromagnetic spectrum is a finite resource. Weather radars are one of the many sources which use electromagnetic waves. The availability of spectrum bands that can be assigned to a specific user is limited. Consequently, the electromagnetic spectrum is shared by different application in the same frequency band. This is the specific case of C-band weather radars, which operate in the 5.6GHz band, sharing the same frequencies with Radio Local Area Networks, Wireless Local Area Networks and HiperLAN systems. These telecommunication systems are continuously increasing in rural areas as broadband Internet access points. The coexistence of C-band weather radar and such systems is nowadays a primary topic in the weather radar community. The amount of interference received by weather radars are affecting the data quality, especially for polarimetric observations.

Electromagnetic interference may also appear at higher frequencies, such as the X-band located around 9.3GHz. These frequencies are used by weather radars for hydrological purposes. The dense radar network deployed in Dallas Fort Worth area and the mobile radar managed by Arpa Piemonte operate at X-band and they receive interfering signals. These signals have been detected during a field measurement campaign using both the mobile weather radar and a vector signal analyzer able to perform real time analysis.

A technique to identify the likely interfering sources is discussed, which can be used by the National Regulatory Authorities or Regional Agencies, such as the Physics and Industrial Risk Department of Arpa Piemonte, Italy, in charge of the telecommunication authorization processes. The model may be applied to a telecommunication tower transmitting at the same frequency of a given radar and in case of likely interference, mitigation strategies could be set during the tower installation, i.e. changing the antenna direction or tilt.

Over the years, many RFI removal and mitigation tools have been discussed in the literature, but only few are currently implemented on operational weather radars. This work, instead, aims to implement mitigation solutions that can be implemented by National Weather Services. The electromagnetic interference may be removed at different levels: from the received signals to the processed radar products, such as reflectivity maps that are shown to general public. In order to make possible the interference removal also to those National Weather Services, or radar management services, which are not able to act on the radar signal processor to implement deeper mitigation tools, a RFI mitigation solution based on image processing is shown. This method does not require to access the radar signal processor, but it does not mitigate the effect of interference overlapped with weather echoes. Then, based on the interfering signals features, a mitigation solution has been developed. The interfering signals are removed before received signals are processed to obtain radar moments. The proposed method has been tested with good performances in clear air echoes at both C and X-bands. A study case has been selected to evaluate its performances during precipitation events. The proposed mitigation solution is applied to the received signals to remove interfering signals and to reconstruct the residual information. The radar reflectivity is computed and it is compared to the operational radar Z product. A Swiss C-band radar is selected as reference to validate the mitigation solution. The interfering signals are properly removed and the missing data in the received radar pulses are computed by smoothing from adjacent range gates and pulses. Actually, removing only the interfering signals the proposed solution is able to preserve the meteorological echoes which lead to a better estimate of the reflectivity values, especially in case of weak echoes (i.e.light rain or drizzle). The Interference to Signal Ratio (ISR) is considered the metric to quantitatively evaluate the mitigation performance as ISR difference between processed and received signals. The proposed mitigation solution can achieve up to 20dB suppression.

ACKNOWLEDGEMENTS

I would like to thank my family and the Colorado State University which gave me the opportunity of this fantastic journey. Thanks to my advisor Dr. Chandrasekar to have supported me. I'd like also to mention Dr. Renzo Bechini and Roberto Cremonini which allowed me to work with them in Turin on Arpa Piemonte weather radars. I'm grateful to Profs. Margaret Cheney, Anura Jayasumana and Ketul Popat for serving in my graduate committee. The author likes to acknowledge the various funding agencies that have supported research on this important topic over the course of the dissertation including the United States National Science Foundation, NASA and NOAA.

DEDICATION

I would like to dedicate this thesis to my two loves: my wife Federica and my son Filippo. Federica, you always believed in me: thank you for you unconditional support. I'd like also to dedicate this journey to my parents Maurilia and Albino. Thank you! Dad, I miss you.

TABLE OF CONTENTS

LIST OF TABLES

LIST OF FIGURES

Chapter 1

Introduction

Electromagnetic interference is becoming a major topic in radar community due to the increasing requests of electromagnetic spectrum allocation [3], such as for the 5G mobile networks in the United States [4]. Often radars operate in frequency bands close to, or shared with, other telecommunication systems. This is the case of C and X-band weather radars managed by Arpa Piemonte, the environmental protection agency of Piemonte region, Italy, and the ones managed by Colorado State University. The amount of interferences received by these radars are affecting the data quality, especially for polarimetric observations. In Italy, like in the most European countries, operational weather radars operate at C-band, in the 5.6GHz band, sharing the frequency band with Radio Local Area Network (RLAN) and Wireless Local Area Network. These telecommunication systems are continuously increasing in rural areas as broadband Internet access points. The coexistence of C-band weather radar and WLAN is nowadays a primary topic in the weather radar community [5]. Concerning the X-band, Arpa Piemonte manages a mobile radar operating at 9.365GHz, licensed by the Italian Ministry of Economical Development, now Ministry of Enterprises and Made in Italy.[1] This radar started to observe electromagnetic interferences, with an increasing trend, in 2014. In this work, measurements are performed to acquire data and to identify the interfering sources.

Electromagnetic spectrum is a finite, shared resource and decisions taken on allocations can have negative consequences, which can be serious for remote sensing sensor, such as weather radars. This is the case of WLAN frequency allocation in 5.6GHz band, shared with weather radars, taken at WRC-03. [2]

---

[1] In Italy, the Ministry of Economical Development, now Ministry of Enterprises and Made in Italy, is in charge of electromagnetic spectrum allocation and licensing, in compliance with the international legislation.

[2] World radiocommunication conferences (WRC), held every three to four years, have the job to review, and, if necessary, revise the Radio Regulations, the international treaty governing the use of the radio-frequency spectrum and the geostationary-satellite and non-geostationary-satellite orbits.

1.1 Problem statement

The radar transmits electromagnetic power and it measures the backscattered echo, which can depend on meteorological or non-meteorological sources of uncertainty and meteorological related factors. Among the non-meteorological sources, interference from artificial radio emitters deeply affect the quality of weather radar retrievals. The wireless/radio local area network (WLAN/RLAN) are widely used, especially in rural areas, and they operates in the same radar band. Furthermore, the deployment of 5G in unlicensed band [6], such as the 5.6GHz band, could be a serious threat to the quality of weather radars retrievals.

In literature [7], [8] and [9], several studies concerning RFIs are available, but they deal with RFIs as noise, disregarding the peculiar features that these signals may show. For operational radars, the challenge is to implement a tool to mitigate or remove RFIs which can be integrated into the operational scans without any additional processing delay.

From the radar perspective, the electromagnetic spectrum sharing with the aforementioned telecommunication towers produces a notable amount of radio interference, causing a data quality loss. An electromagnetic interference appears in radar PPIs as a ray with increasing reflectivity. Considering the C-band managed by Arpa Piemonte, Italy, in Figure 1.1, the same scans acquired in 2010 and 2014 at the lowest elevation angle are shown. Few interfering signals were received in 2010, while four years later only west sector was not affected by electromagnetic interference. At higher elevation, such as the 4.4 elevation scan shown in Figure 1.2, in 2010, no interference were received, while, in 2014, the southwest and northwest sectors were affected by electromagnetic interference.

Electromagnetic interference may produce deep impact on dual-polarization radar retrievals. In Figure 1.3 the RHI acquired on the 19^{th} of November 2018 at 13:29 UTC is shown. An electromagnetic interference is received for several elevation angles, overlapping with meteorological echoes: in the top-left plot, the uncorrected radar reflectivity shows weak weather echoes and the radar interference, visible as rays with increasing reflectivity along the ray, due to the radar range correction. The hydrometeor classification based on [10] partially identifies the nature of the

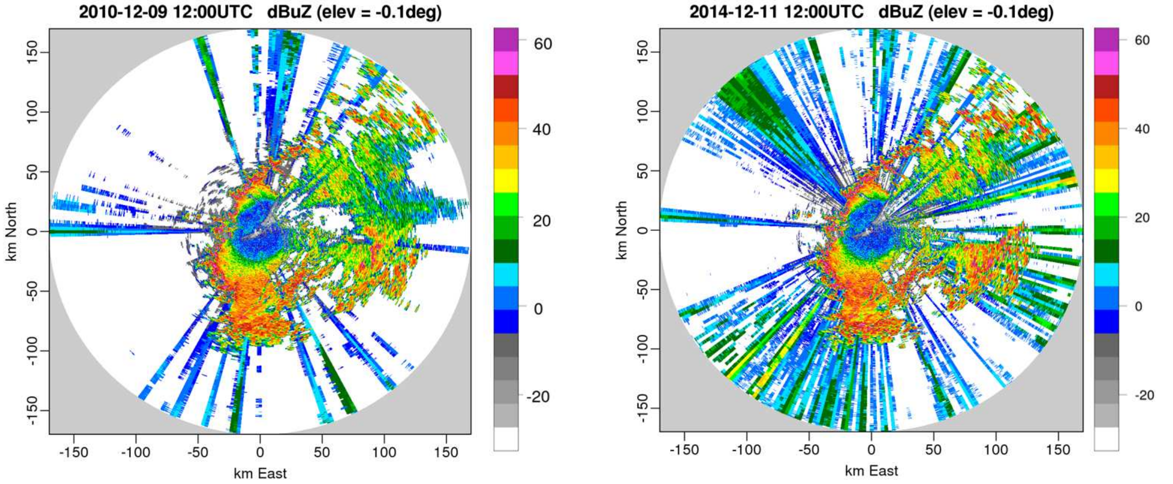
2010-12-09 12:00UTC dBuZ (elev = -0.1deg)

2014-12-11 12:00UTC dBuZ (elev = -0.1deg)

a)

b)

Figure 1.1: Uncorrected and unfiltered horizontal reflectivity Z_h acquired by Bric della Croce radar in 2010 and 2014 at the same elevation angle (-0.1°). Note the increase of electromagnetic interference visible as continuous rays.

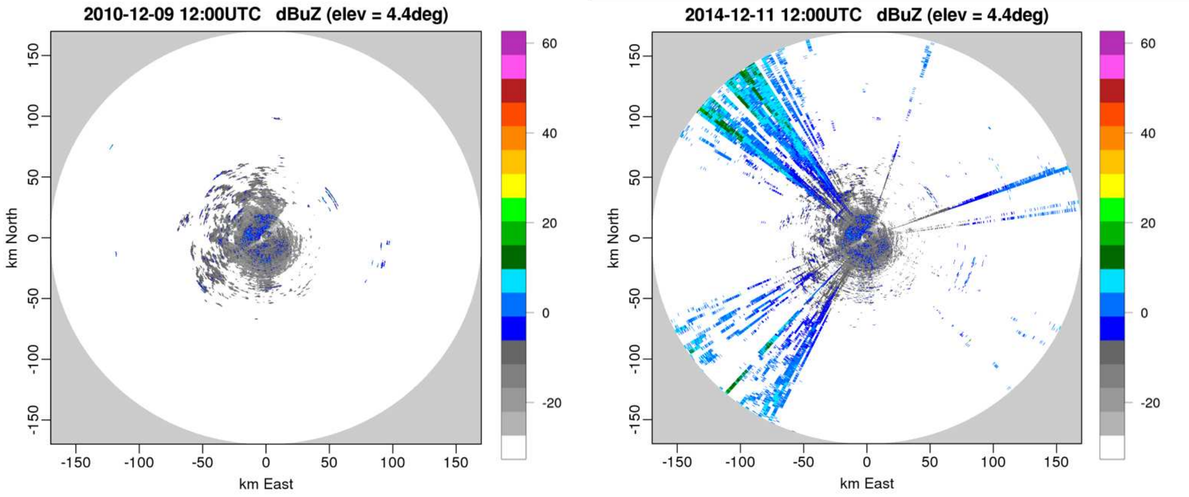
2010-12-09 12:00UTC dBuZ (elev = 4.4deg)

2014-12-11 12:00UTC dBuZ (elev = 4.4deg)

Figure 1.2: As in Figure 1.1, but at 4.4° elevation.

received echoes. The interference is recognized as clutter and those data are removed and not considered for quantitative estimations and post-processing analysis. Nevertheless, the meteorological information are removed too, causing the underestimation of the weather event, in this case drizzle and wet ice on the ground.

In Figure 1.3 bottom left plot, the differential propagation phase shift Φ_{dp} of the received echoes is shown. We can note that in a ray Φ_{dp} exceeds 150°, pointing out the RFI contamination, which is also remarkable in some rays between 10 and 30 km from the radar. Similarly, as reported in Fig 1.4, at 11:18 UTC during the RHI scan electromagnetic interference are received when the radar antenna is pointing at 162°. In this case, two interference are visible: one received for low elevation angles; one around 50° of elevation likely received in the secondary lobes of the antenna. These particular interference are not completely removed by the hydrometeor classification since their polarimetric signatures overlap with the range of values expected from weather targets such as ice particles considering the RFI received at the lowest elevation angle, we can note that the reflectivity and differential reflectivity values are close to the one in the core of the precipitation. This shows that RFI echoes may have polarimetric signatures, related to the interfering signal, similar to weather echoes, caused by electromagnetic scattering of the radar pulses, depending to the nature of the interfering source such as duty cycle, transmitted power level, modulation.

1.2 Research objectives

Over the years, many RFI removal and mitigation tools have been discussed in the literature [7], [8] and [9], but only few are currently implemented on operational weather radars. This work aims to implement mitigation solutions that can be implemented by National Weather Services. Furthermore, an algorithm to identify the likely interfering sources is discussed, which can be used by the National Regulatory Authorities or Regional Agencies, such as the Physics and Industrial Risk Department of Arpa Piemonte, in charge of the telecommunication authorization processes. The model may be applied to a telecommunication tower transmitting at the same frequency of a given radar and in case of likely interference, mitigation strategies could be set during the tower

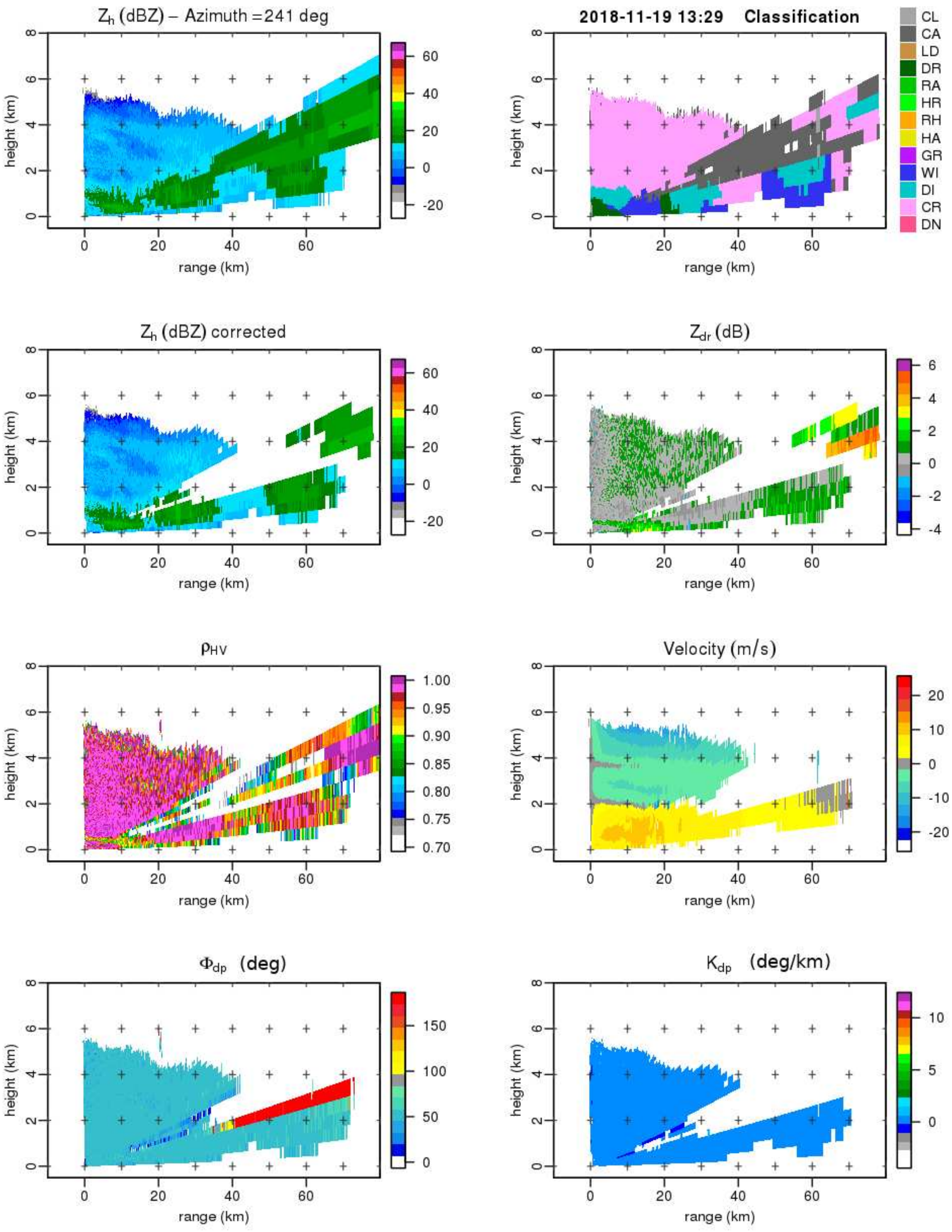

Figure 1.3: Range Height Indicator acquired on the 19^{th} of November 2018 at 13:29 UTC. From top-left, the following polarimentric observables are shown: uncorrected H-pol reflectivity, hydrometeor classification, clutter removed H-pol reflectivity, differential reflectivity, co-polar correlation coefficient, velocity, differential propagation phase and specific differential propagation phase. The electromagnetic interference, clearly visible in the uncorrected reflectivity, is removed by hydrometeor classification algorithm.

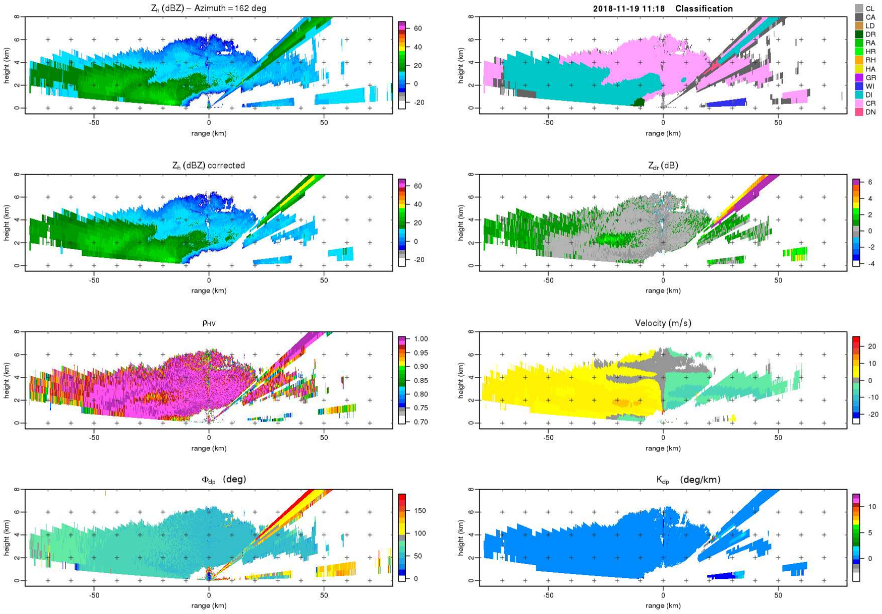

Figure 1.4: As in Figure 1.3 but at 11:18 UTC. The electromagnetic interference, clearly visible in all polarimentric observations, is not removed by hydrometeor classification algorithm.

installation, i.e. changing the antenna direction or tilt. The electromagnetic interference may be mitigated at different levels: from the raw received signals to the processed radar product, such as reflectivity maps that are shown to general public. In order to make possible the interference removal also to those National Weather Services, or radar management services, which cannot act at the radar signal processor to implement deeper mitigation tools, a mitigation solution based on image processing techniques is shown. This method does not require the access to the radar signal processor, but it does not mitigate the effect of interference overlapped with weather echoes. Then, the analysis of the feature of interfering signals and the nature of their sources is performed. Based on this, the overall goal is to implement a RFI mitigation solution to ensure the quality of data, especially in case of weak precipitation echoes. The results of this research will lead to a better reliability of the radar data and, as consequence, this will affect the systems that use the radar data in input, as Quantitative Precipitation Estimation (QPE) processing, short-time weather forecast and numerical models.

1.3 Structure of the Dissertation

To achieve the objectives listed in section 1.2, the features of the radar whose data are analyzed in this thesis are reported in Chapter 2. In Chapter 3 the spectrum sharing legislation is reported, from the International to the local level. Chapter 4 deals with the new algorithm to identify the likely interfering sources is discussed, which can be used by the National Regulatory Authorities or Regional Agencies, such as the Physics and Industrial Risk Department of Arpa Piemonte, Italy, in charge of the telecommunication authorization processes. The model may be applied to a telecommunication tower transmitting at the same frequency of a given radar and in case of likely interference, mitigation strategies could be set during the tower installation, i.e. changing the antenna direction or tilt. The aim of Chapter 5 is to discuss some procedures to retrieve those signal features which allow to identify the interfering sources. At C-band an analysis of the feature of the interfering signals has been studied for decoding the information that WLAN usually transmit, such the SSID. At X-band, instead, the interfering signals do not carry any easy to be decoded information. Thus, using a vector signal analyzer able to perform real-time analysis, the characteristic of electromagnetic interference are investigated. In Chapter 6, the procedure to remove the RFI signals from the radar product by image processing is presented. The RFI removal tool is presented in Chapter 7: the radar signal theory is reported and the IQ data at C-band and X-band are analyzed. The results of the proposed algorithm are discussed both in clear sky condition and during a selected weather event. Finally, in Chapter 8 the summary and future works of this thesis are presented.

Chapter 2

Radars overview

In the following sections an overview of the radars whose data have been acquired and analyzed in this thesis proposal is shown. C and X-band radars managed by Colorado State University and Arpa Piemonte are presented.

2.1 Colorado State University weather radars

Colorado State University is a partner of the Center for Collaborative Adaptive Sensing of the Atmosphere (CASA), established in 2003, which aims to develop the understanding of atmospheric phenomena and to establish the Distributed Collaborative Adaptive Sensing (DCAS) networks for general public safety. The DFW radar network is composed by X-band radars strategically located in the Dallas Fort Worth area, to cover the gaps in the Next-Generation Radar (NEXRAD) systems. In Figure 2.1, the X-band radar located in Addison is displayed. These X-band radars have low power, short scan range and high resolution. The collaborative network is able to optimally adjust its scanning strategies to better collect the most relevant data. Electromagnetic interferences may impact the data quality of the DFW radar network, as reported in Figure 2.2 where two interferences are received in the South West radar domain.

Furthermore, Colorado State University manages a C-band radar, Hydrological Instrument for Volumetric Observations (CSU-CHIVO). The radar is currently located near Fort Collins (CO) after have been deployed for the remote sensing of electrification, lightning, and mesoscale/microscale processes with adaptive ground observation (RELAMPAGO) field campaign [11]. Data will be acquired by this C-band radar, preliminary observations confirm the presence of RFIs affecting the radar.

Figure 2.1: Addison X-band radar

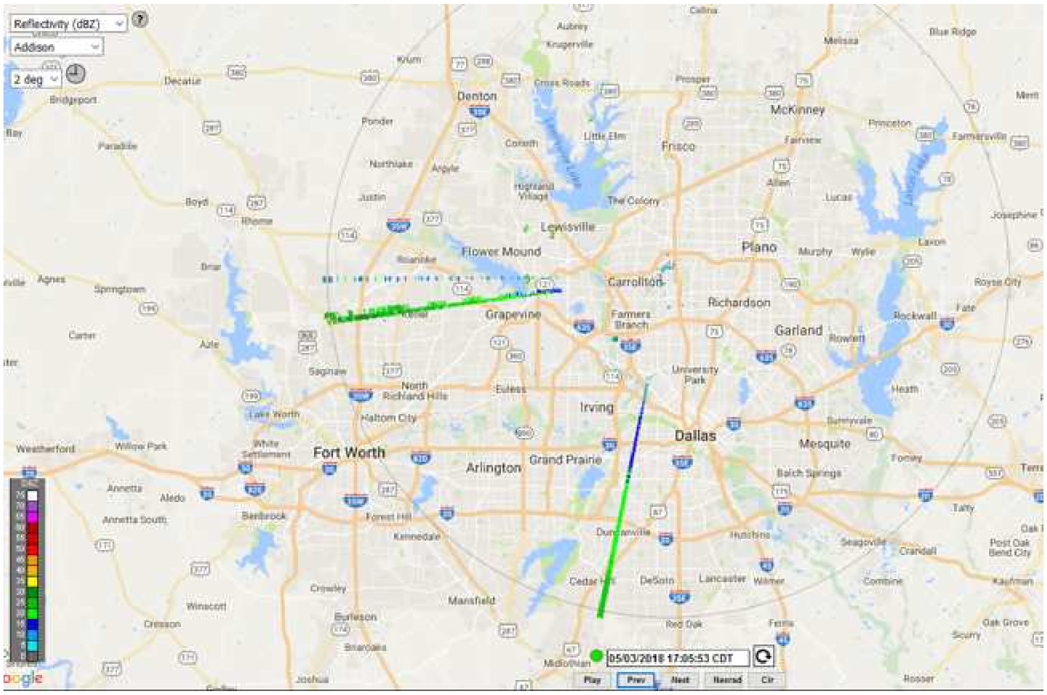

Figure 2.2: Electromagnetic interference in radar reflectivity product acquired by Addison X-band radar, US.

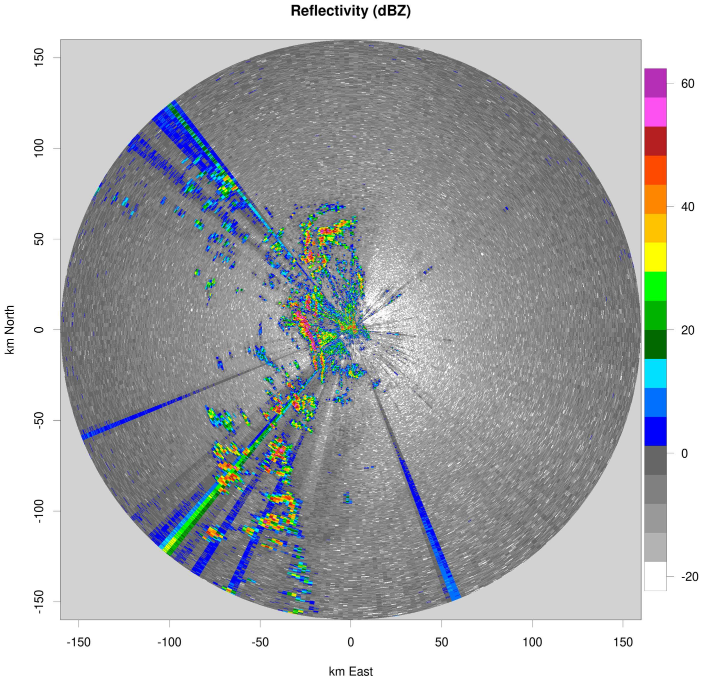

Figure 2.3: PPI of reflectivity acquired at the lowest elevation by the CSU-CHIVO radar the 6^{th} of October 2021.

2.2 Arpa Piemonte weather radars

The continuous surveillance of the territory in the North-Western regions of Italy is operated by the Regional Agency for environmental protection (Arpa) Piemonte, which owns and manages two C-band weather radars and a mobile X-band radar for research purposes. The two C-band radar are located at *Bric della Croce* hill near Turin and at *Monte Settepani* mountain near Savona (Liguria). The operational radars coverage is shown in Figure 2.4, where the red and blue markers represent the two C-band radars managed by Arpa Piemonte.

2.2.1 Bric della Croce

Bric della Croce radar is located on the hills near Turin, at 736 meters above sea level. It is placed on the top of a 33 meters height tower and covers the Piemonte region. The visibility map shows the minimum elevation required to overcome the orographic obstacles. From Figure 2.5, we can observe that the East side of the radar domain does not present obstacles that may block the radar beam, in fact the minimum elevation is less than 1°. Instead, in the Western side of the

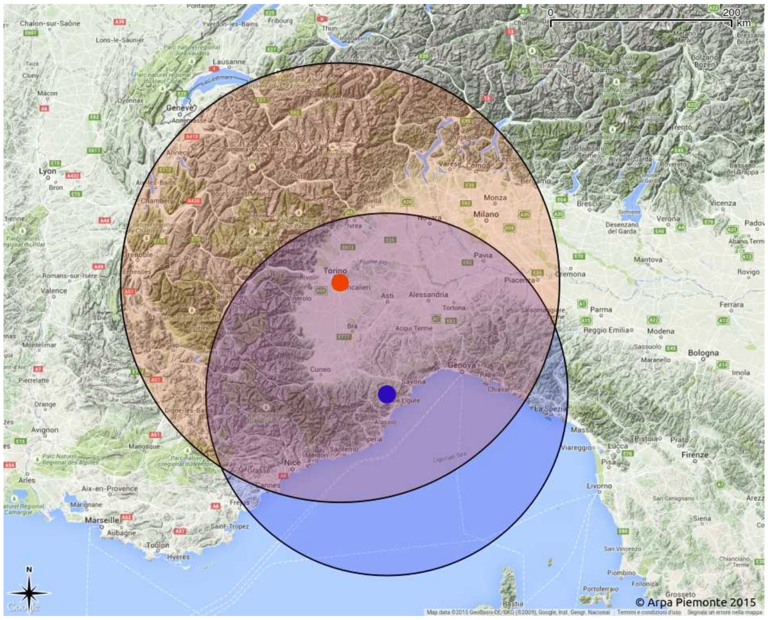

Figure 2.4: Weather radars in North-Westerner Italy. The circles correspond to the scan domains and the colors are related to the markers in the map. The circles represent the Bric della Croce scan (red) and the Monte Settepani primary scan (blue).

radar domain, the beam is partially or totally blocked by the Alps and the minimum elevation that overcomes the orography is 3°.

The radar of Bric della Croce performs two volume scans every five minutes, repeated every ten minutes. Both scans are composed by 11 elevations from -0.1° to 28.5°. The volume scans are used for quantitative measurement and the observed parameters are: radar reflectivity Z, Z_{dr}, ρ_{hv}, Φ_{dp}, k_{dp} and the Doppler velocity V. Each measure is the result of the integration of about 50 pulses. The two volume scans differ in the filters applied for the clutter removal in the radar reflectivity: in the volume scan at minute zero, no filters are applied, while, in the volume scan at minute five, clutter echoes are partially removed by a frequency domain clutter filter. The range of both volume scans is 170km and the range resolution is 340m. The angular resolution is 1°. The pulse time width is 0.5μs (short pulse). Since Bric della Croce radar operates in dual-PRF mode toenhance the unhambiguous velocity, the two alternate pulse repetition frequencies are 882 and 588 Hz.

The antenna has a 4.2m diameter and the beam width is $\sim 1°$. The antenna gain is 44.5dB and the maximum sidelobe level is -28dB. The radar transmitter is a magnetron with a frequency of 5640MHz, see Table 2.2. The peak power is 250kW.

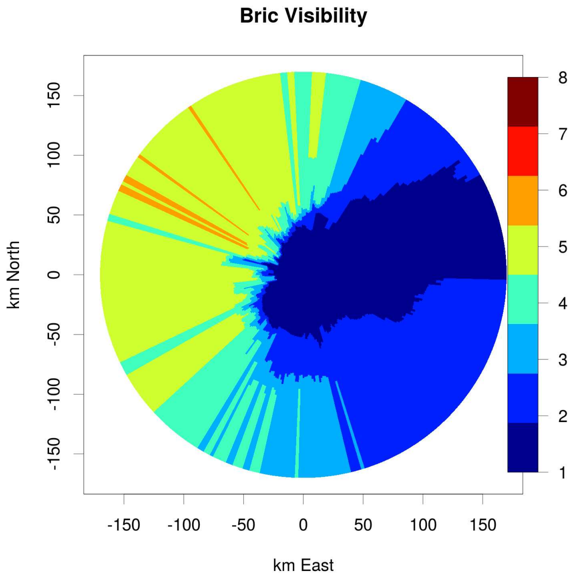

Figure 2.5: Bric della Croce visibility maps, the colors represent the minimum elevation required to overcome the orography.

2.2.2 Monte Settepani

The second C-band weather radar is located on the top of Monte Settepani mountain at 1386m asl, in the Ligurian Apennines. This radar is managed by Arpa Piemonte in collaboration with the Ligurian Region. This strategic position allows to monitor the precipitation coming from the Mediterranean sea, which may cause severe hydrological effects. Furthermore, as we can see in Figure 2.6, Monte Settepani radar has an excellent visibility in the North and East sectors, corresponding to the Pianura Padana and the mountain areas of Piemonte.

The scanning strategy of Monte Settepani radar is quite different from Bric della Croce radar. Monte Settepani radar performs two volume scans: the primary scan at minute zero, and the secondary scan at minute three. Both scans are repeated every ten minutes. The primary volume scan is used for qualitative measurement and it is a polarimetric scan. While the secondary scan, used for quantitative measurement, is not polarimetric. During the primary scan, the values of radar reflectivity Z, Z_{dr}, Φ_{dp}, ρ_{hv} and the Doppler velocity V are acquired. The primary volumetric scan is composed by seven elevations from -0.3° to 14.9°. The range is 136km and the range resolution

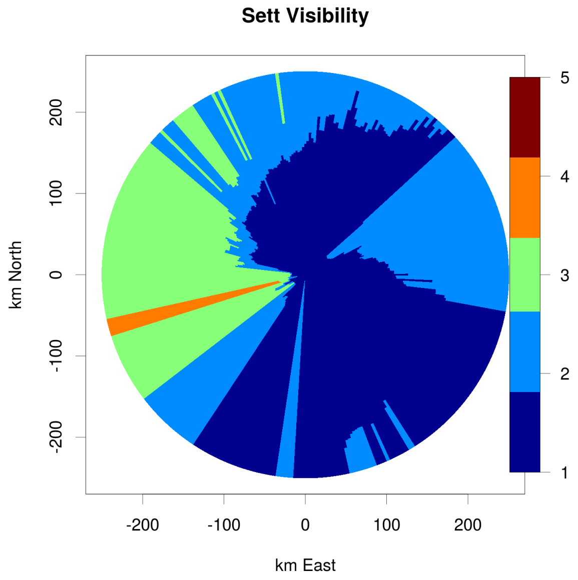

Figure 2.6: Monte Settepani visibility maps, the colors represent the minimum elevation required to overcome the orography.

is 375m, using short pulses of 0.5μs and PRF of 1090Hz. Clutter echoes are partially removed from the radar reflectivity by the digital signal processor with an IIR filter.

Monte Settpani radar uses the same antenna type as Bric della Croce radar, while the transmitter is a magnetron with operational frequency 5620MHz and peak power above 250kW. The radar is remotely controlled by the weather service of Arpa Piemonte, and the data are transmitted via a radio link.

2.2.3 Mobile X-band weather radar

The mobile X-band weather radar is a transportable compact system that can be employed for small or medium hydrological catchments monitoring, mountain area hydrological monitoring, urban hydrology and as gap filler of the national C-band radar network. The X-band radar operated by Arpa Piemonte, shown in Figure 2.7, is manufactured by Selex-SI. Respect to the C-band radar, the X-band radar has the transmitter and received mounted on the antenna, with a minimum wave guide path and without a rotary joint. This radar transmits (and receives) simultaneously both horizontal and vertical polarized signals. The antenna is smaller than that of the C-band and its

Figure 2.7: X-band mobile radar owned and managed by Arpa Piemonte, during the measurement campaign in the Alps. From Arpa Piemonte.

Table 2.1: Location of radars.

	CSU-CHIVO	**Bric della Croce**	**Monte Settepani**	**X-band**
Municipality	Fort Collins (CO)	Pecetto Torinese (TO)	Calizzano (SV)	Vercelli
Altitude	1520 m	736 m	1386 m	129 m
Latitude	40.61	45.03	44.25	45.29
Longitude	-105	7.73	8.20	8.39

diameter is large only 1.8m. The beam width is 1.3° and the antenna gain is 43dB. The transmitted peak power is 70kW, about one third of the peak power transmitted by a C-band radar.

This mobile X-band radar is currently located near Turin but during this study it was located near the tollgate of E25 in Vercelli, named Vercelli Ovest. It operated a volume scan and two vertical scans every five minutes. The volume scan is polarimetric and the radar parameters Z, Z_{dr}, Φ_{dp}, k_{dp}, ρ_{hv} and the Doppler velocity V are acquired. Two RHI are produced from the vertical scans: one along the direction 162° South with elevation ranging between 0 to 180°; the second is along 248° West with elevation between 0 and 90°. The volumetric scan is composed by 5 elevations from 3° to 15°, and a vertical scan at 89.5°. The scanning range is 80km and the range resolution is 125m, providing a high spatial resolution. The time width of the transmitted pulse is 0.5μs and the PRF is 800Hz and 1200Hz (dual-PRF mode).

Table 2.2: Technical specifications of the radars managed by Arpa Piemonte.

	Bric della Croce	**Monte Settepani**	**X-band**
Polarization	Linear H/V Simultaneous mode		
Measured parameters	Z, Z_{dr}, Φ_{dp}, k_{dp}, ρ_{hv} and V		
Antenna diameter	4.2m	4.2m	1.8m
Beam width	0.94°	0.94°	1.29°
Maximum sidelobe level	-28dB	-28dB	$<$-25dB
Antenna gain	44.5dB	44.5dB	43dB
Transmitter	Magnetron	Magnetron	Magnetron
Transmitted frequency	5640MHz	5620MHz	9370MHz
Peak power	$\simeq 250kW$	$\simeq 250kW$	$\simeq 70kW$
Pulse length	0.5, 2.0 μs	0.5, 1.5, 3.0 μs	0.5, 1.0, 2.0 μs
PRF	250$\div$ 1,200 Hz	300$\div$ 2,000 Hz	800$\div$ 1,200 Hz

Chapter 3

Spectrum sharing legislation

In Europe, most of weather radars are operating at C-bans, around 5.6 GHz, sharing the same frequency band with Radio Local Area Network and Wireless Local Area Network (RLAN and WLAN). Since the World Radiocommunication Conference in 2003 (WRC-03), the primary allocation for Wireless Access Systems WAS, including RLAN and WLAN, was set in the bands 5.150 - 5.350 and 5.4750 - 5.725 GHz [12]. Since then, weather radars and WAS are expected to coexist in the same frequency band, so this last are required to implement the Dynamic Frequency Selection (DFS) function. This algorithm should be able to detect radar signals in the WAS operating frequency. However, as reported by [5], there are several issues that affect the DFS capability to detect radar signals: first of all weather radars performs short pulses (e.g. 0.5 μs) and different Pulse Repetition Frequency (PRF), which are difficult to be detected by the DFS; then, also the radar waveform may not be the same as the one for which the DFS is certified. All these issues may cause interferences in the weather radars.

At higher frequency, such as at 9.3 GHz (X-band), no civil communications are allowed in the same frequency band of the weather radar managed by Arpa Piemonte. In this case, it likely, and it will be shown later in this paper, that the electromagnetic interference are caused by out-of-band or spurious emissions. For all telecommunication standards, spurious emission are well defined inside the standards compliance as maximum power level that a source may give at a particular frequency.

3.1 Regulation Authorities

The major activities of the existing radio spectrum regulatory framework are the allocation and assignment of radio spectrum. Radio spectrum allocation is carried out at international level, while radio spectrum assignment is a national responsibility. A frequency band is allocated when a decision is taken on the service (or services) that can be implemented by using that specific frequency

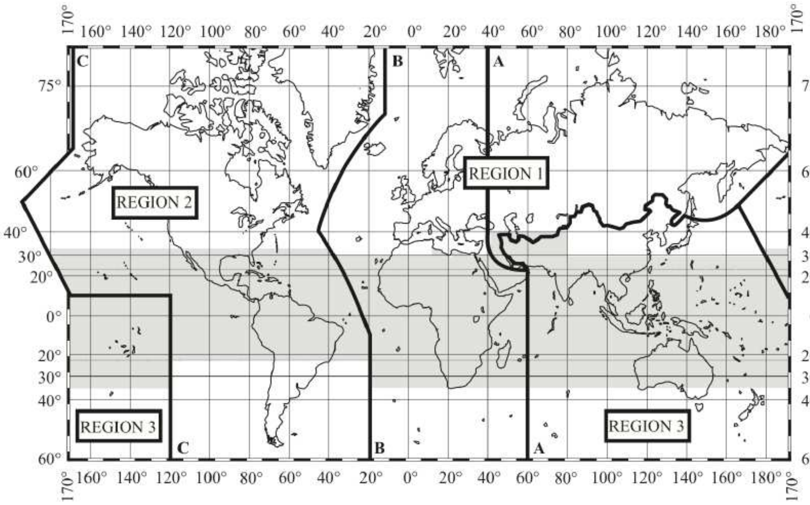

Figure 3.1: ITU Regions, from [1]

band. Each frequency band and its related service or services are indicated in the international Table of Frequency Allocations (TFA), which reports all frequency bands and related services, on a global basis [1]. Once allocated at international level, frequency bands are assigned at national level. A frequency band is assigned when service providers are granted authorisations to deliver their services over that frequency band, on a national basis [1]. Radio spectrum regulation at international level is a core responsibility of the International Telecommunication Union (ITU). The ITU is responsible for allocating radio spectrum frequency bands to radio-based services, which are set out in the TFA. National regulatory authorities (NRAs) are in charge of regulating the radio spectrum at national level. NRAs conducts assignment procedures for granting radio spectrum licences to service providers within their national territories. Radio spectrum is largely regulated at national level, the radio spectrum being a national resource [13]. Every three to four years, the ITU holds a World Radiocommunication Conference (WRC), where ITU member states discuss and revise the Radio Regulations. These are the international treaty that regulates the allocation of radio spectrum frequency bands to the various radio-based services, with mandatory effects on all ITU member states. The ITU counts 193 member states, including all EU member states. Delegations of national governments participate in WRCs and take decisions in the matter of radio spectrum allocation. Each WRC concludes with the adoption of amendments to specific portions of the Radio Regulation In the ITU Radio Regulations, the globe is conventionally divided into three regions, called ITU Region 1, Region 2 and Region 3. As shown in 3.1, Region 1 includes Europe, Africa, the Middle East, including Iraq, the former Soviet Union and Mongolia. Region 2 covers the Americas, Greenland and some of the eastern Pacific Islands; and Region comprises most of the Asian countries, which were not part of the former Soviet Union, Iran, and most of Oceania [13]. At national level, instead, National Regulation Authorities grant service providers access to the radio spectrum on a national level. NRAs can be an independent agency or part of a government ministry. NRAs assign radio spectrum rights of use by assignment procedures. In particular, radio spectrum rights of use are assigned by means of auctions, such as the right of use of N78 telecommunication band (3600-3800MHz) for the 5G New Radio mobile communications. Furthermore, there are the so-called unlicensed bands, where spectrum users can provide services without holding a licence. However, they are asked to comply with specific technical requirements so that the provision of their services is not likely to cause any harmful interference to other radio spectrum users in the same or adjacent bands. In the United States, the NRA is the Federal Communication Commission (FCC), an independent U.S. government agency overseen by Congress, which is responsible for implementing and enforcing America's communications law and regulations. In Italy, the Ministry of Enterprises and Made in Italy, is the equivalent NRA, in particular the Ministry Technical Area of Communications. The General Directorate for the communication technologies and cyber-security was established in 2019. At local level, the Territorial Inspectorates supervise and control the correct use of frequencies, the verification of the technical compliance of telecommunications systems, the identification of unauthorized systems as well as the search for methodologies techniques to optimize the use of radio channels. The collaboration between National Weather Services, or in general weather radars managers, and NRAs is a crucial matter to verify the international standards compliance of radar RFI sources.

Chapter 4

RFI sources identification algorithm

National Regulatory Authorities and regional authorities involved in the telecommunication authorization processes manage the information on the electromagnetic sources in a given area. This is the case of Arpa Piemonte, the regional environmental agency of Piemonte region, Italy, which owns and manages the database of electromagnetic sources. Following national and regional laws, radio access providers, such as mobile carriers, FM radios, TVs, RLAN, WLAN, have to transmit to the regional agency a set of features before the installation or upgrade of a specific site. The radio-electric characteristics are needed to complete the tower authorization process: transmitted power, antenna gain, polarization, antenna pattern, electric center height, antenna direction, antenna position (UTM coordinates [1]) are considered in this work. These features are a small subset of the data available in the reginal database of electromagnetic sources, which is part of the National database. In the regional database 23708 towers are available, for an overall amount of 171130 sources until June 2022.

4.0.1 Piemonte region database of electromagnetic sources

C-band weather radars share the unlicensed 5.4750 - 5.725 GHz frequency band with RLAN, WLAN and HiperLAN systems which are continuously expanding. Due to its particular orography, composed by hills and mountains, Piemonte region is experiencing a quick and continuous growth of WAS, especially HiperLAN systems shown in Figure 4.1. Nowadays, considering the data available in Arpa Piemonte database of electromagnetic sources, more than 1500 towers are currently transmitting in the same frequency band as C-band radars. In 2010, only less than 200 towers were operational (Figure 4.2). In the first semester of 2022, we can note a reduction of the increasing rate, with only 20 new installations. This phenomenon may be related to tow main

---

[1] In the UTM coordinate system a grid is used to specify locations on the surface of the Earth. The UTM system is not a single map projection but instead a series of sixty zones. Each zone is based on a specifically defined secant Transverse Mercator projection. The units for both east and north coordinates are meters.

Figure 4.1: HiperLan Tower in rural area.

factors: first, the HiperLAN network has been fully-developped in previous years; then, since last couple of years, Fixed Wireless Access communications have been pushed by mobile carriers in rural areas where wired connections are not available. FWA is implemented in the legacy frequency bands for mobile telecommunications, such as the 1800 and 2600MHz bands with LTE modulations, and in 5G bands. The evolution of 5G systems, especially in the FR2 radio spectrum, which is 26GHz, is slowing down the expansion of Internet Service Providers in the 5.6GHz band. Nevertheless, the deployment of 5G in unlicensed band [6], such as the 5.6GHz band, could expand the number of towers in the C-band, which could be a serious threat to the quality of weather radars retrievals.

These towers, whose technical information are available in the regional database of electromagnetic sources managed by Arpa Piemonte, are mainly HiperLAN systems, which provide broadband Internet access in rural areas. In recent years, a remarkable amount of wireless surveillance cameras have been deployed by municipalities. The 2010-2022 trend suggests a continuous growth

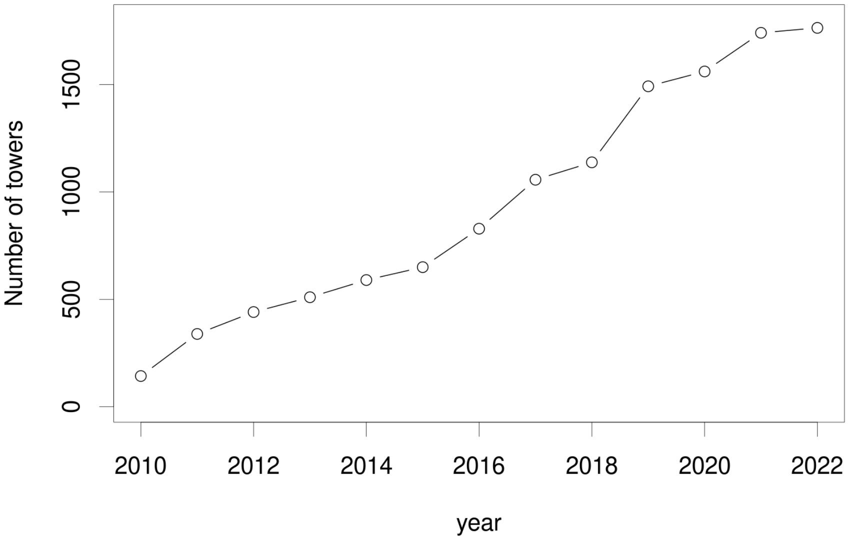

Figure 4.2: Increase of transmitting towers operating in the 5.4750 - 5.725 GHz frequency band in Piemonte region. Data available in the regional database of electromagnetic sources.

of telecommunication systems operating in the 5.4750 - 5.725 GHz. From the radar perspective, the electromagnetic spectrum sharing with those towers produces a notable amount of radio interferences, causing a data quality loss. In Figure 1.1 the same scans acquired in 2010 and 2014 at the lowest elevation angle are shown. Only few interferences were received in 2010, while four years later only West sector is not affected by electromagnetic interferences. Considering the 4.4° elevation scan (Figure 1.2), in 2010 no interferences were received, while in 2014 the South-West and North-West sectors are affected by electromagnetic interferences.

4.0.2 Algorithm to identify likely interfering sources: implementation and results

The spatial location of the towers transmitting in the 5.4750 - 5.725 GHz frequency band is displayed in Figure 4.3. It is remarkable the density of sources transmitting in the C-band around the radar site and, as consequence, some radar sectors are potentially affected by electromagnetic

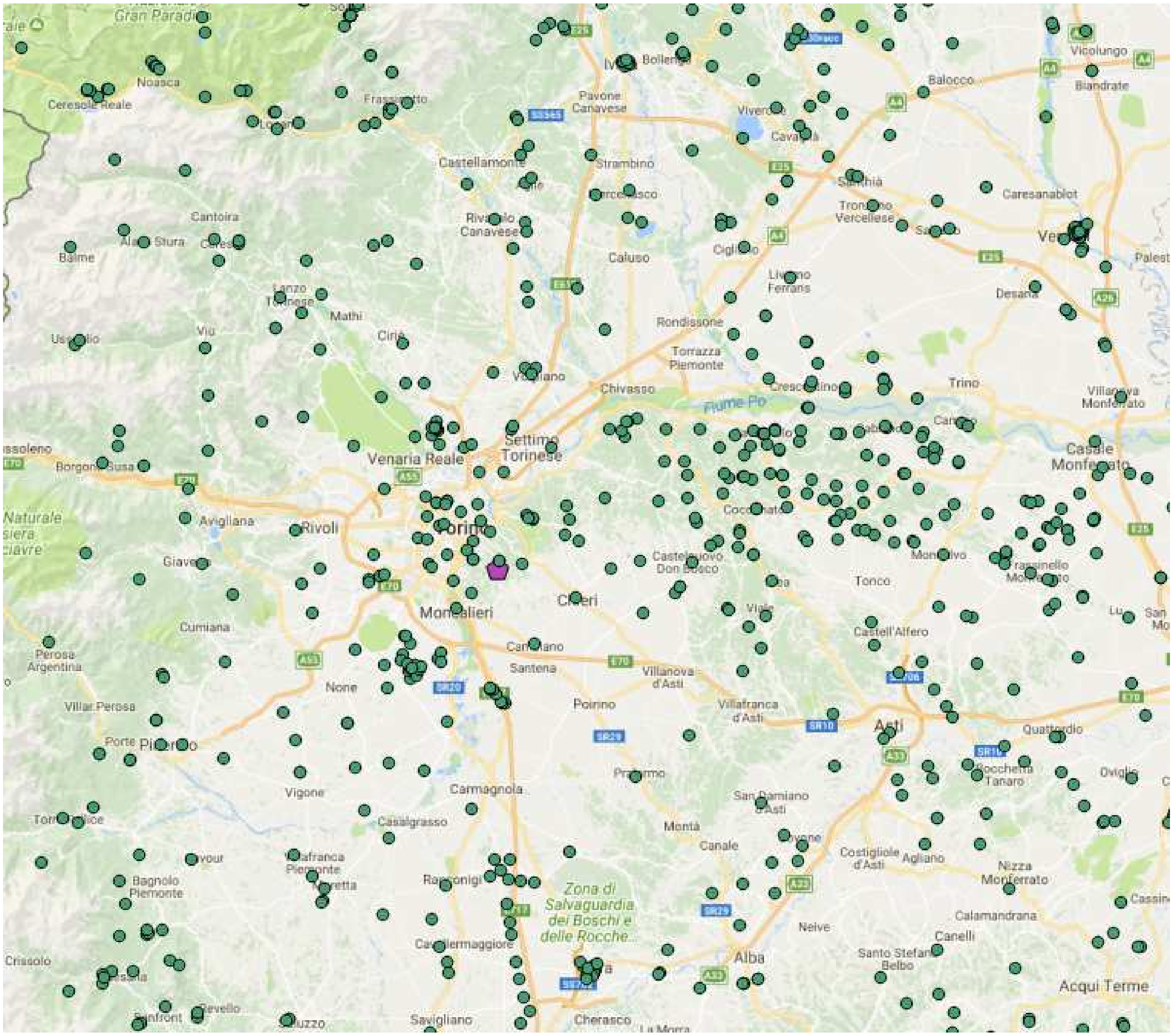

Figure 4.3: Transmitting towers (green points) operating in the 5.4750 - 5.725 GHz frequency band in Piemonte region. The violet pentagon represents the Bric della Croce radar.

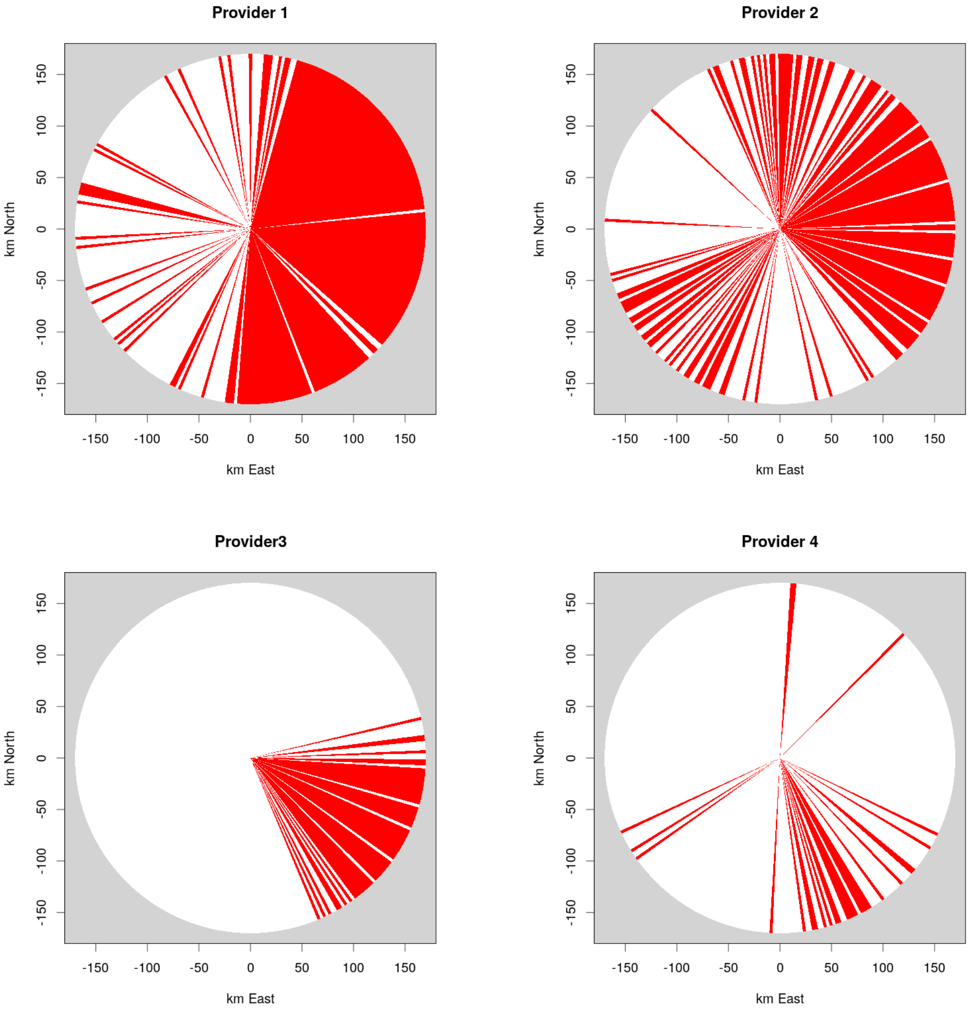

Figure 4.4: Radial directions of Bric della Croce radar likely affected by electromagnetic interferences (shown as red rays) caused by four main Internet providers in Piemonte region.

interferences. In fact, as reported in Figure 4.4 for four main HiperLAN Internet providers, the East and South sectors of Bric della Croce radar may be completely affected by interferences due to the high density of towers and to the good radar visibility in that area. However, some towers may not be in visibility from the radar site or the radar beam may not intercept some towers due to the operational scan strategy. Therefore, Arpa Piemonte and Colorado State University have implemented a model to preliminary discriminate which towers may cause interferences. The model can be useful to preliminary understand (i.e. during the authorization processes carried at local or regional level to install a given base station) if a tower, transmitting at the radar frequency band, may or not interfere with a given radar. The model is performed on the electromagnetic source database and the likely interfering towers are selected according to the following criteria:

- tower operating frequency in the 5.4750 - 5.725 GHz band;
- radar center beam intercepts tower location with 5° horizontal tolerance and 2° vertical tolerance;
- visibility between radar and tower using high resolution digital elevation model;
- tower antennas point to the radar with 5° tolerance;
- the mechanic and electrical antenna tilts of the likely interfering source point the vertical main lobe of the antenna pattern to the radar, considering the digital elevation model of the terrain.

This latest point is better shown in Figure 4.5 where the vertical antenna pattern[2] is displayed. In mountains and hills areas, usually antennas are mechanical tilted in order to reach residential areas. If the antenna has a mechanical tilt, the vertical main lobe of the antenna may not be parallel to the ground and it may be direct to the radar even if there is a considerable elevation difference.

---

[2] The antenna pattern is the graphical representation of the radiation properties of the antenna as a function of space. The antenna's pattern describes how the antenna radiates energy out into space. It is common to describe this 3D pattern with two planar patterns, called the principal plane patterns. These principal plane patterns can be obtained by making two slices through the 3D pattern through the maximum value of the pattern. It is these principal plane patterns that are commonly referred to as the antenna patterns.

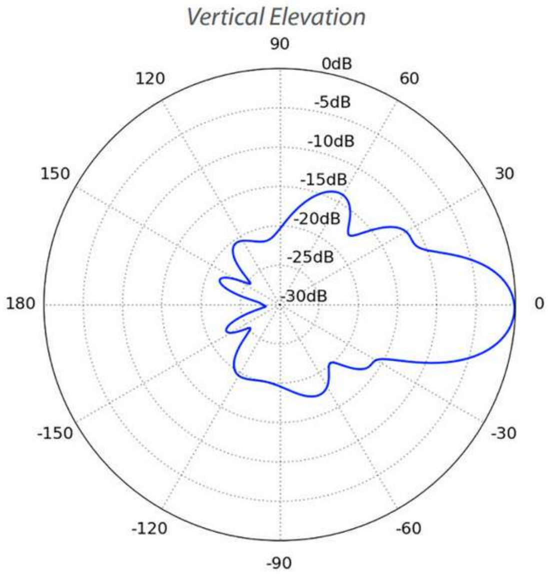

Figure 4.5: Vertical pattern of a HiperLan access point deployed by one of the ISP active in rural areas.

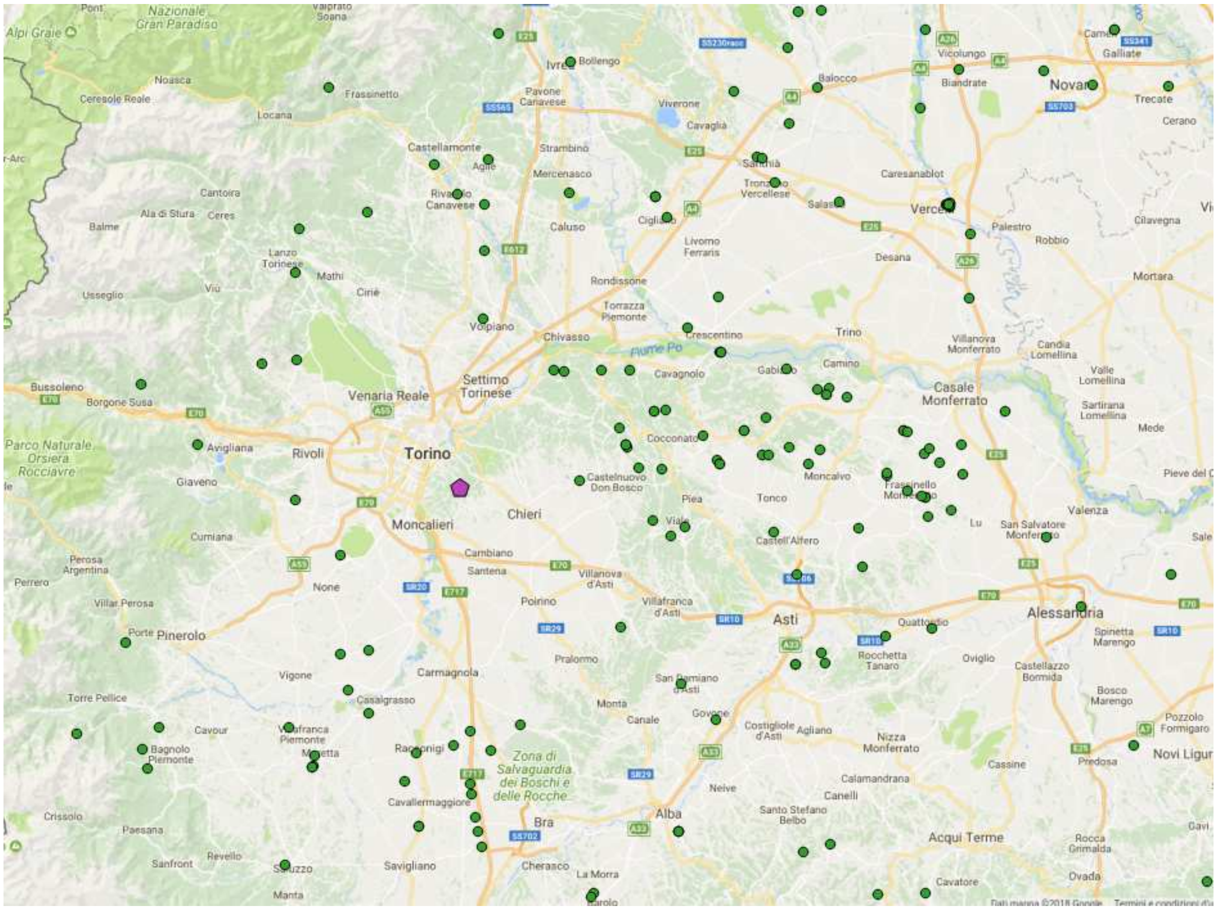

Figure 4.6: As in Figure 4.3, but the towers are filtered based on the interference model criteria.

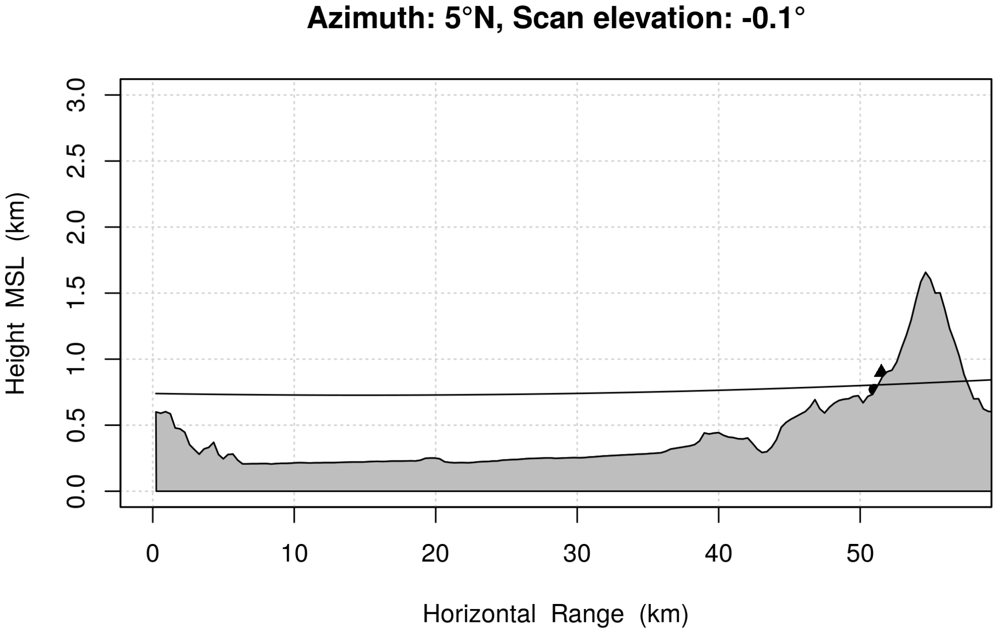

Figure 4.7: HiperLAN towers (black point and triangle) located 50 km North from Bric della Croce radar. Only the HiperLAN reported as black point was identified during in-field measurements. The radar center beam at the elevation scan of -0.1° is shown as black line, while the orography is reported as gray area.

The aforementioned thresholds have been selected according to the radar beam geometrical features. In Figure 4.6 the towers selected by the interference model are displayed. The likely interfering towers, available in the electromagnetic sources database, are about 250 in Piemonte region. The model has been validated on the data retrieved during an in-field measurement campaign. In 2015, Arpa Piemonte, in collaboration with the Italian Ministry of Economical Development, now Ministry of Enterprises and Made in Italy, made SSIDs measurements at the Bric della Croce radar to identify the interfering sources. One of the tower, which has been identified by the information reported in the SSID, is located 50 km North from Bric della Croce radar. As displayed in Figure 4.7, the radar beam at the elevation scan of -0.1° intercepts the tower site, without orography blocking. Since the tower antenna is pointing to the radar, this radial direction is affected by interference. This method is implemented by other Agencies [14] to investigate and to identify the interfering sources in their operational C-band weather radars. National Regulatory

Authorities may verify the DFS implementation in an interfering source and may take legal actions against the ISP.

Chapter 5

RFI data acquisition and analysis

The aim of this chapter is to discuss some procedures to retrieve those signal features which allow to identify the interfering sources. At C-band an analysis of the feature of the interfering signals has been performed decoding the information that WLAN usually transmit, such the SSID. At X-band, instead, the interfering signals do not carry any easy to be decoded information. Thus, using a vector signal analyzer able to perform real-time analysis, the characteristic of electromagnetic interference are investigated.

5.1 Electromagnetic interference at C-band

As previously discussed, interfering signals at C-band are mainly generated by WLAN and HiperLAN systems. This category of telecommunication systems is based on IEEE 802.11 standards, in particular 802.11a, 802.11ac (Wi-Fi 5) and 802.11ax (Wi-Fi 6) for the 5.6GHz band. According to these standards, WLANs transmit a service set identifier (SSID), which is a type of identifier that uniquely identifies a wireless local area network. Service set identifiers differentiate wireless LANs by assigning each a unique, 32-bit alphanumeric character identifier. However, there are usually multiple access points within each WLAN, and there is a way to identify those access points and their associated clients. This identifier is called a basic service set identifier (BSSID) and is included in all wireless packets. Consequently, the SSID and BSSID decoding allows to identify the specific source that generates the electromagnetic interference in a given radar.

Usually radar systems can be used to extract part of the received echoes from the wave-guide. In this way, using proper attenuation, it's possible to analyze the received echoes, in particular the interfering signals, using a Wi-Fi analyzer device connected to a computer. Such commercial devices are capable to decode the SSID and BSSID of the received WLAN signals. This procedure has been performed on the C-band weather radar managed by Arpa Piemonte, in collaboration to the NRA, which is the Ministry of Enterprises and Made in Italy. The results are reported in Figure 5.1, where the identified SSID, BSSID, antenna manufacturer name, operating frequency and signal level are shown.

Cross-checking the retrieved information on the interfering signals and the data available in the regional database of electromagnetic sources is possible to easily understand where is located the antenna that generates the interference. Often, in the SSID is reported the provider name and tower location. In addition, these information can be compared to the tower location available in the regional database. In this way, in-field investigation can be carried on in collaboration with the NRA to verify the proper DFS implementation and maximum transmitted power compliance.

5.2 Electromagnetic interference at X-band

The mobile X-band radar managed by Arpa Piemonte has been used to acquire the interfering signals. Operational and dedicated scans have been implemented to retrieve the signals features, as well as data recording. First, considering the data acquired in a single month, the impact of RFI at different elevations is investigated. In Figure 5.2, the amount of received EMI versus the scan elevation (in degree) is shown. The highest amount is received at the lowest elevation, while it decreases at second and third elevation scans. At higher elevation angles interefereces are still received since they may be collected by the antenna sidelobes.

In Figure5.3, the statistics of the amount of electromagnetic interferences is displayed by data aggregation every 15 minutes of the RFIs collected every 2 minutes. The radar was not operating from the 10^{th} morning to the 11^{th} morning, save for few hours during the day. Except for this period, it is remarkable the day-night patter of EMI affecting the X-band radar. The maximum amount of interferences, computed as 15 minutes aggregation, is achieved the 9^{th} of January at 14:15 UTC, with more than 110 EMI received by the radar. The maximum daily amount of interferences is reached during the 12^{th} of January. Histogram of RFI power, differential reflectivity and copolar correlation coefficient are shown in Figure 5.4, 5.5 and 5.6, respectively. The maximum received RFI power is -37.8dBm, while the average value is -89dBm. More than 96% of received

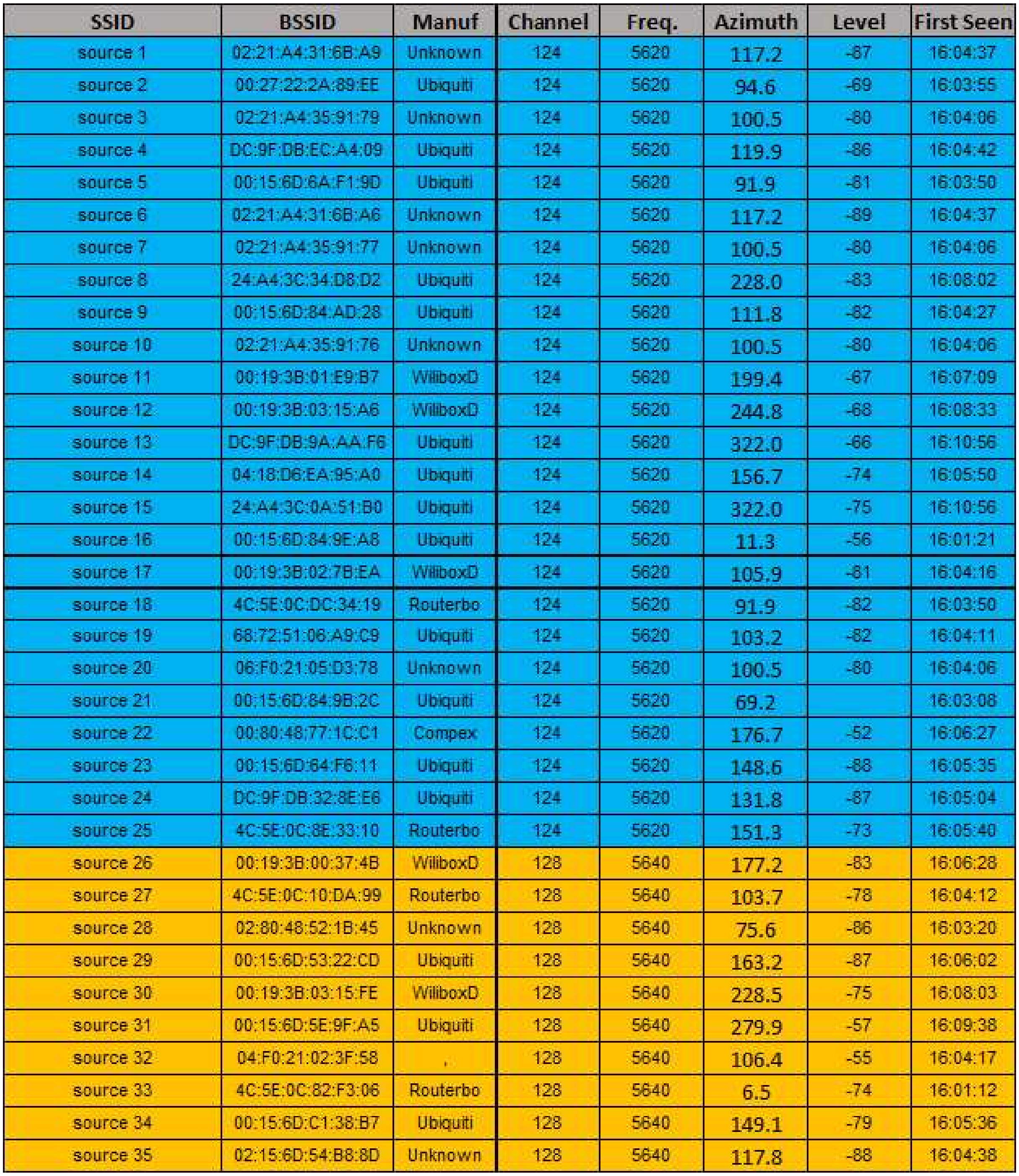

SSID	BSSID	Manuf	Channel	Freq.	Azimuth	Level	First Seen
source 1	02:21:A4:31:6B:A9	Unknown	124	5620	117.2	-87	16:04:37
source 2	00:27:22:2A:89:EE	Ubiquiti	124	5620	94.6	-69	16:03:55
source 3	02:21:A4:35:91:79	Unknown	124	5620	100.5	-80	16:04:06
source 4	DC:9F:DB:EC:A4:09	Ubiquiti	124	5620	119.9	-86	16:04:42
source 5	00:15:6D:6A:F1:9D	Ubiquiti	124	5620	91.9	-81	16:03:50
source 6	02:21:A4:31:6B:A6	Unknown	124	5620	117.2	-89	16:04:37
source 7	02:21:A4:35:91:77	Unknown	124	5620	100.5	-80	16:04:06
source 8	24:A4:3C:34:D8:D2	Ubiquiti	124	5620	228.0	-83	16:08:02
source 9	00:15:6D:84:AD:28	Ubiquiti	124	5620	111.8	-82	16:04:27
source 10	02:21:A4:35:91:76	Unknown	124	5620	100.5	-80	16:04:06
source 11	00:19:3B:01:E9:B7	WiliboxD	124	5620	199.4	-67	16:07:09
source 12	00:19:3B:03:15:A6	WiliboxD	124	5620	244.8	-68	16:08:33
source 13	DC:9F:DB:9A:AA:F6	Ubiquiti	124	5620	322.0	-66	16:10:56
source 14	04:18:D6:EA:95:A0	Ubiquiti	124	5620	156.7	-74	16:05:50
source 15	24:A4:3C:0A:51:B0	Ubiquiti	124	5620	322.0	-75	16:10:56
source 16	00:15:6D:84:9E:A8	Ubiquiti	124	5620	11.3	-56	16:01:21
source 17	00:19:3B:02:7B:EA	WiliboxD	124	5620	105.9	-81	16:04:16
source 18	4C:5E:0C:DC:34:19	Routerbo	124	5620	91.9	-82	16:03:50
source 19	68:72:51:06:A9:C9	Ubiquiti	124	5620	103.2	-82	16:04:11
source 20	06:F0:21:05:D3:78	Unknown	124	5620	100.5	-80	16:04:06
source 21	00:15:6D:84:9B:2C	Ubiquiti	124	5620	69.2		16:03:08
source 22	00:80:48:77:1C:C1	Compex	124	5620	176.7	-52	16:06:27
source 23	00:15:6D:64:F6:11	Ubiquiti	124	5620	148.6	-88	16:05:35
source 24	DC:9F:DB:32:8E:E6	Ubiquiti	124	5620	131.8	-87	16:05:04
source 25	4C:5E:0C:8E:33:10	Routerbo	124	5620	151.3	-73	16:05:40
source 26	00:19:3B:00:37:4B	WiliboxD	128	5640	177.2	-83	16:06:28
source 27	4C:5E:0C:10:DA:99	Routerbo	128	5640	103.7	-78	16:04:12
source 28	02:80:48:52:1B:45	Unknown	128	5640	75.6	-86	16:03:20
source 29	00:15:6D:53:22:CD	Ubiquiti	128	5640	163.2	-87	16:06:02
source 30	00:19:3B:03:15:FE	WiliboxD	128	5640	228.5	-75	16:08:03
source 31	00:15:6D:5E:9F:A5	Ubiquiti	128	5640	279.9	-57	16:09:38
source 32	04:F0:21:02:3F:58	,	128	5640	106.4	-55	16:04:17
source 33	4C:5E:0C:82:F3:06	Routerbo	128	5640	6.5	-74	16:01:12
source 34	00:15:6D:C1:38:B7	Ubiquiti	128	5640	149.1	-79	16:05:36
source 35	02:15:6D:54:B8:8D	Unknown	128	5640	117.8	-88	16:04:38

Figure 5.1: Identified SSID (named generically "source" to not report specific names of providers) and BSSID of interfering signals in C-band radar (channel 128). The antenna manufacturer name, operating frequency, azimuth and signal level are reported.

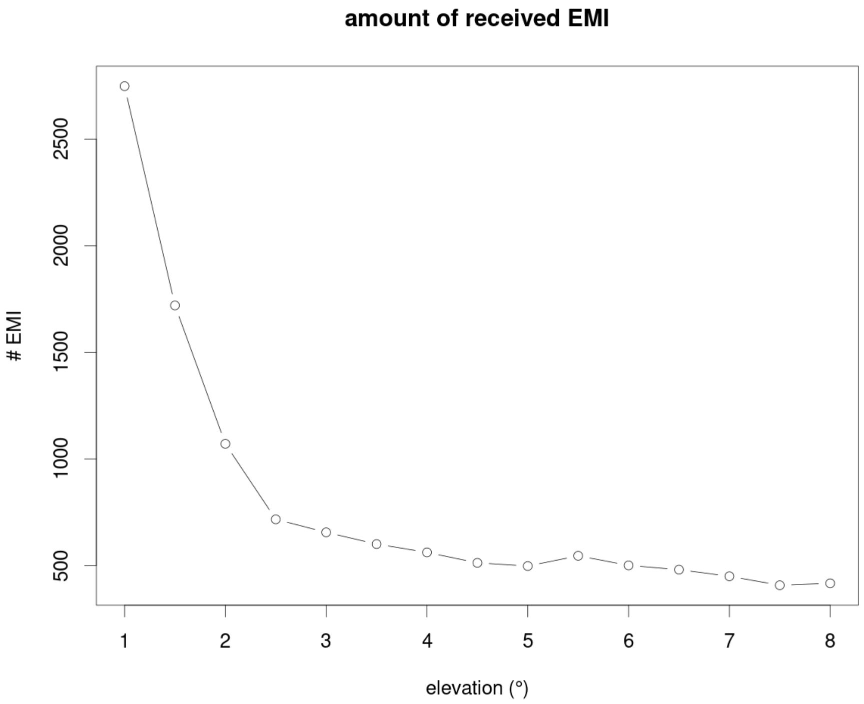

Figure 5.2: Amount of received interference versus PPI elevation.

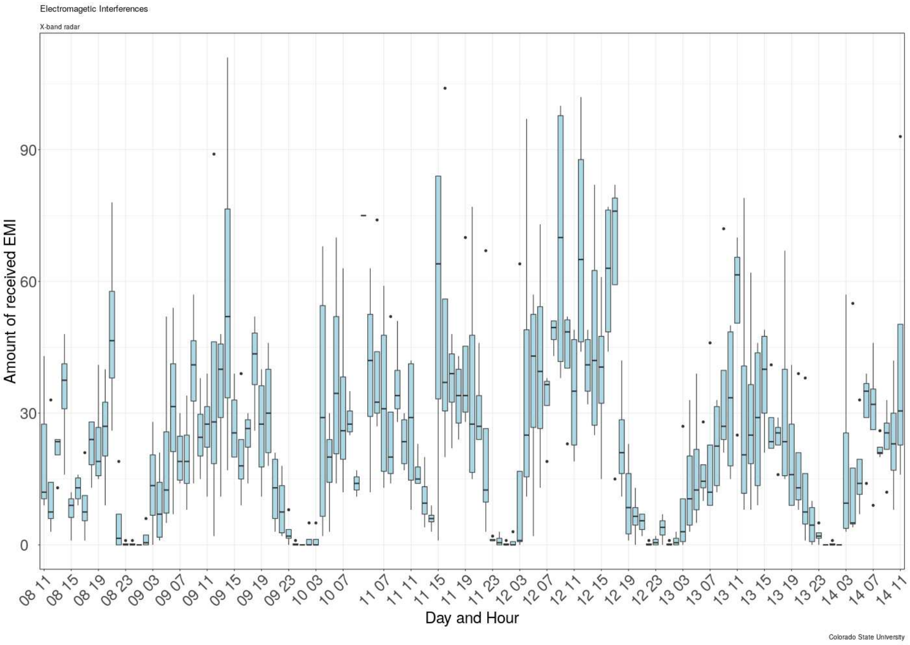

Figure 5.3: Boxplot of the electromagnetic interference amount received during the January 2019 in-field campaign. The EMI amount is aggregated every 15 minutes and the hourly average data are displayed.

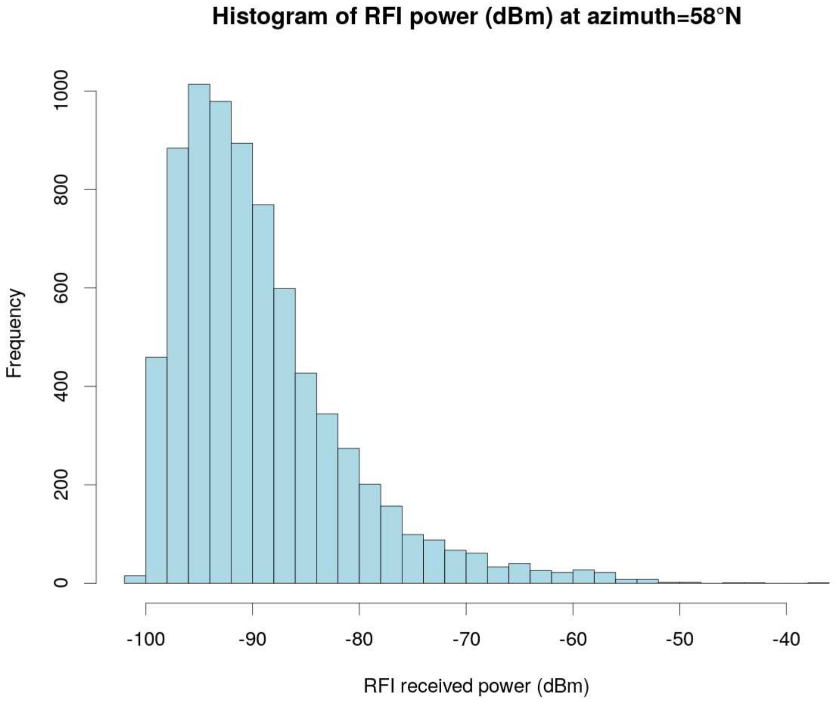

Figure 5.4: Power distribution of electromagnetic interferences based on signals received at azimuth 58°from the 8 th to the 14th of January 2019.

RFIs have power less than -80dBm. This values are likely related to the average transmitted power of the sources interfering at X-band, to their duty cycles and to their antenna patterns and distances from the radar. RFIs Z_{dr} is Gaussian distributed around 0.9dB, with few signals highly polarized. The analysis of the collected RFIs shows that approximately 80% of collected RFIs have copolar coefficient ρ_{hv} higher than 0.9, pointing out the high correlation between the two orthogonal polarizations. Thus, polarimetric signatures of RFI may not be completely distinguished from weather echoes, as previously shown.

5.3 Vector signal analyzer

The X-band radar operates at 9.37GHz with approximately 1MHz receiving bandwidth, which is suitable for weather radar retrievals but it's limited for interfering signals identification. Therefore, a Keysight's FieldFox portable analyzer is used, which is able to perform real-time analysis up to 50GHz and with up to 120MHz receiving bandwidth. FieldFox real-time analysis capture

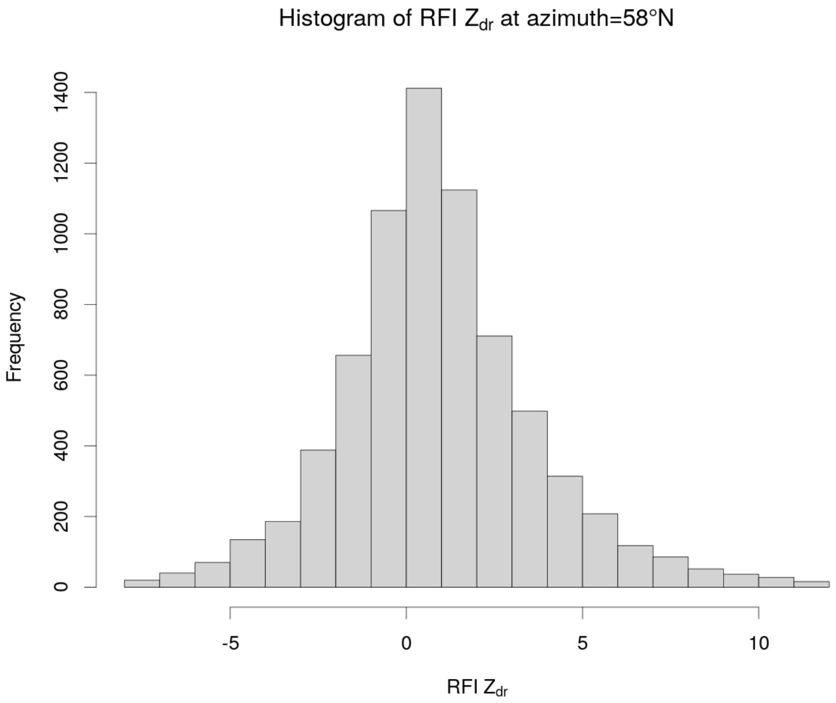

Figure 5.5: As in Figure 5.4 but for differential reflectivity.

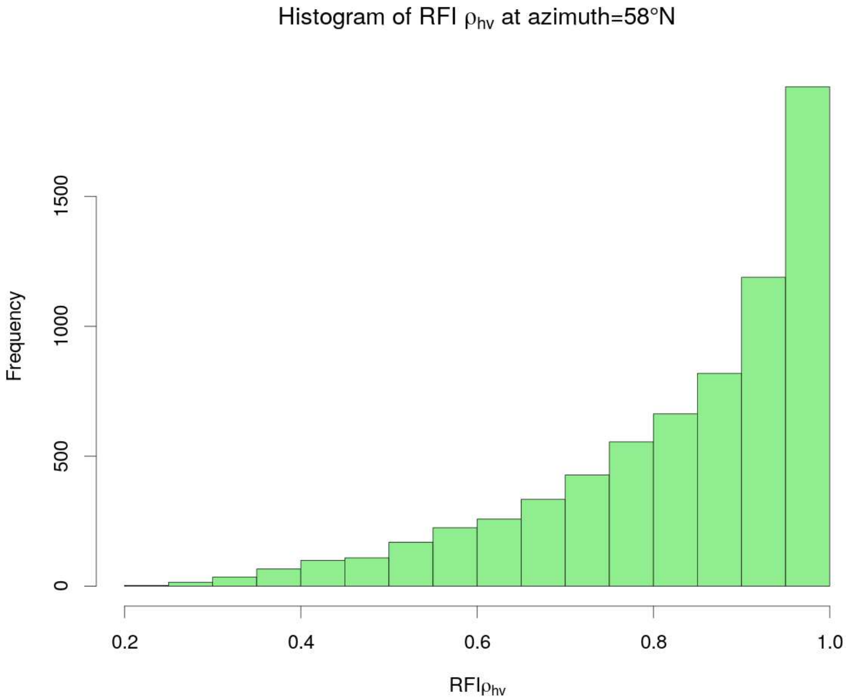

Figure 5.6: As in Figure 5.4 but for copolar correlation coefficient.

signals as short as 12μs with 100% Probability of Intercept[1] with a maximum 10 MHz real-time bandwidth and full amplitude accuracy. It is also able to visualize small signals as short as 22 ns independent of amplitude accuracy and to detect a low-level signal in the presence of a high-power transmitter using the spectrum density view. These features make the FieldFox suitable to detect the interfering signals.

During several days between February and March 2022, the FieldFox analyzer has been deployed to investigate the interfering signals features. Measurements have been collected at the radar site and in adjacent areas, especially close to logistics hub that are located hundreds meters away from the radar. Firstly, using the real-time spectrum analysis, the 100Mhz span spectrum around the radar frequency is acquired, as shown in Figure 5.7. It is visible the radar signal spectrum (black line) and the radar pulses represented by the orange pixel in the signal waterfall. The waterfall setup, however, does not allow to detect interfering signals. Moving to the spectrum density function, as displayed in Figure 5.8, the radar signal and pulses, now represented by the light blue colors of the signal persistence, are clearly observable as the interfering signals located at lower frequencies respect to the radar pulses. The signal persistence shows that the interfering signals are pulsed with a short duration.

Next, the radar has been switched off in order to better observe the interfering signals. In fact, we can note in Figure 5.9, acquired in spectrum analyzer mode, that there is a signal exactly at the radar frequency, which is 9.370GHz, other than signals at 9.35, 9.36 and 9.373GHz. During the measurements, it has been noted that those signals are impulse and some of them may not appear for minutes. So, moving back to the real-time analysis, which is shown in Figure 5.10, many signals in the 9.32-9.42GHz band are detected. In particular, the radar is interfered by the signal whose persistence is shown as a blue vertical line in Figure 5.10. Except for the signals at 9.33GHz, that will be discussed later, and the signal at 9.3715GHz, the occupied bandwidth of the signals is between 35 and 70kHz.

---

[1] A POI represents the signal duration such that there is a probability that the signal will be intercepted. In real-time spectrum analysis, many user-adjustable parameters affect probability of intercept, which is the minimum duration of a signal that can be observed and measured with 100% probability.

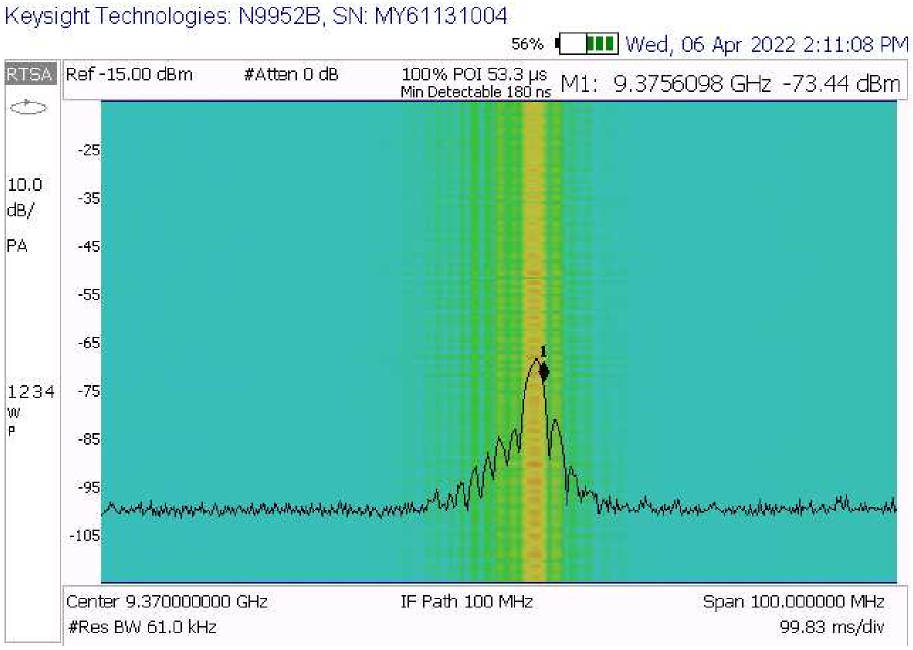
Keysight Technologies: N9952B, SN: MY61131004

56% Wed, 06 Apr 2022 2:11:08 PM

RTSA Ref -15.00 dBm #Atten 0 dB 100% POI 53.3 µs Min Detectable 180 ns M1: 9.3756098 GHz -73.44 dBm

10.0 dB/ PA

1234 W P

Center 9.370000000 GHz IF Path 100 MHz Span 100.000000 MHz

#Res BW 61.0 kHz 99.83 ms/div

Figure 5.7: Radar pulses acquired by the Keysight FieldFox Vector Spectrum Analyzer. The radar signal spectrum is shown as black line and the radar pulses are represented by the orange pixel in the signal waterfall.

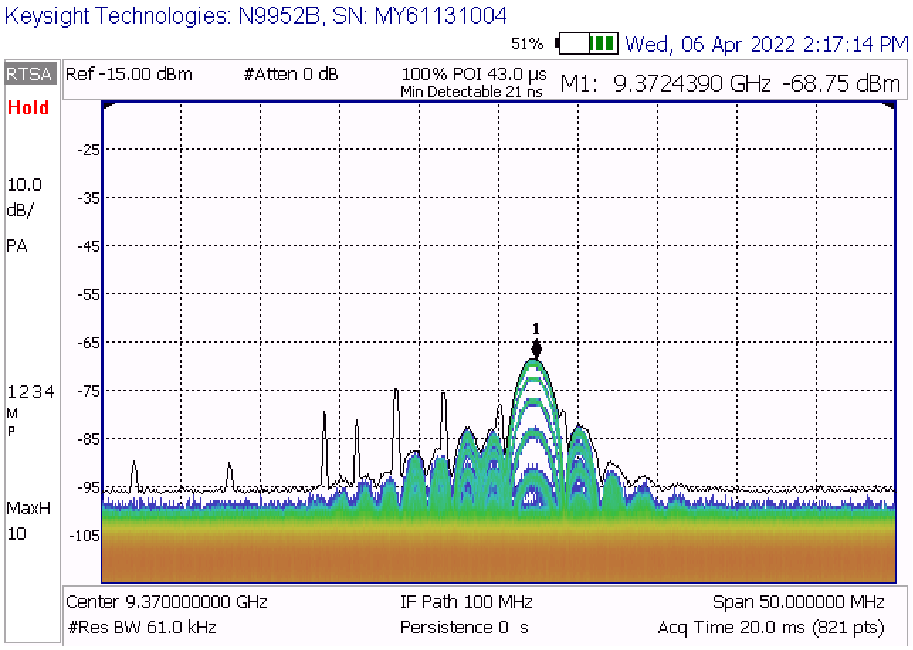
Keysight Technologies: N9952B, SN: MY61131004

51% Wed, 06 Apr 2022 2:17:14 PM

RTSA Ref -15.00 dBm #Atten 0 dB 100% POI 43.0 µs Min Detectable 21 ns M1: 9.3724390 GHz -68.75 dBm

Hold

10.0 dB/ PA

1234 M P

MaxH 10

Center 9.370000000 GHz IF Path 100 MHz Span 50.000000 MHz

#Res BW 61.0 kHz Persistence 0 s Acq Time 20.0 ms (821 pts)

Figure 5.8: Radar pulses and interfering signals in the 93.7GHz band acquired by the Keysight FieldFox Vector Spectrum Analyzer in the spectrum density mode of the real-time analysis.

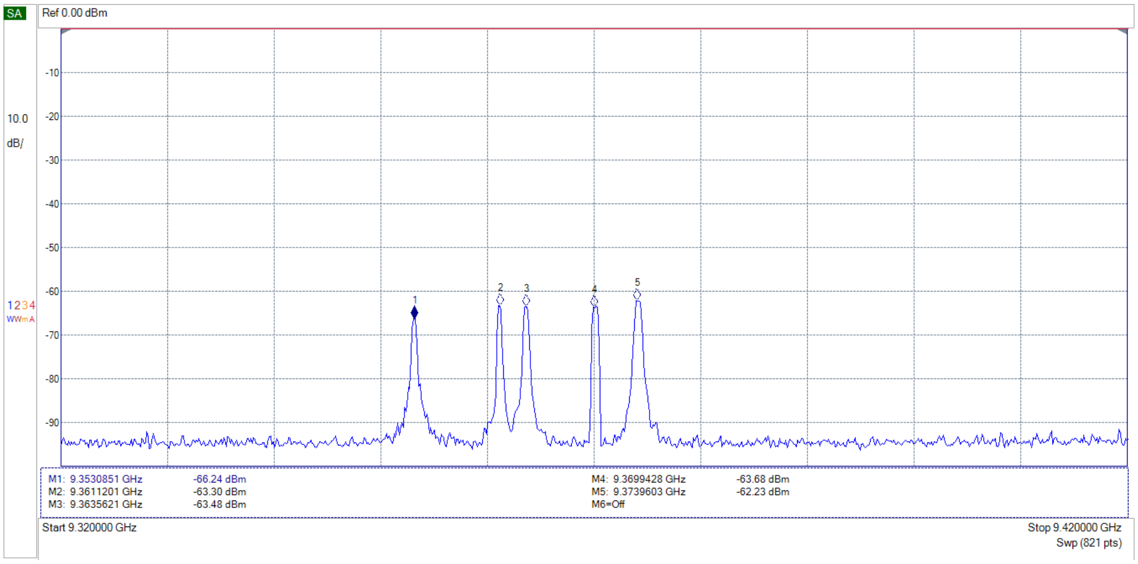

M1: 9.3530851 GHz -66.24 dBm
M2: 9.3611201 GHz -63.30 dBm
M3: 9.3635621 GHz -63.48 dBm
M4: 9.3699428 GHz -63.68 dBm
M5: 9.3739603 GHz -62.23 dBm
M6=Off

Start 9.320000 GHz
Stop 9.420000 GHz
Swp (821 pts)

Figure 5.9: Electromagnetic spectrum in the 9.37GHz band acquired by the Keysight FieldFox Vector Spectrum Analyzer. The radar was switched off during this measurement.

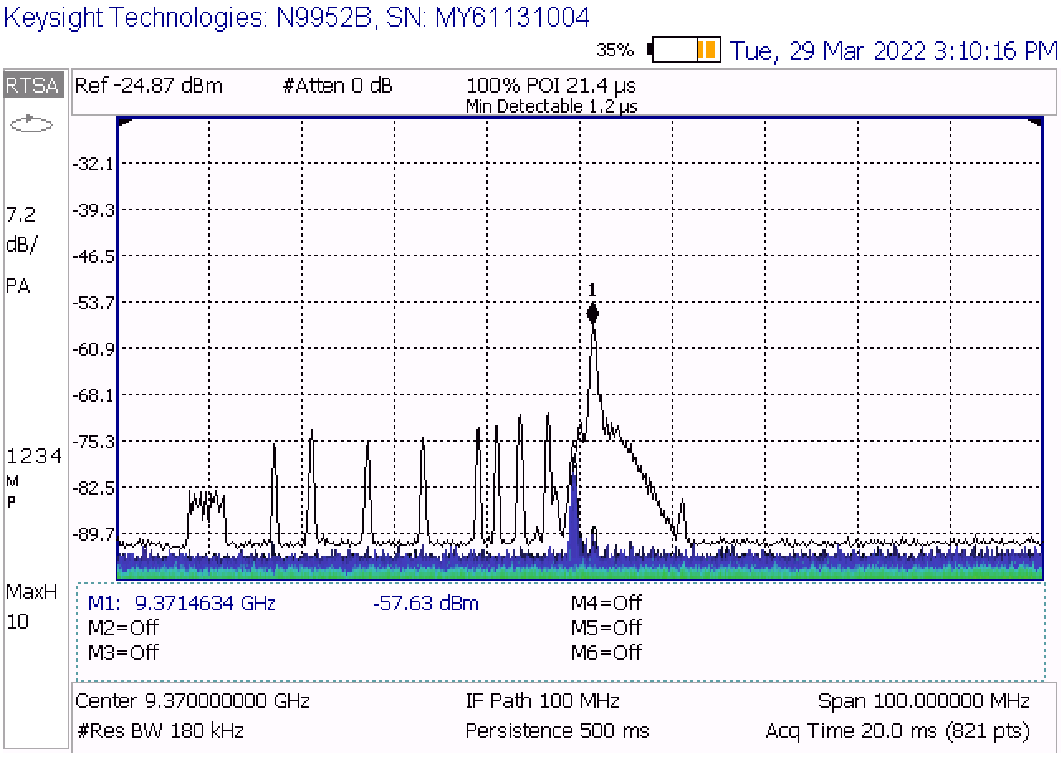

Ref -24.87 dBm #Atten 0 dB 100% POI 21.4 µs
Min Detectable 1.2 µs

M1: 9.3714634 GHz -57.63 dBm
M2=Off
M3=Off
M4=Off
M5=Off
M6=Off

Center 9.370000000 GHz IF Path 100 MHz Span 100.000000 MHz
#Res BW 180 kHz Persistence 500 ms Acq Time 20.0 ms (821 pts)

Figure 5.10: Signals at X-band detected in real-time spectrum analyzer mode. The persistent signal (vertical blue line) is received at the radar operating frequency. As in Figure 5.9, the radar was switched off.

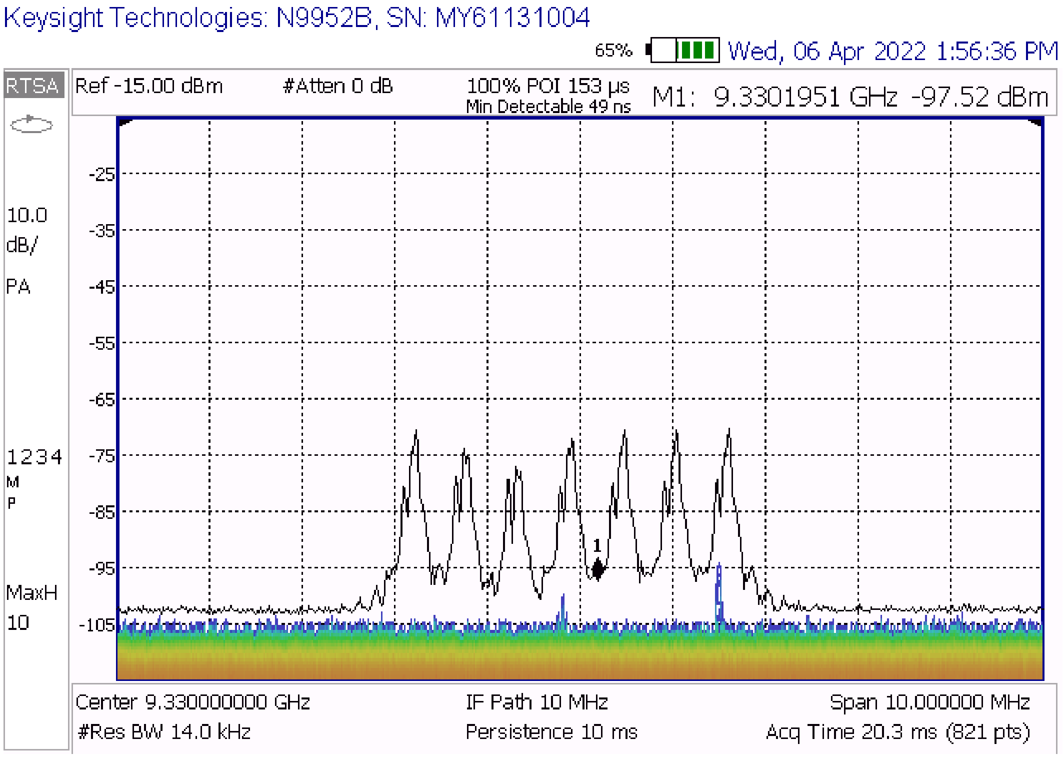

Keysight Technologies: N9952B, SN: MY61131004

65% Wed, 06 Apr 2022 1:56:36 PM

RTSA

Ref -15.00 dBm

#Atten 0 dB

100% POI 153 μs

Min Detectable 49 ns

M1: 9.3301951 GHz -97.52 dBm

10.0 dB/

PA

1234

M

P

MaxH

10

Center 9.330000000 GHz

#Res BW 14.0 kHz

IF Path 10 MHz

Persistence 10 ms

Span 10.000000 MHz

Acq Time 20.3 ms (821 pts)

Figure 5.11: Detail of the 9.33GHz signal.

Considering, instead, the signal at 9.33GHz in Figure 5.10, it may appear as a digital modulated signal with 4MHz span. This is biased by the resolution bandwidth used in the 100MHz real-time analysis, which was 180kHz, minimum RBW to obtain a 100% POI for about 20μs signals. Decreasing the real-time bandwidth from 100MHz to 10MHz around 9.33GHz, we were able to set the RBW at 14kHz, see Figure 5.11. In this case, we can note that the signal is composed by seven frequencies with span approximately 200kHz. These frequencies are not transmitted at the same time, as we can observe in the persistence color-scale, where only the fourth and seventh frequencies are persistence at the same time.

The investigation on the interfering signals was carried on to locate and identify the sources of the signal descried previously. Using the portable vector signal analyzer and a directive antenna, we moved around the radar signal along radial directions, that were identified using radar data. Due to the impulse nature of these signal we were able to identify a single signal in the 9.3GHz band. The signal, which is reported in Figure 5.12, was generated by a commercial Wi-Fi outdoor

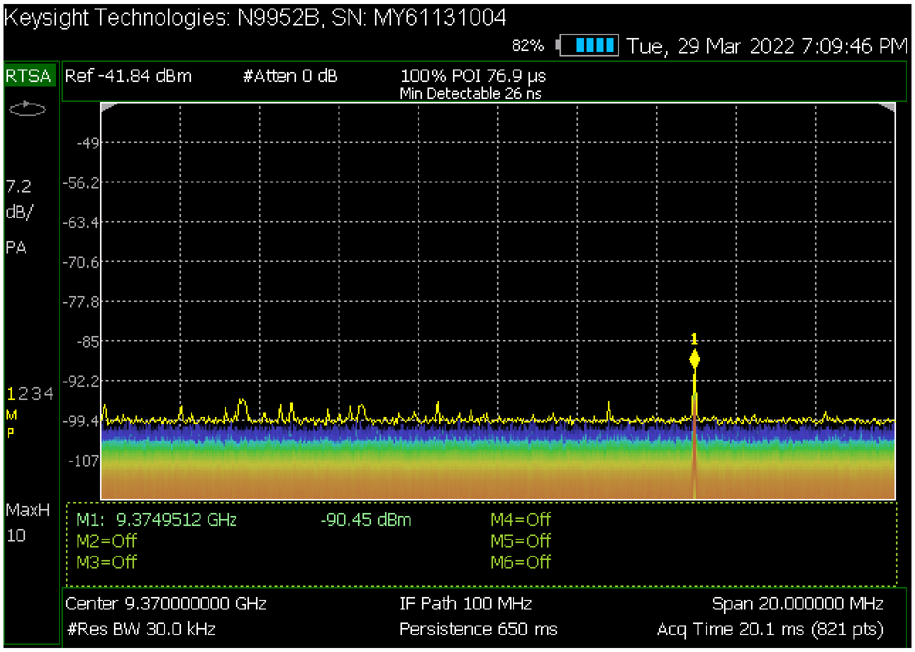

Keysight Technologies: N9952B, SN: MY61131004
82% Tue, 29 Mar 2022 7:09:46 PM
RTSA Ref -41.84 dBm #Atten 0 dB 100% POI 76.9 µs
Min Detectable 26 ns
7.2 dB/
PA
1234
M
P
MaxH
10
M1: 9.3749512 GHz -90.45 dBm M4=Off
M2=Off M5=Off
M3=Off M6=Off
Center 9.370000000 GHz IF Path 100 MHz Span 20.000000 MHz
#Res BW 30.0 kHz Persistence 650 ms Acq Time 20.1 ms (821 pts)

Figure 5.12: Interfering signal generated by a commercial Wi-Fi outdoor repeater. The source has been located and identified.

repeater operating a both 2.4GHz and 5.6GHz. The electronic components of this device emitted a constant signal at 9.375GHz. In this case, it was possible to remove the interfering source by switching off the repeater.

Since the measurements where performed in several location around the radar site, as reported in Figure 5.13, it was also possible to compare the electromagnetic spectra acquired in two locations, which are approximately 10km far. These spectra are shown in Figure 5.14, where it is remarkable that all the same signals are present in the two locations. This fact points out that the interfering sources transmit at the detected frequencies and they are distributed in a wide area.

Using the capability of the FieldFox analyzer to record the real-time data, post-elaboration of the detected signals have been performed. Since these signals are rapidly time-varying, it is not straightforward in real-time analysis to understand there is any correlation. Considering signals at 9.361, 9.366 and 9.370GHz, the received power versus time is reported in Figure 5.15, in green, red and blue colors, respectively. These signals are not transmitted at the same time during the 12s recording period. In fact, only in few case, e.g. at 8.2s, 9.7s and 13s from recording start, the three signals appear together. Computing the correlation coefficient between signals, we can affirm

Figure 5.13: Measurements location around radar site.

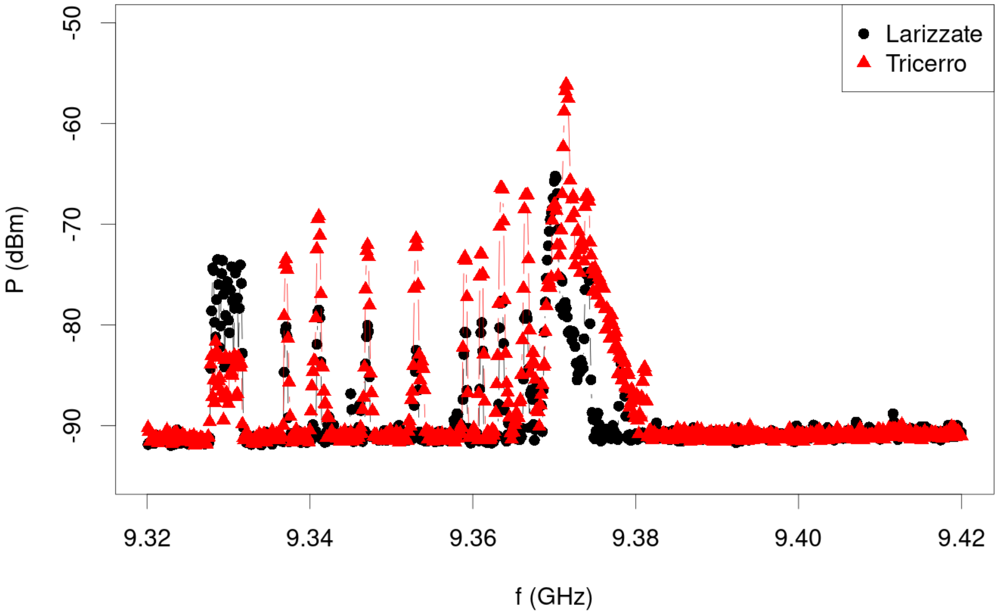

Figure 5.14: Comparison of electromagnetic spectra acquired in different locations: Larizzate (black dots) and Tricerro (red triangles), which are 10km far. Note that the frequency has been reported in Hz. To locate the two measurements areas, see Figure 5.13.

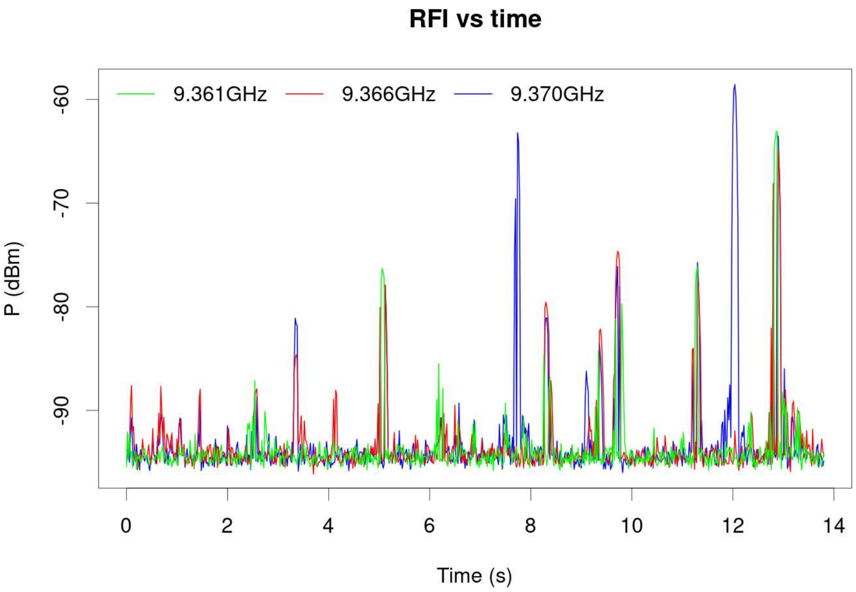

Figure 5.15: Interfering signals recorded by the Kiesight FieldFox analyzer. The power of detected signals at 9.361, 9.366 and 9.370GHz versus time is reported in green, red and blue colors, respectively.

that there is no correlation, since the maximum correlation is less than 0.5 for 9.37 and 9.366GHz signals and less than 0.01 for the other permutation. Therefore, in addition to the spatial distribution, the sources of the electromagnetic interference at X-band are also uncorrelated, meaning that are several sources transmitting at different frequencies. Further investigation will be performed in collaboration with the Ministry of Enterprises and Made in Italy to identify the sources and to verify the authorizations compliance.

Chapter 6

Image processing for radar products to identify interference

Radio frequency interferences from artificial sources often affect the quality of weather radar product displayed to general public. In order to make possible the interference removal also to those National Weather Services, or radar management services, which are not able to act on the radar signal processor to implement deeper mitigation tools, a first removal tool based on image processing is shown.

The radar signal processor considers the received radio interference as a meteorological echo and it applies the $1/R^2$ correction. Since the power of the interference is constant, the applied correction increases the reflectivity over the range. At long range distances, these interferences may exceed 10dBZ and in those sectors weak meteorological echoes are obscured by the interferences. An example of how the interferences from artificial radio source affect radars images is shown in Figure 6.1.

In order to minimize the presence of radio interferences in the radar reflectivity, RFIs are removed by image processing techniques. In B-scope images (i.e. the azimuth versus range plot), the interferences appear as horizontal straight lines with width that varies from one to five or six degrees. In the radar reference system, the interferences are received for all the range bins of a certain azimuth and the power of the interference is constant, that means the reflectivity increases along the ray.

6.1 Image processing

Image processing is any form of signal processing for which the input is an image, such as a radar image, and the output of image processing may be either an image or a set of characteristics or parameters related to the image. Most image-processing techniques involve treating the image as a

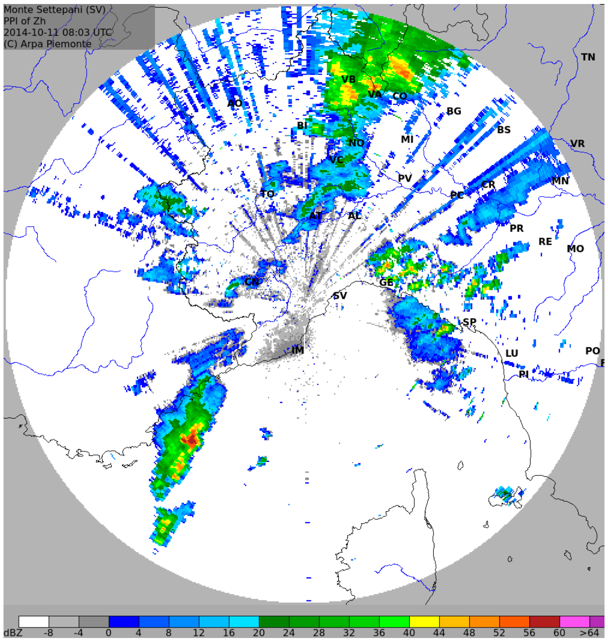

Figure 6.1: RFI and meteorological echoes in Monte Settepani PPI at 0° elevation, 11^{th} October 2014 08:03 UTC. The colors represent the radar reflectivity values.

two-dimensional signal and applying standard signal processing techniques to it. Image processing techniques have been already implemented on the interpretation of remotely sensed scenes, such as the interpretation of satellite images for city planning, flood control, agricultural production monitoring, etc. In order to remove (partially or completely) the radio interferences in the radar images, images processing techniques are performed on the secondary (non polarimetric) scans of Monte Settepani radar. The lowest elevation scan is the most affected by RFI interferences, while at higher elevations the number of radio interferences in a single PPI decreases. The B-scope radar images are processed to detected horizontal lines by using the Canny edge detector and the Hough transform [15].

6.1.1 Canny edge detector

The Canny filter is a edge detector that uses a multi-stage algorithm to detect a wide range of edges in images, it was developed by John F. Canny in 1986. Canny edge detection is a four step process, [15].

- A Gaussian filter is applied to clear any speckles and remove the noise from the image.

- A gradient operator is applied for obtaining the gradients' intensity and direction.
- Non-maximum suppression determines if the pixel is a better candidate for an edge than its neighbors.
- Hysteresis thresholding finds where edges begin and end.

The Canny edge detector is implemented in a large number of python libraries. The scikit-image Python library is used because it contains also the Hough transform. The Canny filter has three adjustable parameters: the spatial width of the Gaussian (the noisier the image, the greater the width), and the low and high threshold for the hysteresis thresholding. If we use high Gaussian width, we loose the interferences that appear in 1 azimuth or partially deleted. Therefore, the width of the Gaussian is set to one, which corresponds to one bin and one azimuth. The binary matrix containing the data is passed in input to the Canny routine and as output it returns a new matrix (image) with detected edges.

6.1.2 Hough transform

The Hough transform performs the detection of particular patterns in images, such as straight lines, circles or ellipses. An edge detector can be used as pre-processor stage to obtain image points or pixels that are on the desired curve in the image space. The simplest case of Hough transform is the detection of straight lines. In the slope-intercept model of a straight line, the straight line is described as

$$y = mx + b \tag{6.1}$$

where the m is the slope of the line and b the y-intercept.

In the parameter space, a straight line can be represented as a point of coordinates (b,m). An other representation was introduced by [16], in which the parameters are r and θ. These two values, taken in conjunction, define a polar coordinate. The parameter r represents the algebraic distance between the line and the origin, while θ is the angle of the vector orthogonal to the line and pointing toward the half upper plane. Using these parameters, the straight line can be written as:

$$y = (-\frac{cos\theta}{sin\theta})x + \frac{r}{sin\theta} \tag{6.2}$$

It is therefore possible to associate with each line of the image a pair (r,θ) which is unique if $\theta \in [0,\pi)$ and r $\in \mathbf{R}$, or if $\theta \in [0,2\pi)$ and r ≥ 0. The (r,θ) space is called Hough space for the set of straight lines in two dimensions. For an arbitrary point on the image plane with coordinates, e.g., (x0, y0), the lines that go through it are the pairs (r,θ) with

$$r(\theta) = |x_0 cos\theta - y_0 sin\theta| \tag{6.3}$$

This representation corresponds to a sinusoidal curve in the Hough space, which is unique for that point. If the curves corresponding to two points are superimposed, the location (in the Hough space) where they cross corresponds to a line (in the original image space) that passes through both points. The Probabilistic Hough Transform (PHT) is a particular upgrade of the Hough Transform, which minimize the computational requirements. In the first step of the PHT, a random subset of points is selected and a standard HT is subsequently performed on the subset. The poll size, i.e. the number of samples, is a parameter critically influencing the Probabilistic HT performance. The Probabilistic HT can be formulated as a Monte Carlo estimation of the HT. The number of iterations necessary to achieve a desired error rate is derived using the theory of Monte Carlo evaluation. Nevertheless, the poll size remains independent of the data and is based on a priori knowledge. If little is known about the detected objects, a conservative approach (poll size much larger than necessary) must be adopted, diminishing the computational advantage of the Probabilistic HT. In adaptive Probabilistic HT the termination of iterations is based on the monitoring of the polling process. The Progressive Probabilistic Hough Transform (PPHT) minimizes the computational requirements of the Hough Transform. The PPHT algorithm possesses a number of attractive properties. Firstly, a feature is detected as soon as the contents of the accumulator allows a decision. The progressive probabilistic algorithm is an anytime algorithm. It can be interrupted

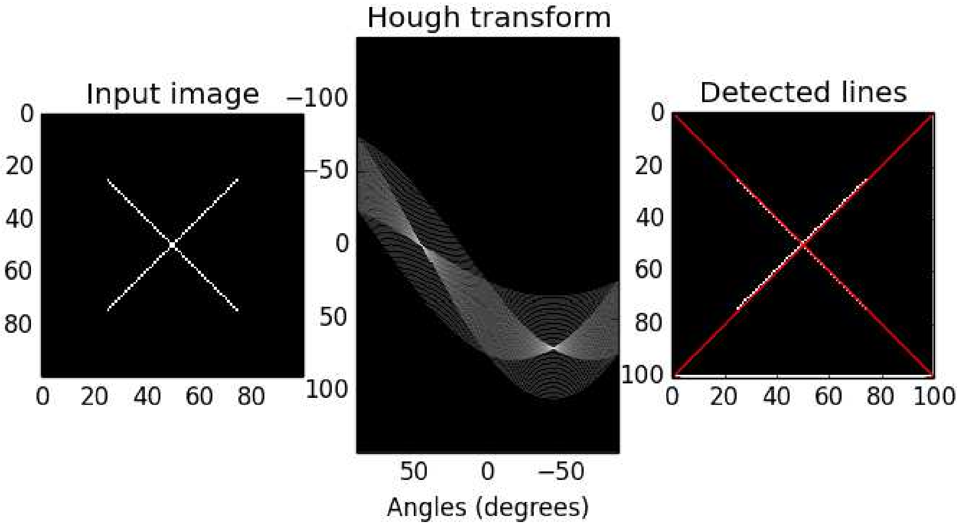

Figure 6.2: Example of Hough transform, from http://scikit-image.org/docs. The input image (left) has axis with arbitrary units. The Hough transform is applied on the input image and it is shown in the range versus angle plot, named Hough space (center). The detected lines are shown in red (right).

and still output useful results, in particular salient features that could be detected in the allowed time. The algorithm does not require a stopping rule. The computation stops when all the points either extracted or have been assigned to a feature. This does not mean that a full Hough Transform has been performed. Depending on the data, only a small fraction of points could have extracted, the rest being removed as supporting evidence for the detected features. If constraints are given e.g. in the form of minimum line length a stopping rule can be tested before selecting a point for extraction.

The scikit-image Python library has been chose since it gives as output the position (as pair x,y) of the beginning and end of the detected line. This allow us to identify horizontal lines or with 1 deg. of max tilt angle. This library contains the Progressive Probabilistic Hough Transform which returns the beginning and end of each line segment. The function *probabilistic_hough* has three parameters: a general threshold that is applied to the Hough accumulator, a minimum line length and the line gap that influences line merging. The parameters values are: default for the threshold, 25 pixels for the minimum length and 5 pixel for line gap. An example of the Hough transform is shown in Figure 6.2.

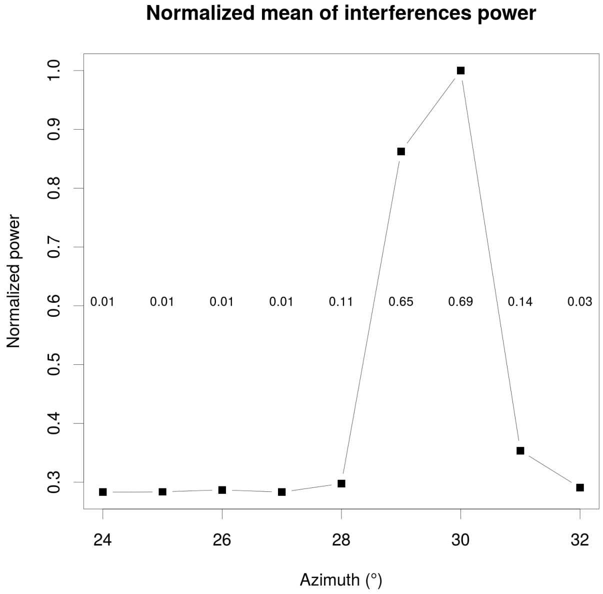

Figure 6.3: Normalized mean value of power. The image contains an interference at 30° of azimuth. The numbers in the plot displays the percentage of valid radar bins in each ray.

6.2 Moving window algorithm

In radar images, interferences may not be the only straight lines: in case of meteorological echoes, the edge of a precipitation could be detected as a straight line. The removal of the interferences should be able to understand when a RFI should not removed. For example, if there is a small convective cell superimposed to a interference, we would not remove the interference in order to maintain the information about the precipitation. Therefore it is needed to implement an algorithm able to classify the straight lines detected by the Hough transform. This method, illustrated in figures 6.3 and 6.4, is based on a azimuthal window. The window covers approximately 10° in azimuth and all the range. For each azimuthal ray in the window, the power measured by the radar is divided by the maximum value of the power data inside the window. In the following figures, the y-axis represent the normalized power in each azimuthal ray. The x-axis, instead, represents the azimuthal angle in degree at which the power is measured.

The interference shown in the image has particular characteristics: this interference affects two rays, the width of the interference is fixed by the lines found by the Hough transform; and the first

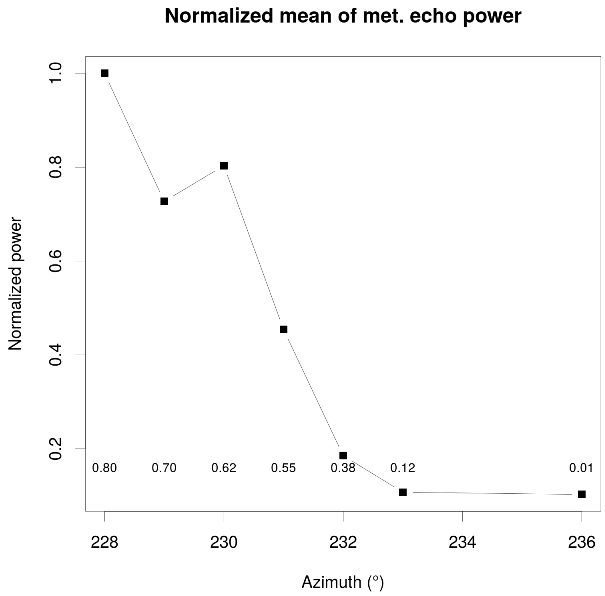

Figure 6.4: Normalized mean value of power. The image contains meteorological echoes.

azimuth before the lower edge of the interference (azimuth 29°) has normalized power about one third of the maximum power of the interference. The percentage of valid bins for each azimuth is displayed in the plot: the interference have about more the 65% of valid bins while the others azimuth have few valid bins. Analyzing the standard deviation of the power along the rays, we found that usually interference has low standard deviation (less than 5dB), although some interferences may have higher standard deviation of power due to non time constant emission of the RFI source. Thus, the standard deviation of the power along the rays is an useful method to classify the detected straight line as interference.

The normalized power of a meteorological echo is shown in Figure 6.4 where the rays from 228° to 232° degrees are recognized as straight lines by the Hough transform. This area is actually the edge of a precipitation. We can note that the patter of the normalized power is not symmetric as it was for the interference. The value of the normalized power decreases in this range of azimuths and the percentage of valid bins is higher than in the case of an interference. The standard deviation of power in case of precipitation is higher than in case of interferences.

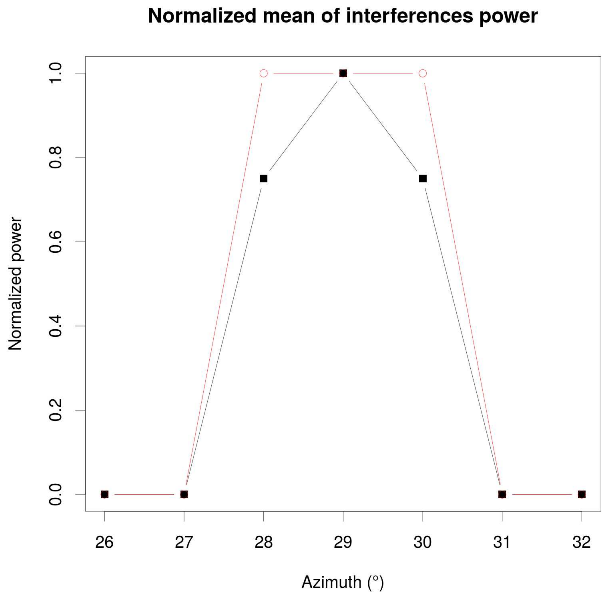

Figure 6.5: The theoretical normalized power (red line) is compared to the interference normalized power (black line) inside the azimuthal window.

The moving window algorithm is performed as reported in Figure 6.5: the rays between the edges of the interference, detected by the Hough transform, should have normalized power approximately one (red line). This theoretical pattern is compared to the measured normalized power (black points) and, if certain constraints are valid, the rays are flagged as interferences. The criteria that the interference should respect are:

- The first azimuth below and above the edge of the supposed interference should have mean power below 3/10 of the maximum of mean power inside the window.
- The mean power of azimuth inside the window should not exceed 10^{-9}W, because rarely interferences have higher power while the meteorological echoes may exceed this value.
- The standard deviation of rays inside the window should be less than 5dB.

6.3 Standard deviation in image texture

The procedure described above is repeated two times (with different thresholds) for a better detection of interferences affecting the second half of the radar range to avoid clutter echoes and

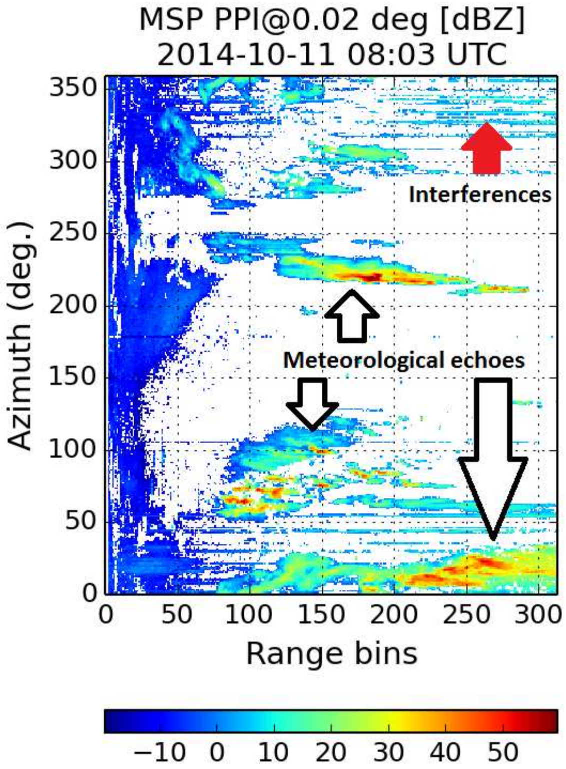

(a) B-scope plot at 0° of reflectivity measured by Monte Settpani radar, 11^{th} October 2014 08:03 UTC.

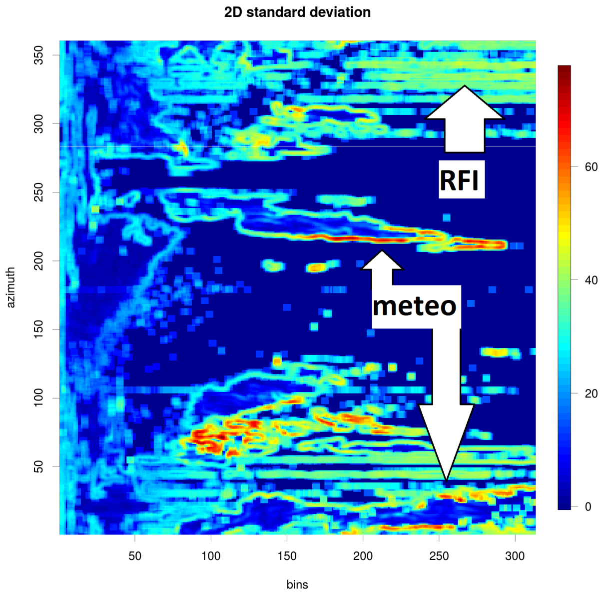

(b) 2-D standard deviation in image texture. The colors represent the value of the standard deviation, the x-axis is the range along the beam and the y-axis the azimuth.

Figure 6.6: Raw data and 2D standard deviation in the image texture.

to overshoot clouds. To remove the interferences also in the first half of the radar range, without lose information about meteorological echoes, the standard deviation in the image texture is investigated. For each pixel in the image, the standard deviation in a square of 5 bins X 5 azimuth centered on the pixel is computed. An example of the standard deviation in the image texture is shown in Figure 6.6b, where the colors represent the value of the standard deviation.

We can note that the interferences (straight line in the image) have value of standard deviation above 15dBZ, while the precipitation (localized near the radar) has standard deviation of less than 10dBZ due to the uniformity in range and azimuth. Hence each ray, detected as interference in the second half of the radar range, is analyzed from the farther portion of the radar range toward the radar (with decreasing range). For each pixel of the ray the 2-D standard deviation is compared to the reference threshold of 10dBZ, if it is greater, the pixel is recognized as part of the interference.

6.4 Results

The proposed method for the interference removal is applied to the reflectivity product of Monte Settepani radar of 11^{th} November 2014, 08:03 UTC. At the lowest elevation, as we can see in Figure 6.6a, intense precipitation are localized in N-NNE, SW and convective cells are visible in over the East sector (azimuth 0÷100°). Instead, interferences are clearly visible in NW and NE region.

In Figure 6.7, the interferences are detected and flagged with red color in the image. We can observe that the algorithm acts properly because it is able to detect interferences near the precipitation and it does not delete the meteorological echoes. Interferences are detected at about 50° and between 300° and 350°. The interference located at about 100° is not detected since there are precipitation echoes in the range sector between 150 and 200 range bins.

The result of the proposed procedure during clear sky condition is reported in Figure 6.8. The raw and processed radar products are compared. The image processing is able to detect and remove a remarkable amount of interferences.

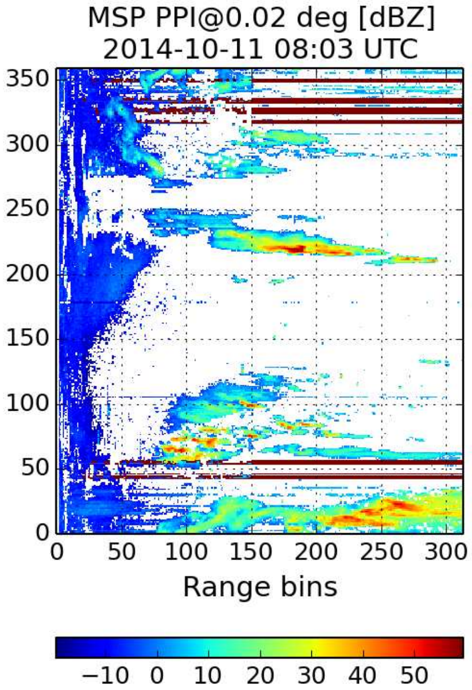

Figure 6.7: The interferences removal is performed on the reflectivity data in Figure 6.6a by the image processing algorithm. The detected interferences are flagged with red color. The colors show the reflectivity values.

In Figure 6.9 the comparison between the raw and processed radar product is shown. The image processing removes the interferences where there is no precipitation although some interferences are not removed because overlapping with precipitation echoes.

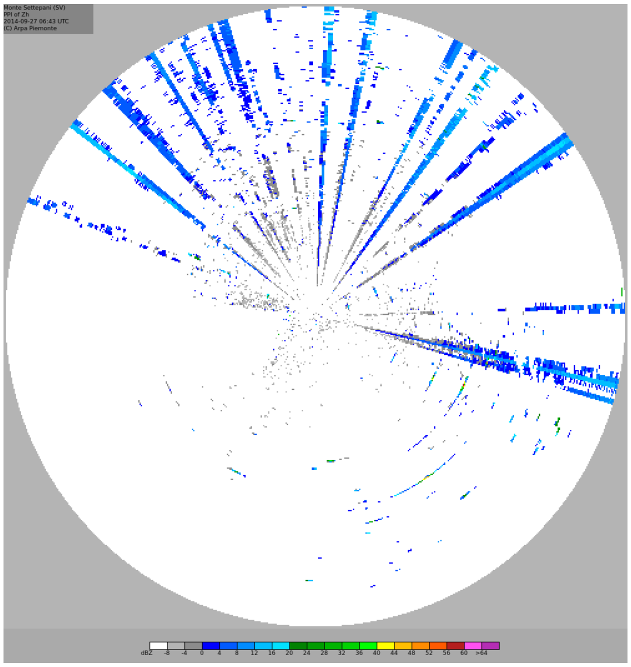

(a) PPI of Monte Settepani radar reflectivity at 0°, 27th September 2014.

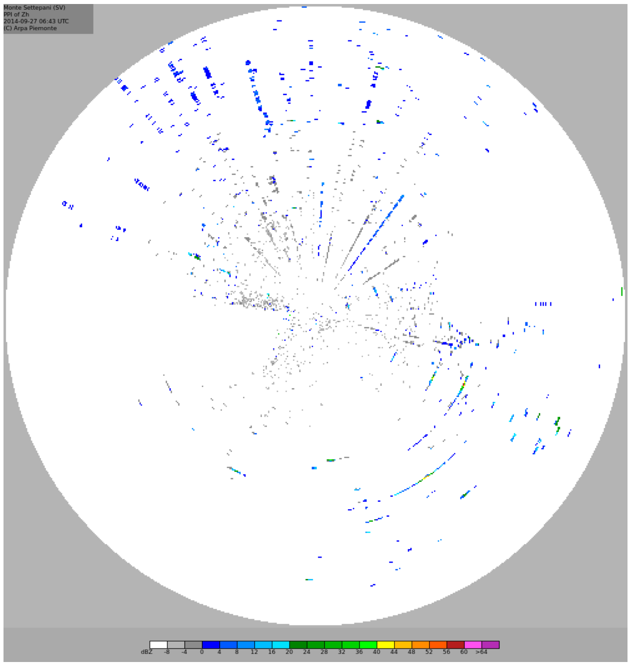

(b) Result of the implemented method with image processing on the same PPI.

Figure 6.8: Comparisons between the Monte Settepani raw (a) and processed (b) reflectivity products in clear sky conditions.

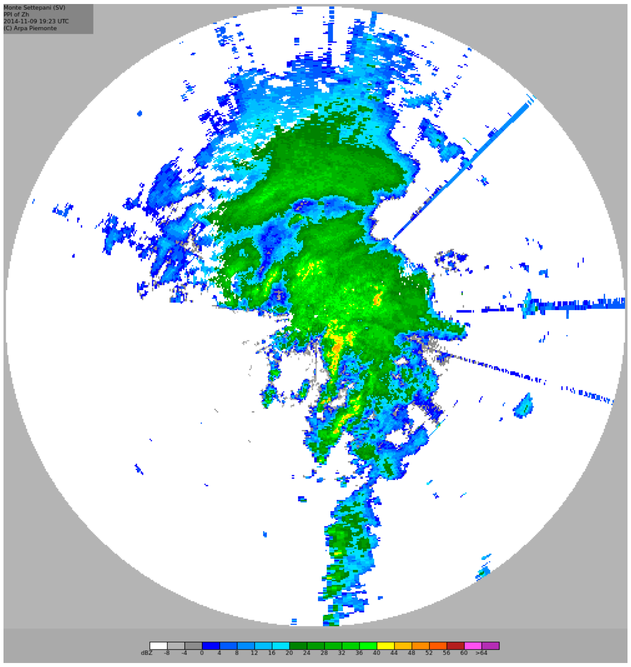

(a) PPI of Monte Settepani radar reflectivity at 0°, 9^{th} November 2014. RFI mainly eastward.

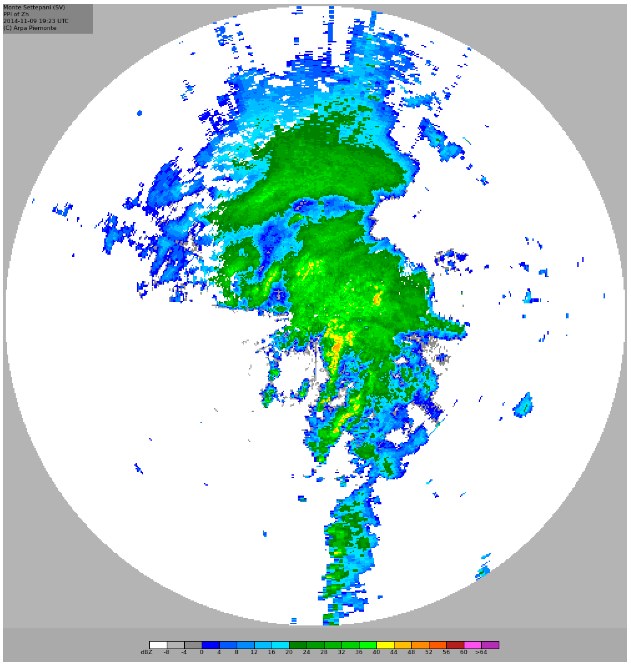

(b) Result of the implemented method with image processing on the same PPI.

Figure 6.9: Comparisons between the Monte Settepani raw (a) and processed (b) reflectivity products during rainfall.

Chapter 7

RFI mitigation and removal

To understand the nature and features of interfering signals in order to implement a new removal tool based on interfering signal features, IQ data have been recorded and analyzed for both C-band and X-band radars. As previously discussed (see Chapter 2), C-band radar are operational and integrated in the National Radar Network, while the X-band is also used for research purposes. In addition, the IQ recording process requires a high computational effort for the radar signal processor. Therefore, few data have been recorded form the operational C-band radar, while several dedicated measurement campaign have been performed using the mobile X-band radar managed by Arpa Piemonte.

7.1 Radar signal theory

Transmitted and received radar signals are described as narrow band signals, since the amplitude and phase modulation of the signal vary slowly compared to the signal baseband. From [2],these signals may be described as:

$$x(t) = a(t)\mathrm{cos}[2\pi f_0 t + \alpha(t)] \tag{7.1}$$

$$= a(t)\mathrm{cos}\alpha(t)\mathrm{cos}2\pi f_0 t - a(t)\mathrm{sin}\alpha(t) sin 2\pi f_0 t \tag{7.2}$$

$$= I(t)\mathrm{cos}2\pi f_0 t - Q(t)\mathrm{sin}2\pi f_0 t \tag{7.3}$$

where I(t) and Q(t) are the in-phase and quadrature phase components of the modulation, respectively. Based on the real signal $x(t)$, the corresponding complex signal $s(t)$ is:

$$s(t) = [I(t) + jQ(t)]e^{j2\pi f_0 t} = a(t)e^{j\alpha(t)}e^{j2\pi f_0 t} \tag{7.4}$$

Therefore the real signal $x(t)$ is the real part of the complex signal:

$$x(t) = Re(s(t)) \tag{7.5}$$

Suppressing the carrier frequency term, the complex envelope is defined as:

$$V(t) = I(T) + jQ(t) = a(t)e^{j\alpha(t)} \tag{7.6}$$

Considering the received signal, it can be written as:

$$s_r(t) = V_r(t)e^{j2\pi f_0 t} \tag{7.7}$$

where $V(t)$ is referred as received voltage.

As reported by [2], the received signal can be written as the sum of single scattererd signal in a given volume. The properties of $I(t)$ and $Q(t)$ may be derived applying the central limit theorem[1] [17]. Thus, for precipitation echoes, the real and imaginary components of the received signal have to satisfy:

$$cov[I(t), Q(t)] = 0 \tag{7.8}$$

where cov is the covariance, which means that the in-phase and quadrature phase components are uncorrelated and their means are zero:

$$E[I(t)] = E[Q(t)] = 0 \tag{7.9}$$

In addition, the variance of in-phase and quadrature phase components is the same.

$$E[I^2(t)] = E[Q^2(t)] = \sigma^2 \tag{7.10}$$

---

[1] The central limit theorem describes the asymptotic distribution of sums of large numbers of independent random variables. In many cases, their properly normalized sum tends toward a normal distribution even if the original variables themselves are not normally distributed.

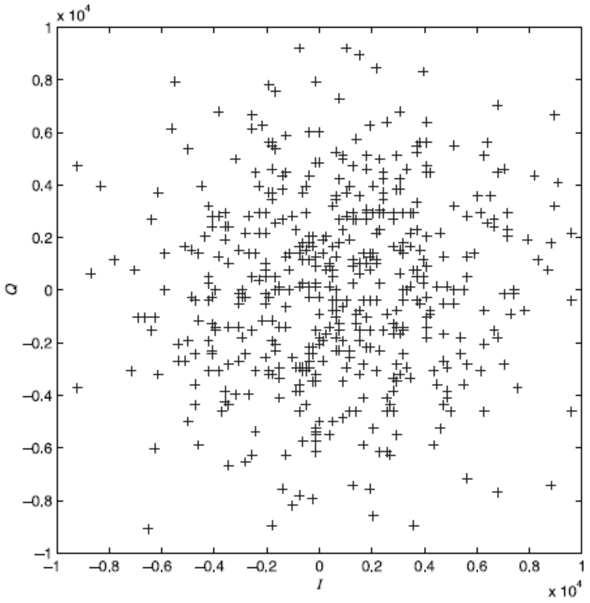

Figure 7.1: Scatterplot of in-phase versus quadrature phase components. Note the uncorrelated nature as given by 7.8. From [2].

The analysis of precipitation signals collected by CSU-CHILL Doppler radar has been shown by [2]. In Figure 7.1, the scatterplot of in-phase versus quadrature phase components is reported, showing that I and Q are spread equally in all directions with respect to the origin (without any preferential direction) indicating that they are independent as given by 7.8.

Radar signal processor usually implements filters to mitigate the interference effects in radar products. One of these is the Signal Quality Index (SQI) thresholding. The SQI is defined as the ratio of the magnitude of correlation at lag 1 (R_1) to the magnitude of correlation at lag 0 (R_0):

$$SQI = \frac{|R_1|}{R_0} \tag{7.11}$$

This ratio is a measure for the coherence of the radar echo. Low coherence data may result from noisy signal levels or from signals with very wide velocity spreads. Where the signal SQI is lower than the threshold the velocity and spectral-width estimates are marked as invalid. The negative side of SQI filtering is the loss of weak weather echoes, such as drizzle or icing phenomena.

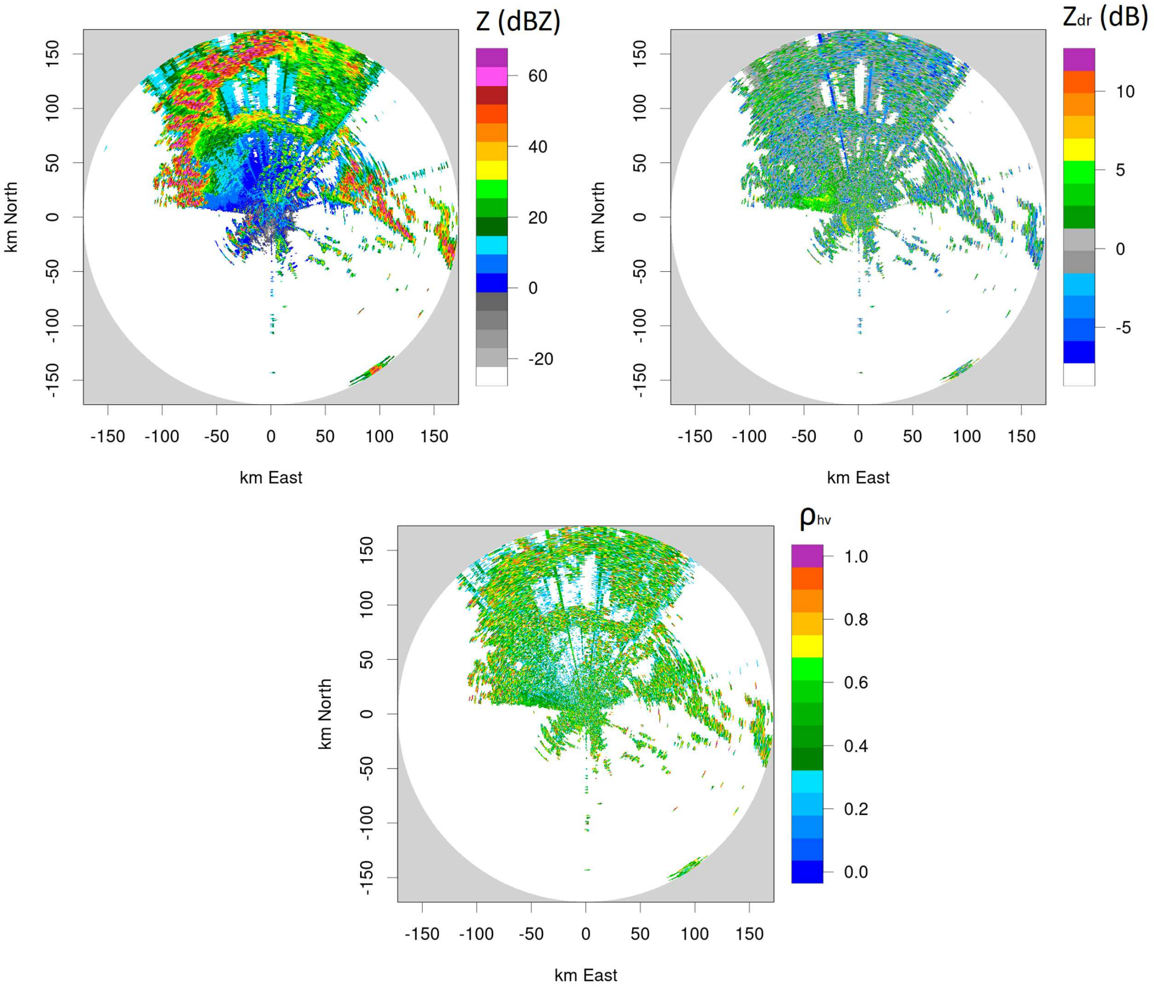

Figure 7.2: From top left: PPIs of uncorrected reflectivity, differential reflectivity and co-polar correlation coefficient corresponding to the acquired IQ data by the C-band radar of Monte Settepani. These PPIs are generated from the acquired signals without any clutter or SQI filtering.

These considerations will be useful to detect the interfering signals and to implement the RFI mitigation tool.

7.2 C-band IQ data

During clear sky conditions, the unprocessed raw data have been recorded by Monte Settepani radar at the lowest elevations scan. At -0.3° the radar beam intercepts the orography in the North and Est sector, mountain and hills, and some sea echoes are likely in the South domain of the radar.

In Figure 7.2 top left, the processed radar product of uncorrected reflectivity is shown, where no clutter filtering is applied. In this radar product it is not straightforward to identify the electromagnetic interference due to the overlap with clutter. In fact, we can note that the North East and North West sectors may appear as clutter areas. Considering the uncorrected differential reflectivity and co-polar correlation coefficient in Figure 7.2 top right and bottom, we can better discriminate RFIs and clutter, especially in the North East sector, pointing out the amount of interference received by the C-band radar. The raw data of the shown radar scan have been recorded and analyzed. For a single scan, 360° and 300 range bins, the IQ dataset is composed by 2800 range gate and 6491 azimuth data, equivalent to 300MB of disk memory. Consequently, a single azimuth ray in radar product is computed over 18 rays in IQ data. Pulsed and continuous interfering signals are recorded and reported in Figures 7.3, 7.4 and 7.5, where the horizontal polarization in-phase component of the received signal is displayed. The colorscale represents the magnitude of the in-phase component. The high values vertical areas represent the clutter since it is received for several azimuths, while the interfering signal is received as approximately $500\mu s$ pulses repeated every millisecond. Even the interfering signal is pulsed as in Figure 7.4, in the radar product a specific ray may appear as a continuous interference, due to the IQ processing. In a different sector of the radar domain, see Figure 7.5, the interfering signals appear as continuous over range and also, in some cases, over azimuth. Due to nature of the interfering sources, it is likely that in this angular sector the radar receives several signals generated by different sources, which are overlapped over the time axis. The investigation of the RFI features is performed on the pulsed signal, then is extend on the areas of continuous interfering signals.

The dataset of interfering signals received in a single scan at the lowest elevation exceeds 1000, which means the one ray over six is affected by RFI in the IQ data. Several pulsed signals have been analyzed to investigate the specific features. Since they show similar proprieties, in the following images the analysis of a single signal is reported. In Figure 7.6, the in-phase components of the selected signals are displayed for both horizontal (red dots and line) and vertical polarization (unfilled black circles and black line). The histogram of $I^2 + Q^2$ is computed, see Figure 7.7, and it

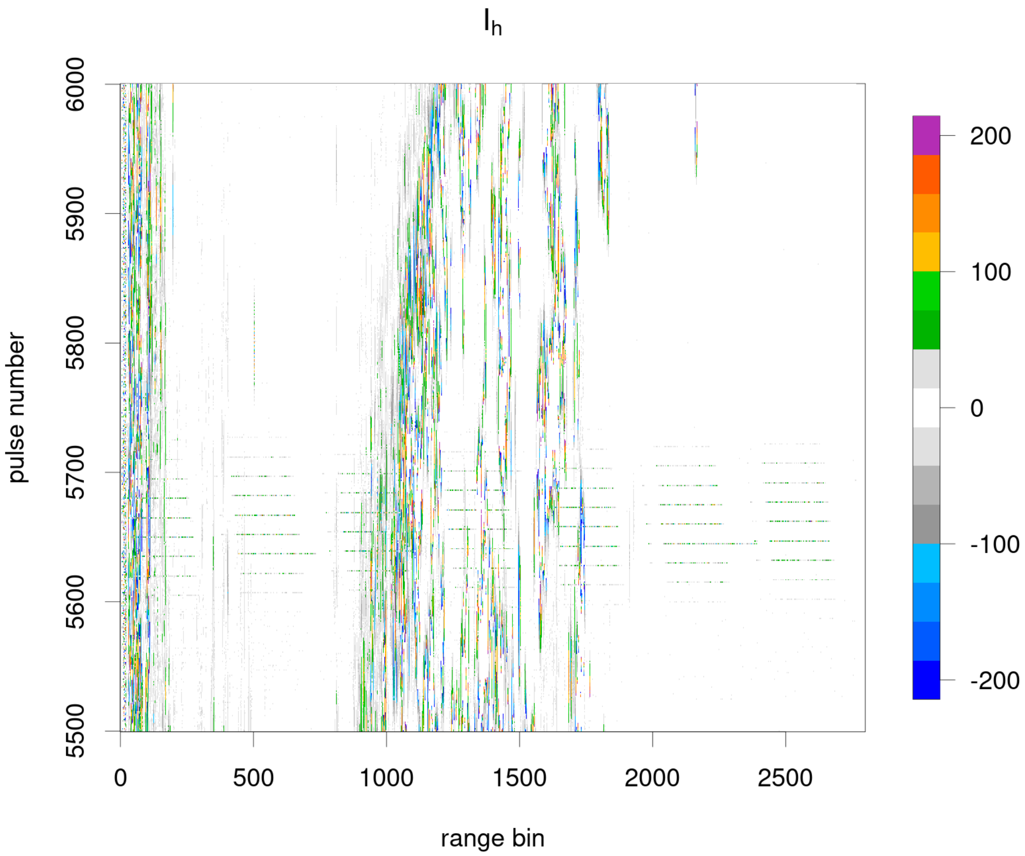

Figure 7.3: In-phase horizontal polarization of the received echoes.

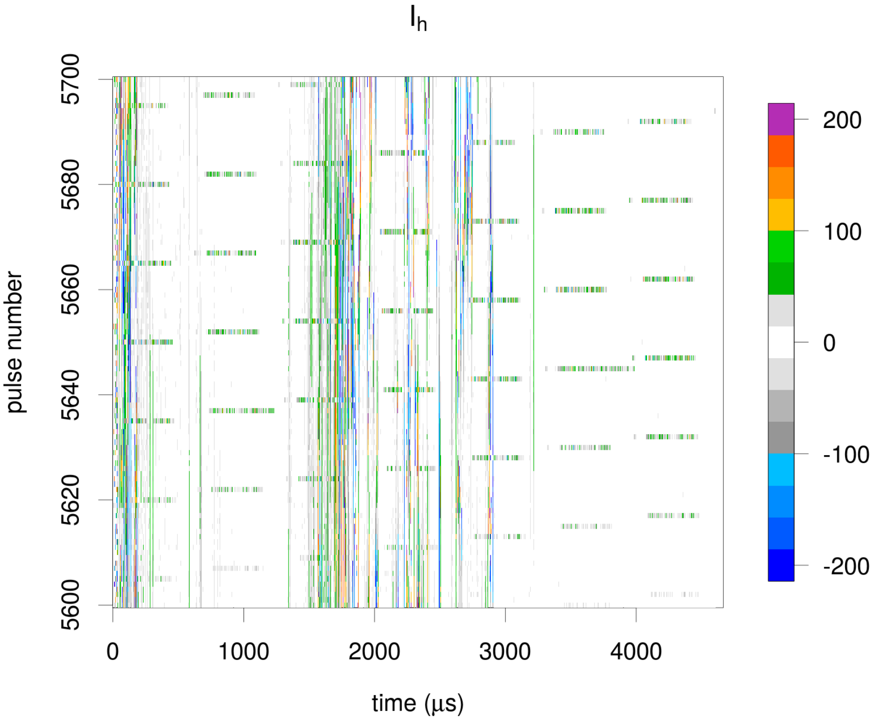

Figure 7.4: Detail of Figure 7.3.

is compared to the IQ behaviour in precipitation. From [2], the log histogram of I^2+Q^2 in weather echoes decreases linearly, indicating the I^2+Q^2 is exponentially distributed. The interfering signal, instead, shows a slowing decreasing histogram of I^2+Q^2, indicating that the probability of detect high I^2+Q^2 samples is almost constant in a wide range of values. This feature may be useful to discriminate weather echoes and RFIs.

Spectral estimate are performed on the selected signal. In particular the Doppler velocity spectrum of the received signal is computed and it is shown in Figure 7.8. Since the estimate is performed only on the signal reported in Figure 7.6, the Doppler spectrum is not contaminated by clutter, i.e. ground clutter or any other forms of clutter which is not electromagnetic interference. The computed power spectrum density varies of about ±3dB in the range -20m/s to +20m/s. It is also remarkable that the 0m/s component, related to static echoes, has a lower power spectral density compared to the range -20 to -10m/s and 10 to 20m/s. We can also understand that the

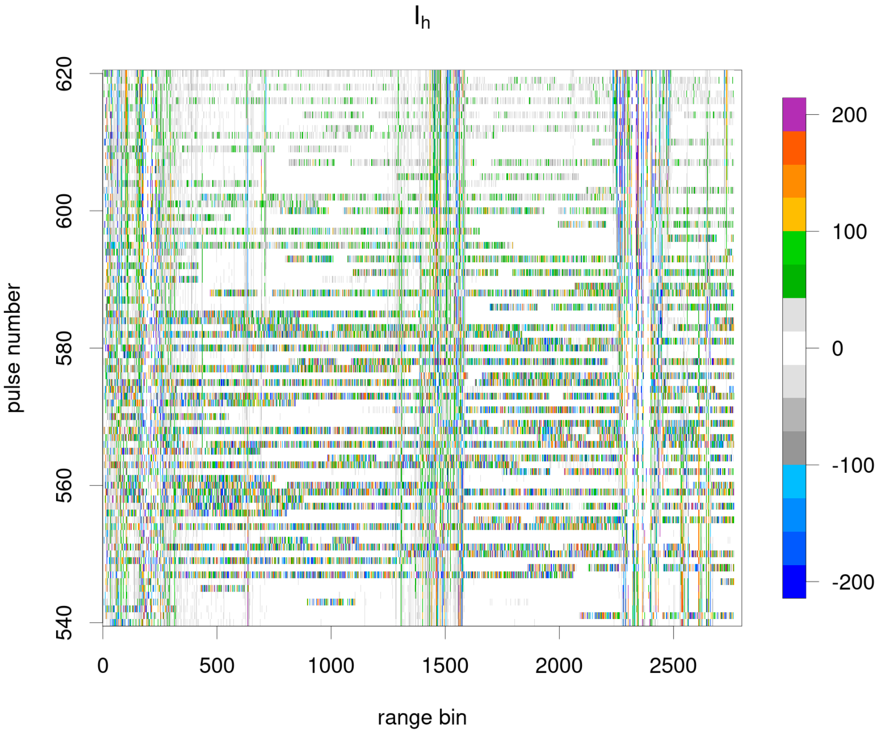

Figure 7.5: As Figure 7.3, but in a different angular sector.

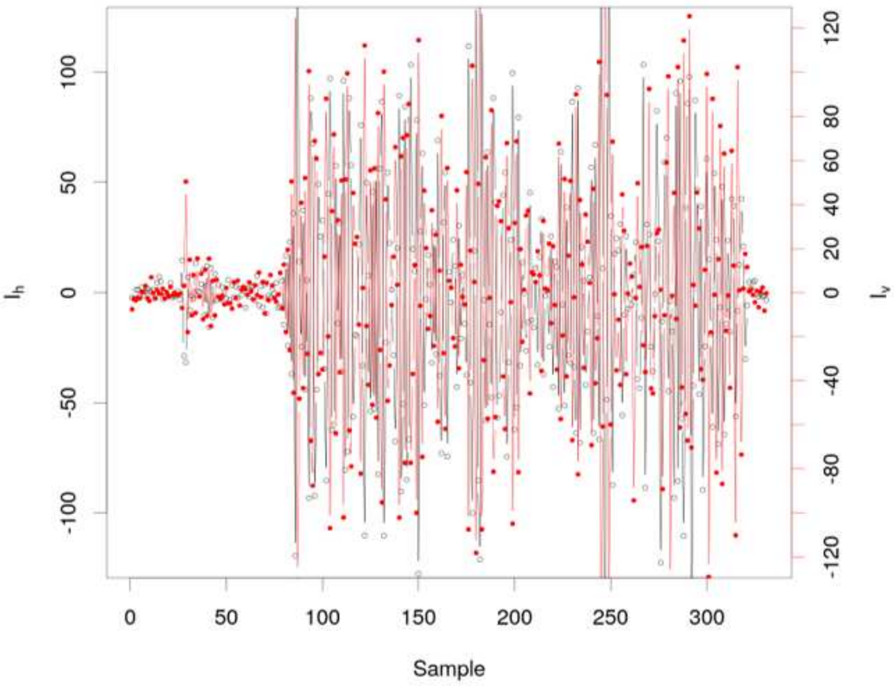

Figure 7.6: Horizontal and vertical polarization in-phase component of the received interfering signal. The horizontal polarization is represented by the red dots and line, while the vertical polarization by the unfilled black circles and black line.

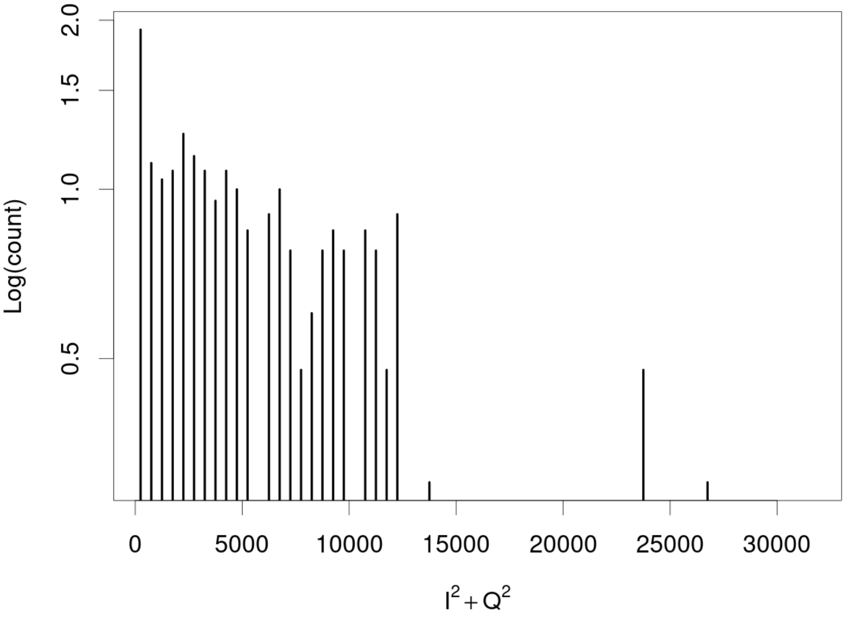

Figure 7.7: Histogram of $I^2 + Q^2$

energy in the interfering signal is spread over a frequency range, such behaviour is standard for WLAN systems.

The investigation on the specific features in IQ data is reported in Figure 7.9. The aim is to identify patterns that allows to identify the interfering signals. Since the radar receives simultaneously both horizontal and vertical polarization, the polarization state of the interfering signal is investigated. The scatterplots of I_h versus I_v and Q_h versus Q_v show that the interfering signal is slant polarized. The slant polarization is commonly used in telecommunication system due to the increased application of polarization diversity systems [18]. Concerning the signal modulation, the scatterplot of I_h versus Q_h and I_v versus Q_v are displayed. In this case, from the acquired IQ data it is not possible to recognize any specific pattern since it is likely that the detected signals are not received directly from the RFI source but they are received after scattering in the environment.

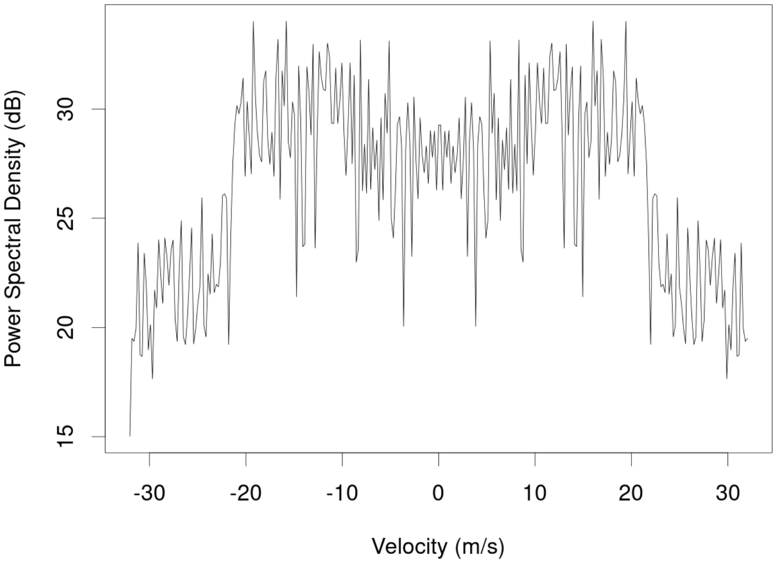

Figure 7.8: Periodogram estimate of the Doppler velocity spectrum of the received interfering signal.

7.3 X-band IQ data

The X-band mobile radar has been dedicated to several measurement campaign to investigate the nature and features of interfering signals at 9.37GHz. Especially the raw data acquisition of interfering signal has been performed. One of the interfering signal investigated is the one detected in the North West sector of the radar domain. The PPI of the angular sector is reported in Figure 7.10 and Figure 7.11, where is clearly visible the interfering signal which appears as pulsed RFI. The IQ data corresponding to the shown sector have been recorder and post-processed. The in-phase component of the horizontal polarization channel is shown in Figure 7.12, where the colorscale represents the magnitude of the received I_h. We can note that the interfering signal is received in several pulses that compose the azimuth in the radar PPI in Figure 7.10.

As for C-band interfering signal, the spectral analysis is performed on several pulses and the results are reported considering a representative pulse. The histogram of $I^2 + Q^2$ is reported in Figure 7.13, using a logarithmic y axis scale. Differently from C-band RFI, the histogram shows two clearly separated areas. Clear sky echoes are displayed for low $I^2 + Q^2$, say less than 150,

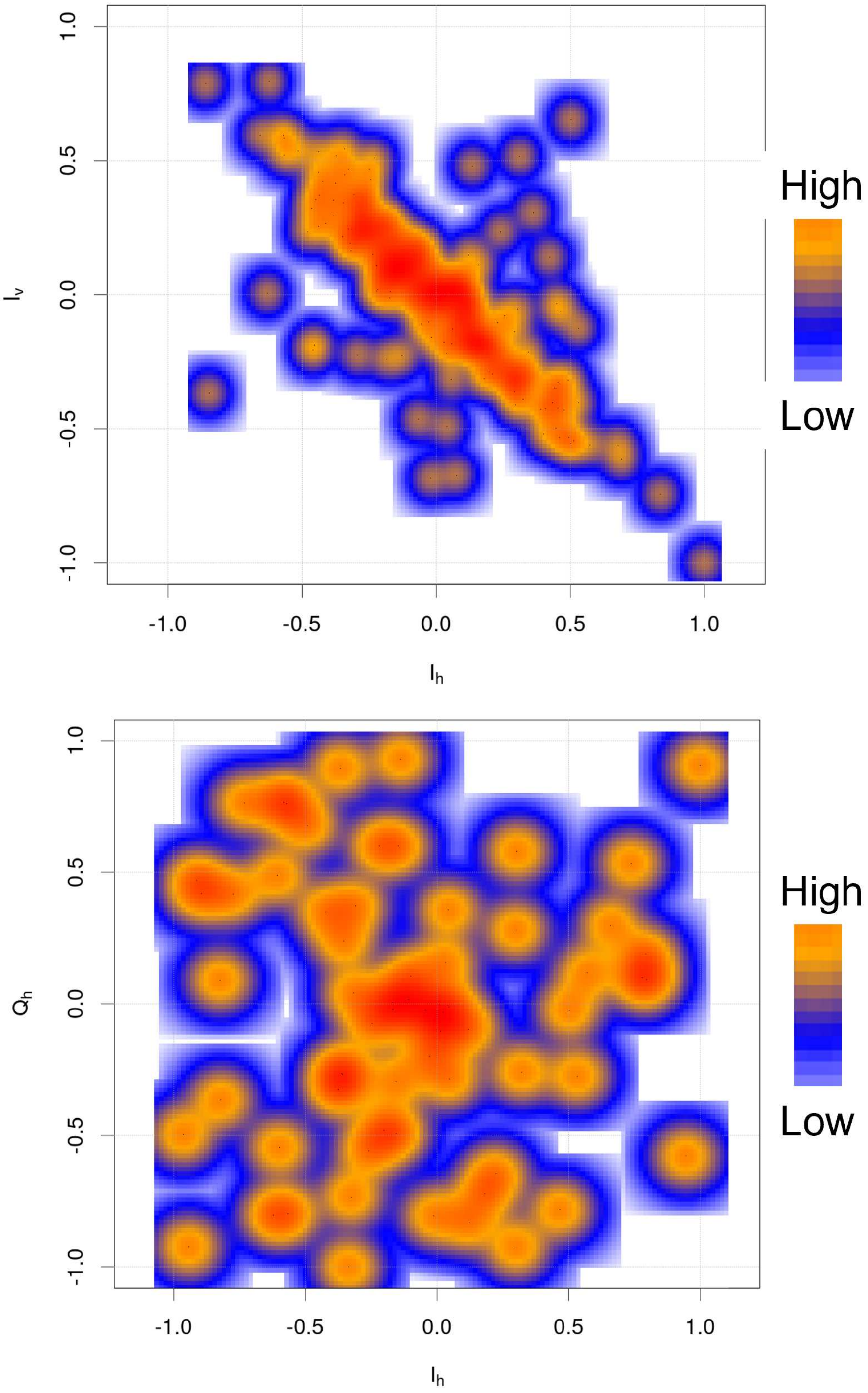

Figure 7.9: IQ analysis of the interfering signal. First row: in-phase components of the horizontal versus vertical polarization is shown. Second row: I versus Q for horziontal polarization is displayed.

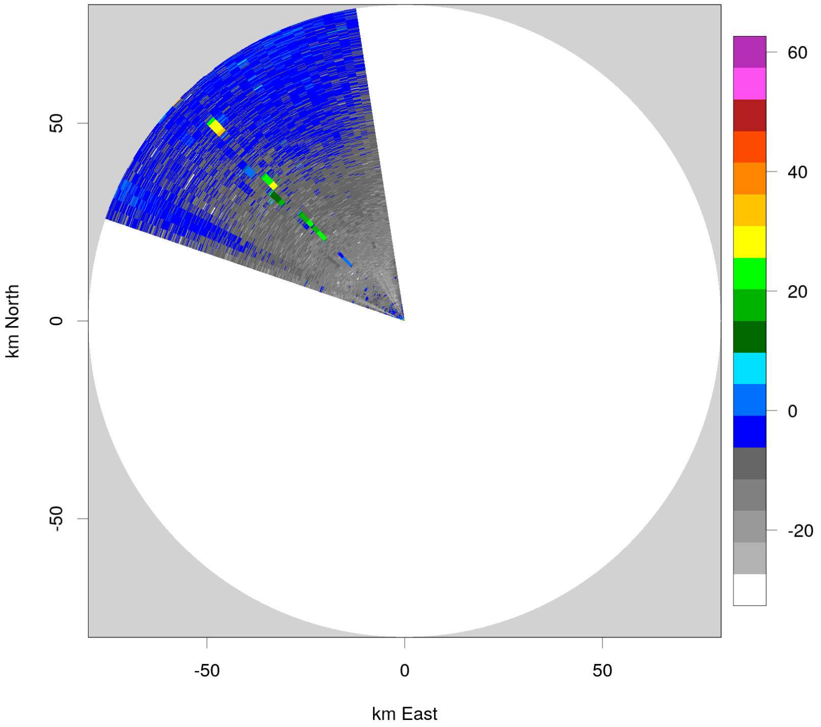

Figure 7.10: PPI of radar reflectivity corresponding to the acquired IQ data

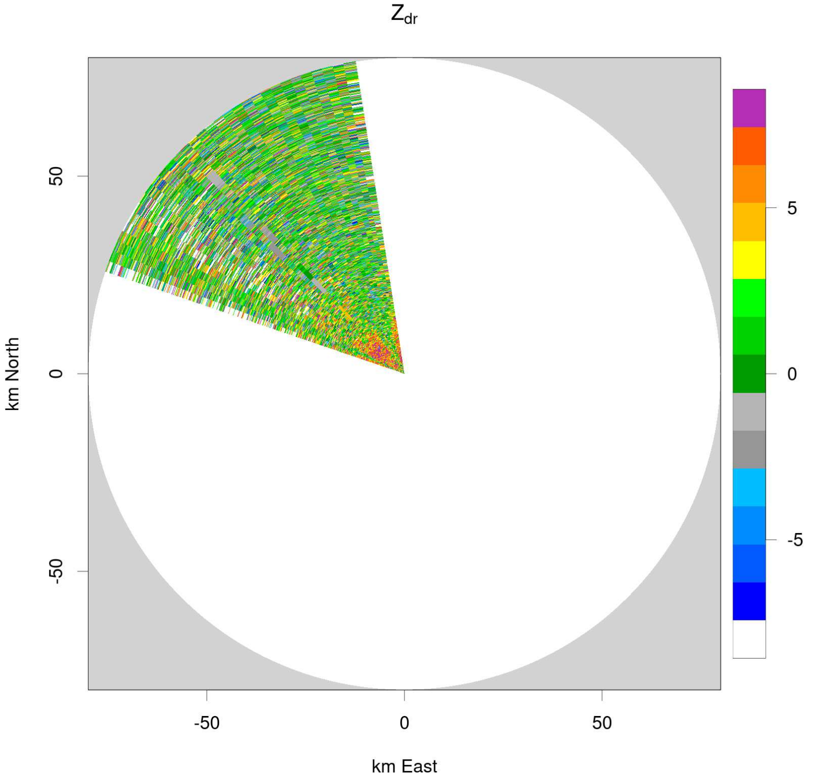

Figure 7.11: As Figure 7.10 but for differential reflectivity

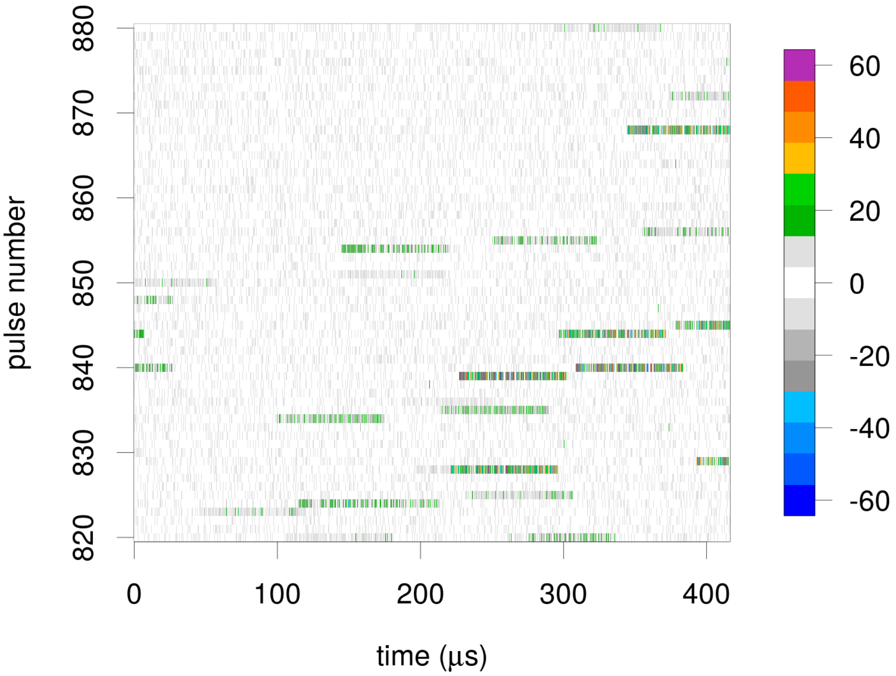

Figure 7.12: IQ data, interfering signals are show.

where the histogram decreases linearly. The interfering signal $I^2 + Q^2$, instead, are shown in the range 500-1000, with a flat pattern. The power spectral density is estimated on the IQ data of a single pulse and it is reported in Figure 7.14. The Doppler spectrum is computed on data unaffected by static clutter, such as orography, however it is remarkable the 0m/s power spectral density. Based on the measurements performed using the Keysight FieldFox vector signal analyzer (see Chapter 5), we know that the X-band radar receives a signal at 9.37GHz with sharp peak value. As consequence, the power spectral density shows a 0m/s peak and a smooth decrease between 1 and 5m/s, with symmetry through the 0m/s. Compared to the RFI at C-band, the X-band interfering signals have a reduced spectral amplitude and, consequently, the signal energy is spread over a limited range of velocities in the Doppler spectrum.

The in-phase and quadrature phase of the interfering signals have been investigated and interesting patterns have been found. The polarization state of the received signal is reported in Figure 7.15, where horizontal and vertical received channels are displayed for both I (blue dot) and Q (red square). The values of I and Q have been normalized. The signal is elliptically polarized along the -45° bisector for both in-phase and quadrature phase components. This specific patter allows to

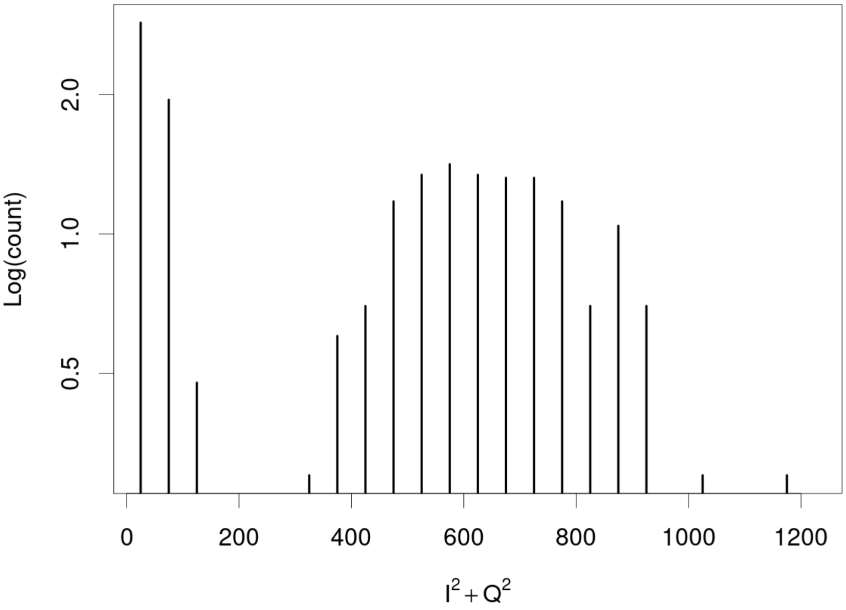

Figure 7.13: Histogram of $I^2 + Q^2$

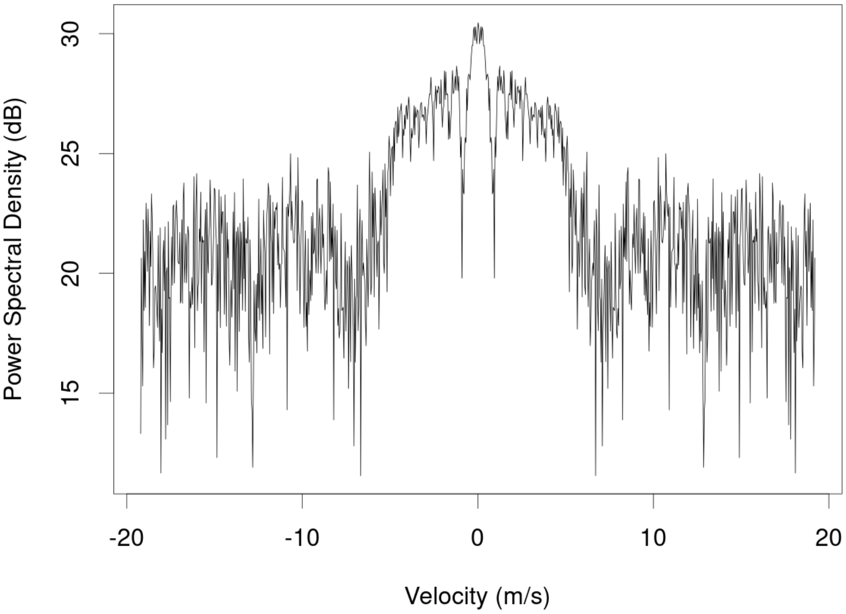

Figure 7.14: Periodogram estimate of the Doppler velocity spectrum of the received interfering signal.

identify the interfering signal in IQ data. The scatterplot of in-phase and quadrature phase components shows a circular pattern for both horizontal and vertical polarization. This is clearly visible in Figure 7.16, where the horizontal polarization is displayed as blue dot and the vertical as red square. The normalized values are located along the unit circle in the I-Q plane, so they satisfy:

$$In^2 + Qn^2 = 1 \tag{7.12}$$

where In and Qn represent the normalized values of I and Q respect to their maximums. The auto-correlation of IQ signal is non zero only at lag zero. So we can suppose that this particular modulation can be a Zadoff-Chu sequence, which is commonly used in LTE modulated signals. In the LTE specifications, Zadoff–Chu sequences have been widely selected as the reference signal in many applications, such as the primary synchronization signal (PSS), the uplink reference signal, and the reference signal in the random access channel and also in the physical uplink control channel (PUCC) [19].

7.4 RFI removal implementation and results

The proposed algorithm is based on the interfering signal features described in the previous section. The flow chart of the tool is reported in Figure 7.17. At radar signal processor level, the algorithm should be implemented after the raw data acquisition for a single elevation scan. For each IQ pulse the tool computes analysis on the acquired data to identify likely interfering signals. The analysis is performed by cluster areas over the range axes, corresponding to the radial distance. The cluster length is defined as one third of the duration of the detected signals. Specifically, for the X-band radar the interfering pulse last for approximately $70\mu s$ and the cluster length is set to $20\mu s$. If a cluster meets the RFI features described in the previous section for polarization and modulation within a 10% tolerance, then the corresponding IQ data for both polarization channels are set as invalid and removed in the following elaborations. The aim of the proposed algorithm is to restore the echoes that are overlapped with interfering signals. So, where the IQ data are recognized

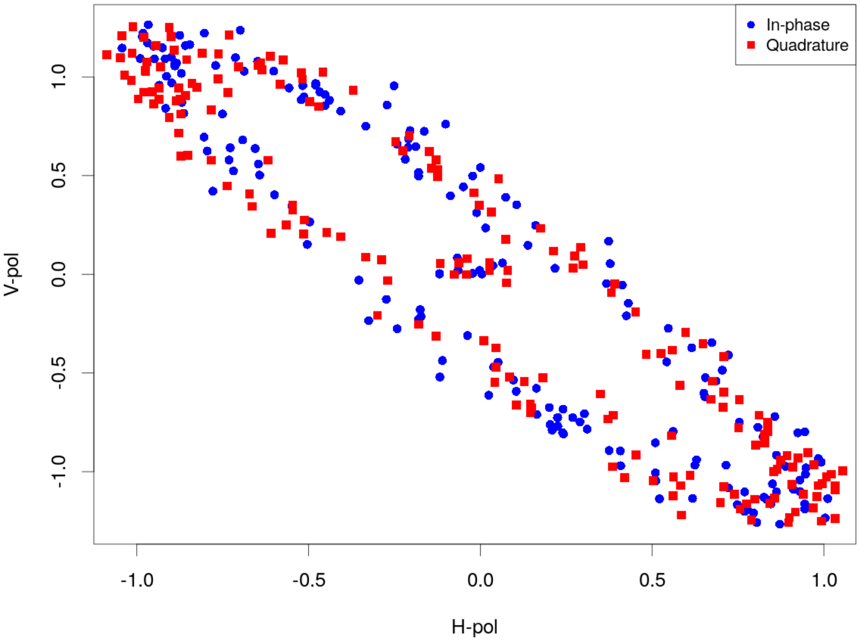

Figure 7.15: The in-phase (blue dot) and quadrature phase (red square) are displayed as horizontal versus vertical polarization. The values have been normalized.

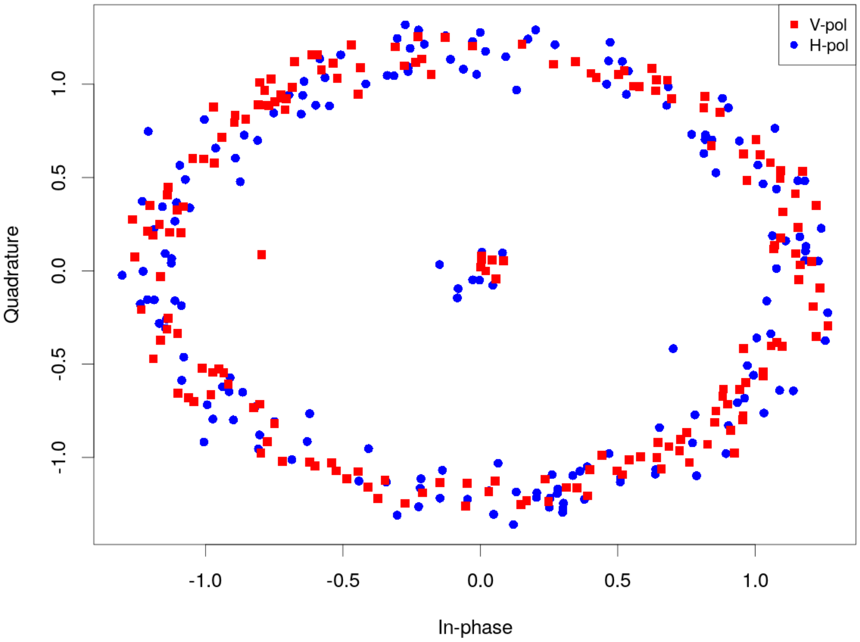

Figure 7.16: Scatterplot of I and Q for both horizontal (blue dot) and vertical polarization (red square).

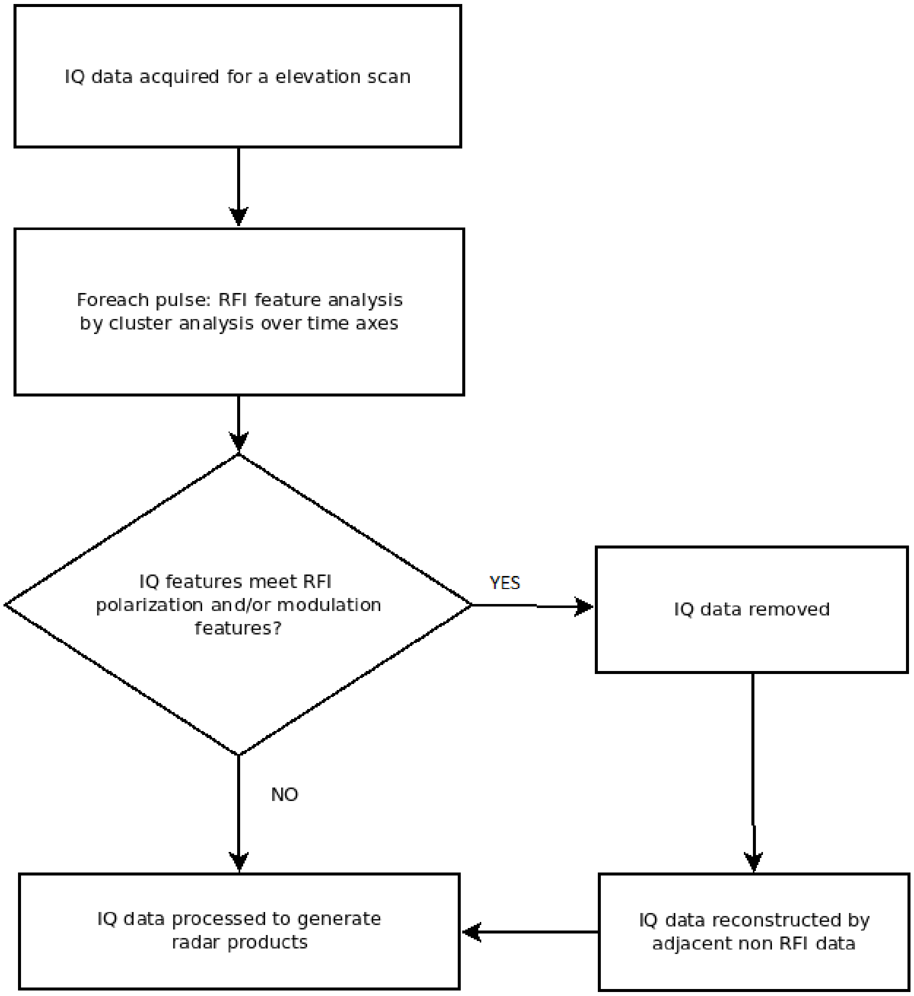

Figure 7.17: Flow chart of the proposed RFI removal tool.

as interference the algorithm reconstructs the likely radar echo by averaging the previous non-interference data. Finally, the IQ data matrix can be processed to generate radar products.

The study case of the proposed algorithm has been implemented in a data analysis programming language, which is R-cran. For operational radar, the code will be translate in the appropriate language to be executed in the radar signal processor. For this research work, the tool runs on a Intel i7 processor laptop with 8GB of RAM memory. The program could only run on a single core of the processor, so the computing time could be easily decreased parallelizing the execution over several cores. The RFI removal and mitigation tool is performed on the X-band data previously show. The execution time is approximately four seconds and the results are displayed in Figure 7.18, where the acquired data (left side) are compared to the processed data (right side). We can note that, in the processed data, the interfering signals have been removed and the data reconstructed. The reconstruction processes, however, needs to be improved, since there is no continuity over azimuth. A refined version of the tool should take into account also the azimuth data in order to recover the data affected by radio frequency interference. For the X-band radar, the polarization of the received interfering signal is elliptical so, I_h and I_v follow the equation:

$$aI_h^2 + bI_hI_v + cI_v^2 = 0 \tag{7.13}$$

where a, b and c are parameters retrieved by fit of the I_h and I_v acquired data. For this specific radar, $a = -0.62$, $b = 0.54$ and $c = -0.56$. Considering about 20 interfering signal, the parameters vary less than 20%. The normalized I_h Q_h data, instead, are located on the unit circle so their quadratic sum should be one. To evaluate the presence of a modulation in the received signals, the Error Vector Magnitude over a set of likely modulation is computed. Currently the algorithm seeks PSK modulation with a 10% tolerance respect the unit circle.

Overall, the performance of the proposed algorithm appears satisfactory. The interfering signal are properly recognized and removed and the processing time is suitable for real-time processing.

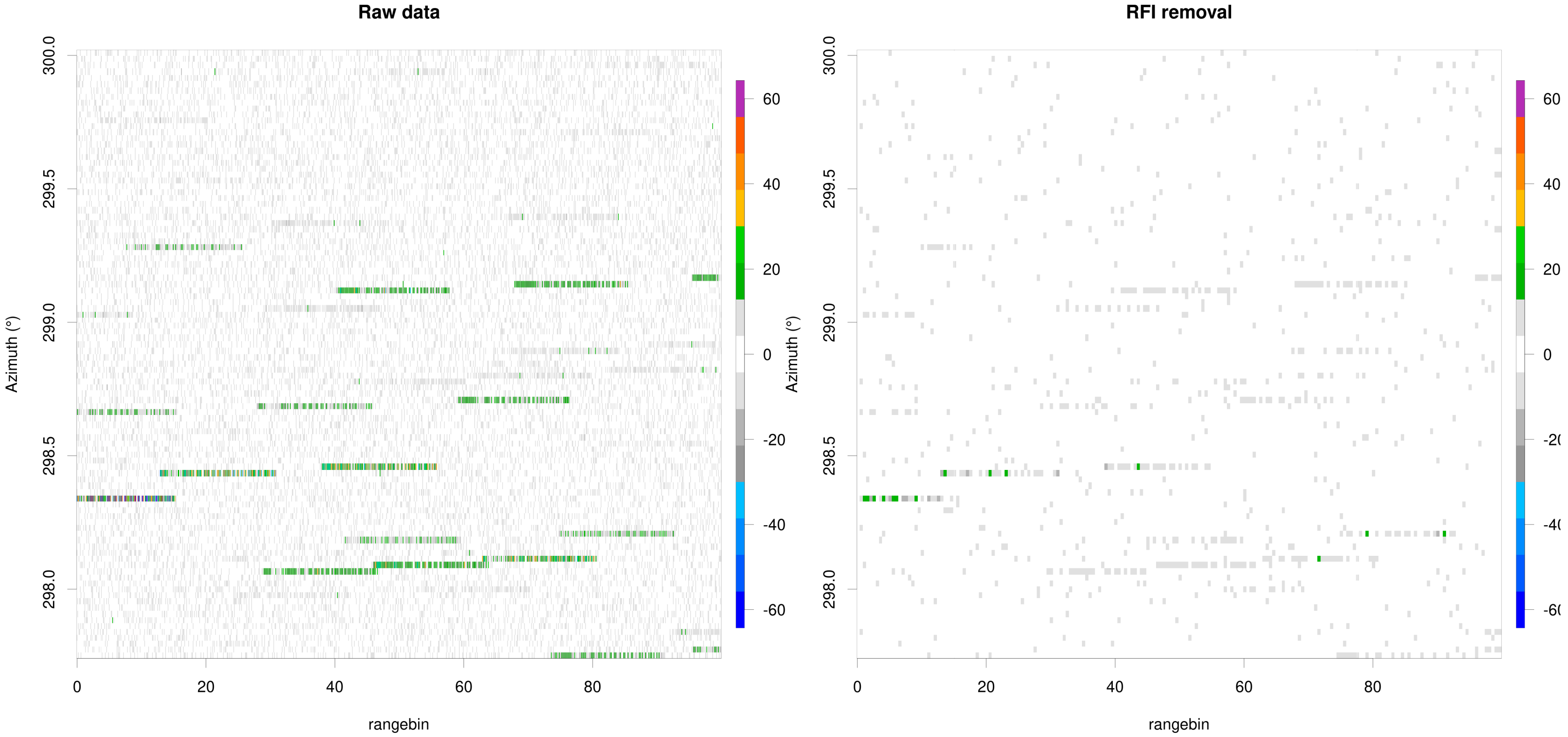

Figure 7.18: I_h data acquired by the X-band radar (left side) and processed data. The interfering signals are visible in the raw data as horizontal lines, while in the processed data they are removed and the missing data are reconstructed.

The RFI removal tool has been also performed on the C-band IQ data, previously shown. Also in this frequency band, the algorithm identifies properly the interfering signals. Only portions of the pulsed RFI are not identified and this will be further investigated in the next months. The reconstruction of the radar echoes will be upgraded since, when RFI are overlapped with clutter, the current version of the code does not act properly. Furthermore, as previous discussed, the smoothing over adjacent pulses will be implemented.

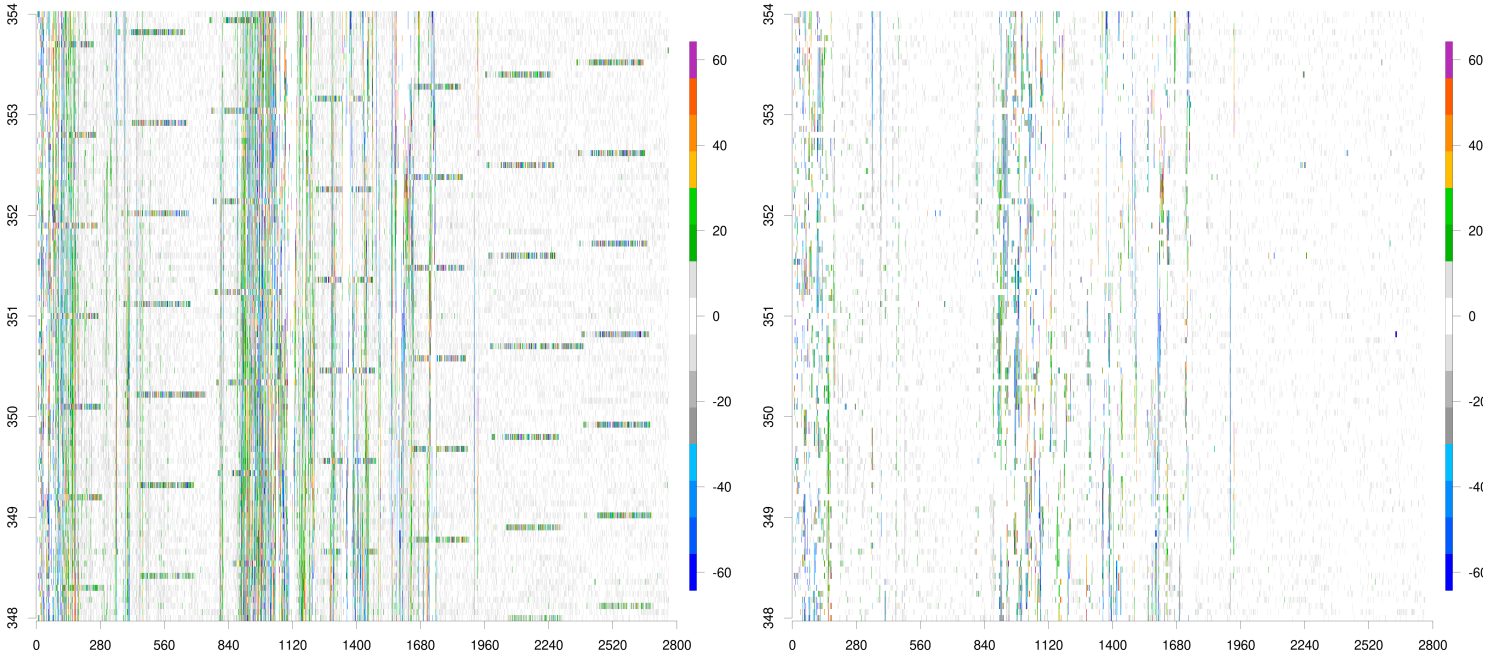

Figure 7.19: I_h data acquired by the C-band radar (left side) and processed data. The interfering signals are visible in the raw data as horizontal lines, while in the processed data they are removed and the missing data are reconstructed

.

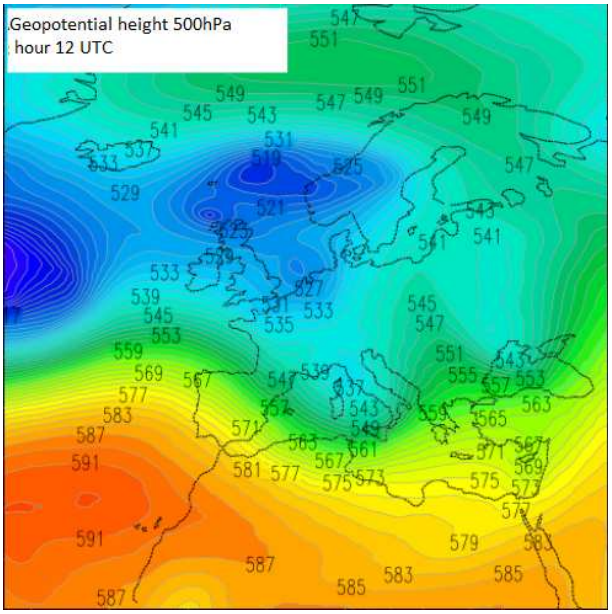

Figure 7.20: 500hPa geopotential height over Europe, 22 November 2022 at 12 UTC.

7.5 RFI removal and meteorological echoes

The RFI removal tool described in the previous Chapter has been tested during precipitation. Interference may affect weak weather echoes, such as drizzle, light rain or ice-phase phenomena. Therefore, this algorithm has been applied on selected study cases, where light rain was observed in the radar domain. Unfortunately, due to a hardware fault at the magnetron, the X-band radar could not acquire data during Fall and Winter 2022. As consequence, the C-band radar was deployed to collect IQ data during precipitation. The precipitation areas over the East side of Piemonte region during the 22 November 2022 have been selected to test the algorithm. The precipitation were generated by a trough from England, which caused a pressure minimum at the ground over the Ligurian Gulf, as reported in the 500hPa geopotential height inf Figure 7.20. During the morning of 22 November, the pressure minimum moved eastward, due to high winds from West, producing light rain over the East side of Piemonte region. The satellite image at 12 UTC showed stratiform clouds over the eastern Piemonte, see Figure 7.21 where the Piemonte region is in the center of the image.

The cumulative rainfall over the 22 November is displayed in Figure 7.22, whose colors represents the cumulative precipitation over 12 hours. During the morning, the precipitation were

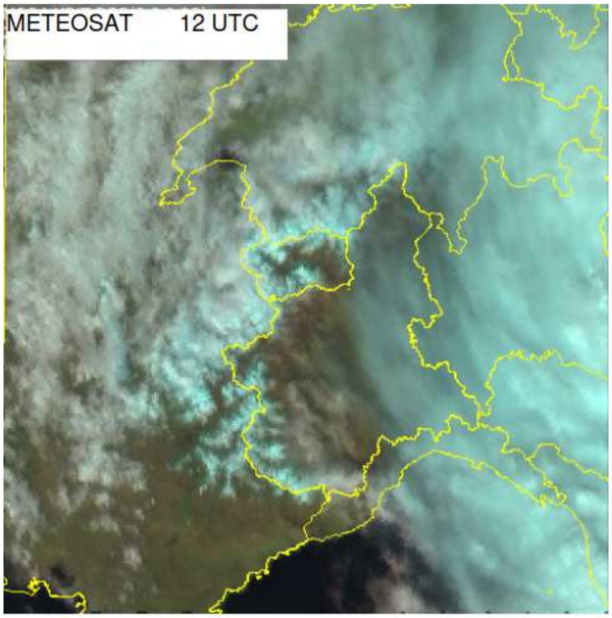

Figure 7.21: MeteoSAT image of Piemonte region (center of the image) 22 November 2022 at 12 UTC.

localized over the east sector of the region, which corresponds to the East side of the C-band radar domain. The maximum rainfall over the morning was 15mm over 12 hours. The freezing level was located at 1800m above the ground, therefore at the lowest elevation scans performed by the Bric della Croce C-band only rain areas are expected.

As reported in Chapter 2, Bric della Croce radar operates a dual PRF strategy to enhance the unambiguous velocity: low PRF is set at 588Hz and high PRF is set at 882Hz. The mitigation tool is applied as post-processing on the IQ data for each PRF. The selected IQ data have been acquired at the lowest elevation scan -0.1° which contains ground clutter contamination. In Figure 7.23, the in-phase horizontal component of the received signal is displayed: clutter areas are detected over several range gates for distances less than 75km, while meteorological echoes are received over 100km. Several radio frequency interferences are detected, especially at pulses corresponding to azimuths between 83 and 85°. Pulsed interfering signals are however received in almost every transmitted pulse.

The radar reflectivity is computed from the acquired IQ data and it is compared to the radar reflectivity product generated by the radar signal processor. Figure 7.24 shows the computed radar reflectivity (left) and the radar product (right), where standard RFI filters are applied, such as

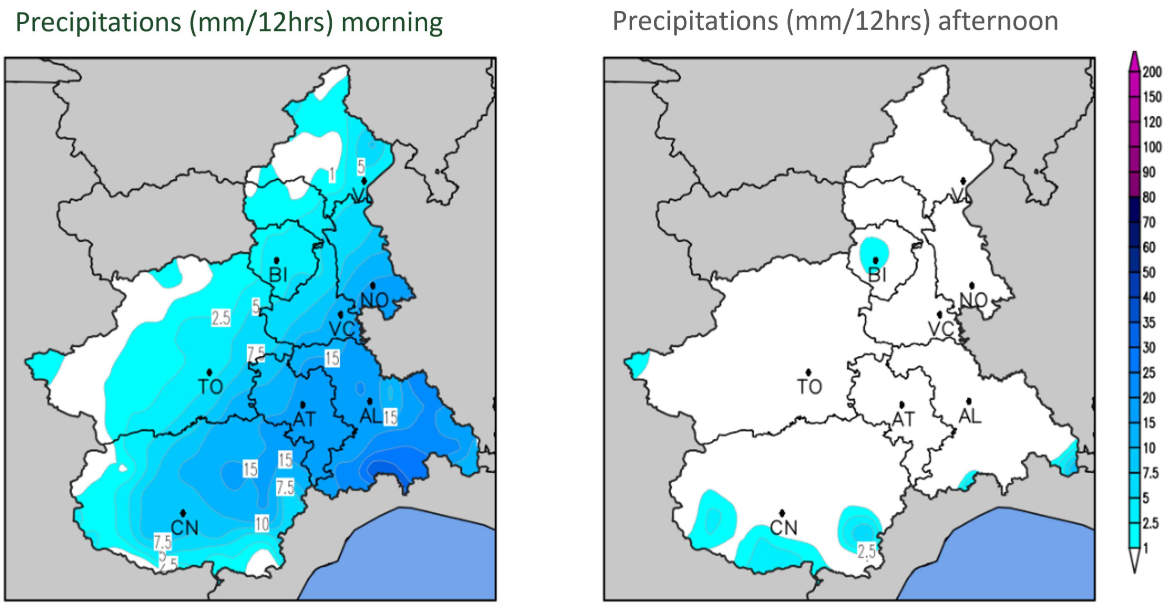

Figure 7.22: Cumulative precipitation over 12 hours (morning and afternoon) of 22 November 2022, the C-band radar is located near the TO point in the images.

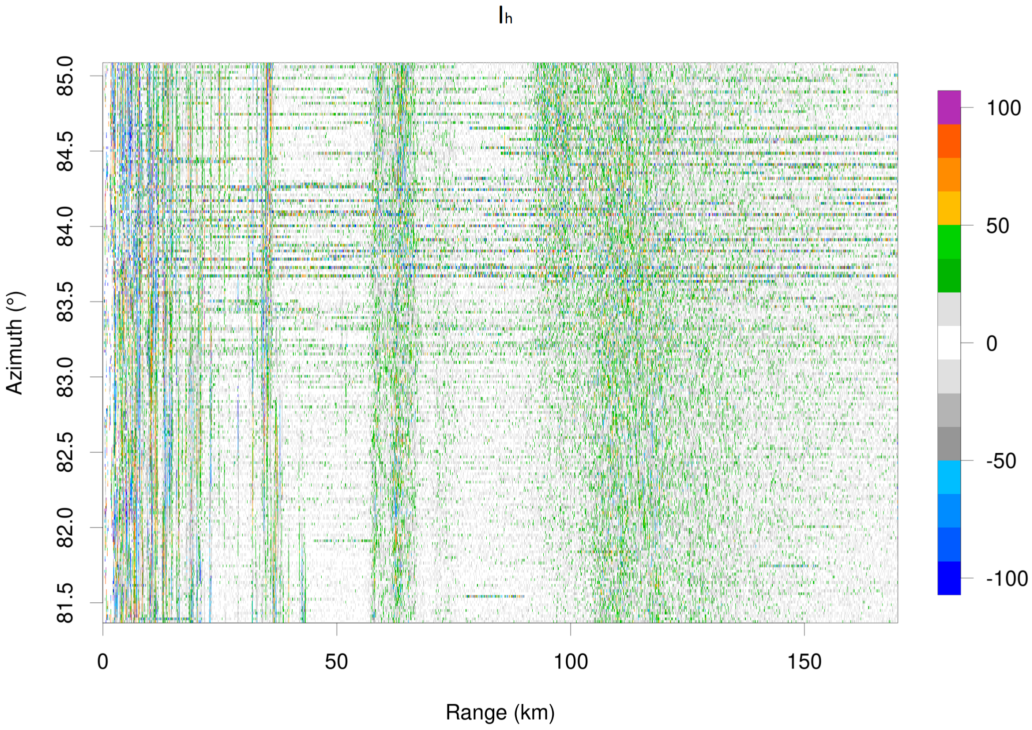

Figure 7.23: I_h data acquired by the C-band radar at 08:50 UTC of 22 November 2022. Interfering signals are clearly visible especially after azimuth 83.5°, while clutter echoes are received below 75km range. The meteorological echoes are collected over 100km.

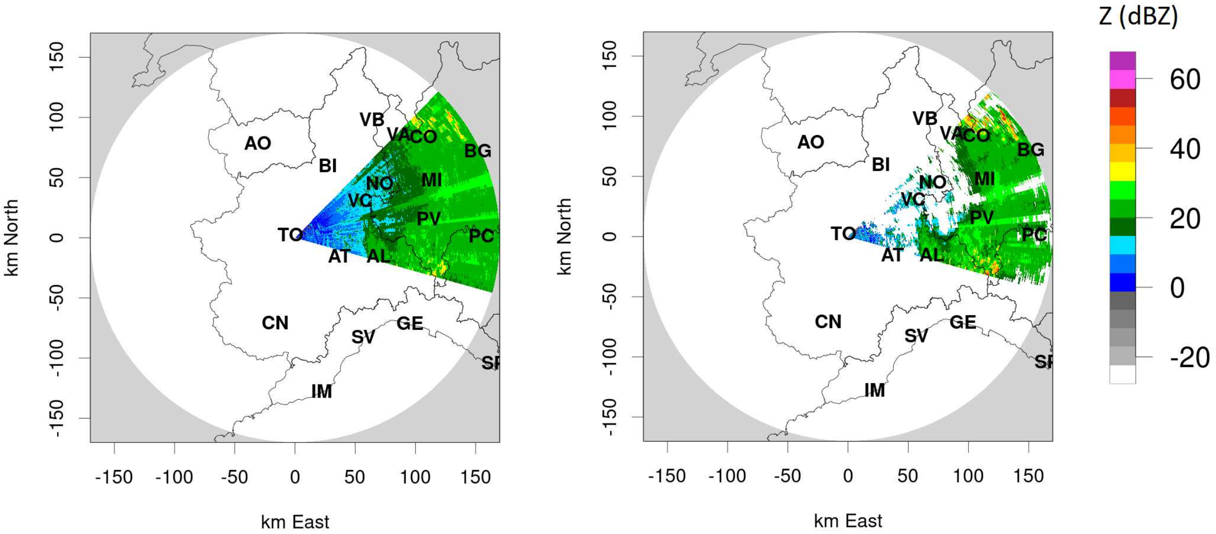

Figure 7.24: PPIs of uncorrected reflectivity in the study-case sector. Left side: Z computed from the acquired IQ data. Right side: operational Z product computed by the radar signal processor.

Signal Quality Index and speckle filters, in the Est sector of the radar domain. Clutter areas are visible at about 50° and 110° associated to high reflectivity values. The Z computed by the signal processor does not show values beyond the clutter areas due to poor correlation of the received echoes, while the Z computed by IQ data, which are unfiltered, shows received echoes. RFI are clearly detected in particular at azimuths 80°, 85°, and 108°. The signals of interest in this study case are the ones overlapped with meteorological echoes. In fact, we can note that standard filters remove the meteorological echoes in the azimuths affected by RFI (Figure 7.24 right).

The mitigation tool previously described is applied to the raw IQ data to remove interfering signals and to reconstruct the removed data. In Figure 7.25, the Z computed from raw IQ and the Z computed after the RFI mitigation tool are displayed. The interfering signals are properly removed and the missing data in the pulses are computed by smoothing from adjacent range gates and pulses. Comparing the raw and processed IQ data, we can note that the reconstruction process can smooth clutter areas since thresholds on the zero Doppler are applied to decrease the amount of processed data.

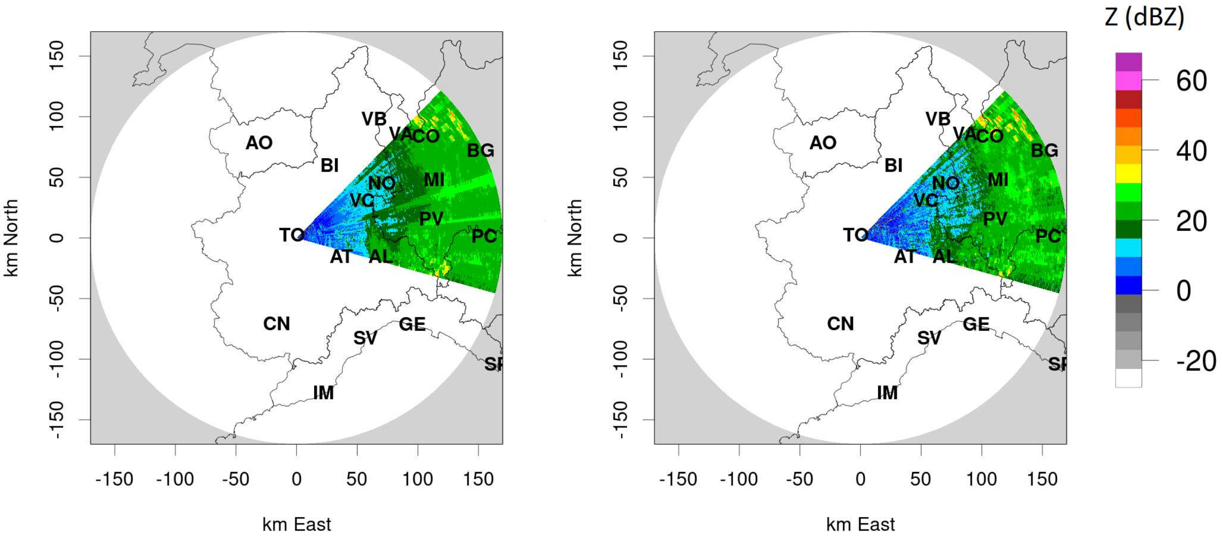

Figure 7.25: PPIs of uncorrected reflectivity in the study-case sector. Left side: Z computed from the acquired IQ data. Right side: RFI removal tool is applied on the IQ data befor computing Z.

The results of mitigation tools in term of computed radar reflectivity are compared to the Z computed by the radar signal processor, as shown in Figure 7.26. Several azimuths are removed by the signal processor due to the presence of RFI which lower the signal quality. Since a single azimuth is computed over about 50 pulses, the removal of some pulses or fractions of a pulse does not affect the computed reflectivity. Actually, removing only the interfering signals the proposed tool is able to preserve the meteorological echoes which lead to a better estimate of the reflectivity values, especially in case of weak echoes (i.e.light rain or drizzle).

Since the radar signal processor applies further filters on the IQ data which have not been implemented to compute Z from the RFI removed IQ data, the performances of the proposed method, in case of light rain, are evaluated on a set of azimuths between 80 to 90°. In this azimuthal region, clutter echoes are not received and the signal quality is only affected by the RFI and meteorological echoes. The proposed mitigation solution does not remove range bins due to the presence of interfering signals since every range bin of a given azimuth is computed over several radar pulses. As consequence, for azimuth 85°, the amount of reflectivity values displayed in the histogram is higher than the ones computed by the radar signal processor. The effect of the interfering signal

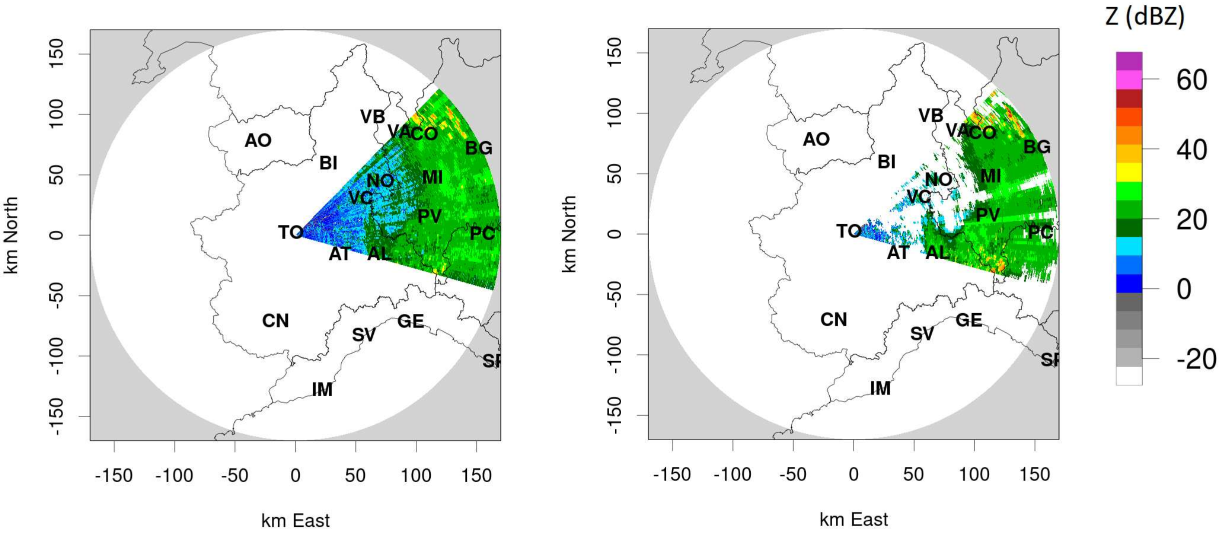

Figure 7.26: As in Fig 7.24, but the RFI removal tool has been applied on the IQ data.

removal and weather echoes reconstruction is clearly visible considering the Z values over the radar distance, as reported in Figure 7.27 for azimuth 85° where the black squares represent the Z computed by the current mitigation tool in the radar signal processor and the red dots the Z computed from the IQ data processed by the proposed mitigation tool. Where no data are available in the Z computed by the signal processor, the proposed mitigation tool is able to keep data for the weather echoes reconstruction as we can note at range 50km and 100km. In the range between 100 and 120km the two methods lead to Z values with a 0.2dB average difference, while for greater distances there are a couple of dB of difference due to the effect of the partial RFI removal in the signal processor. In fact, considering Figure 7.26, we can note that over azimuth 85°, such as azimuth 75°, there is a remarkable azimuthal variability and inhomogeneity due to the effect of RFI removal in these specific azimuths.

The result of the mitigation solution, reported in Figure 7.25, are validated by comparing the reflectivity product of a C-band radar operating at 5.4GHz, thus unaffected by communication systems transmitting in the unlicensed 5.6GHz band, covering the same precipitation area. In Figure 7.28, the reflectivity product of Monte Lema (CH) of 22 November 2022 at 08:50 UTC, same time of the study case, is displayed. The precipitation area observed by Bric della Croce

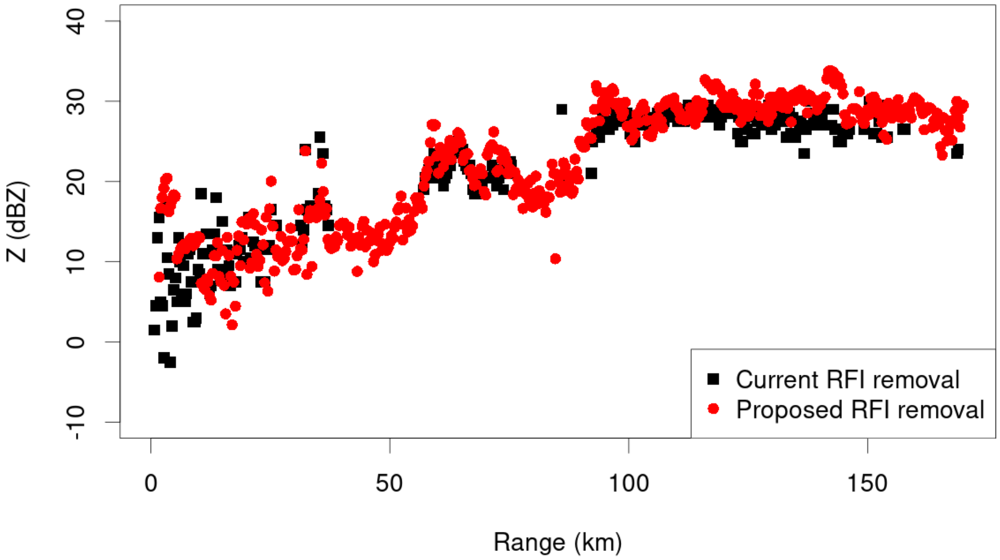

Figure 7.27: Reflectivity over range of azimuth 85° of PPIs reported in Figure 7.26: the black squares represent the Z computed by the current mitigation tool in the radar signal processor and the red dots the Z computed from the IQ data processed by the proposed mitigation solution.

radar is marked by the red circle. The radial lines visible in Figure 7.25 at azimuth 75°, 85° and 115° are not present in the Monte Lema reflectivity, pointing out the those data where not related to weather echoes but to RFI.

Furthermore, Figure 7.29 shows the reflectivity maps computed by SQI filtering at the radar signal processor (top), the reflectivity acquired by the Monte Lema (CH) radar and the Z computed after the proposed mitigation solution. The Swiss radar, considered as reference since unaffected by RFI, detects precipitation in the East side of the Bric della Croce domain, corresponding to the area between Milan and Piacenza (labels MI and PC in the figure). The SQI filtered Z does not show weather echoes in some azimuths of the East domain due to the RFI removal. The proposed mitigation solution, bottom panel of Figure 7.29, is able to preserve the precipitation information and to mitigate the impact of electromagnetic interference. In fact, in that aforementioned area, the reflectivity patterns and values are comparable to those acquired by the Monte Lema (CH) radar. The metric to quantitatively evaluate the method performance is the Interference to Signal Ratio

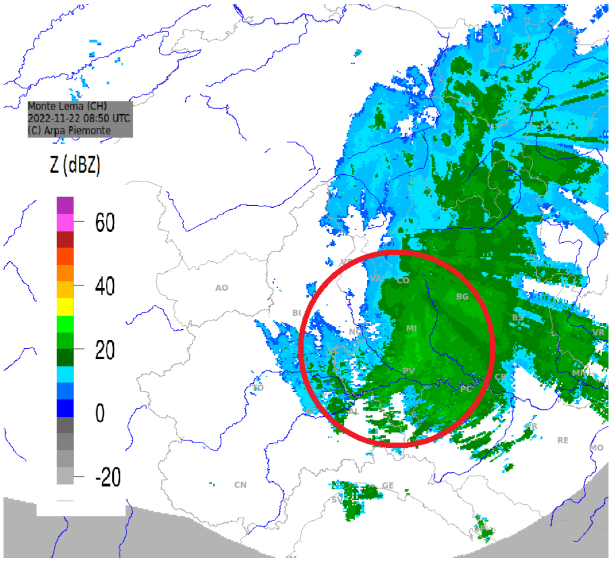

Figure 7.28: Monte Lema (CH) reflectivity product of 22 November 2022 at 08:50 UTC. The study case precipitation is marked by the red circle.

(ISR) defined as the ratio of the power of the interfering signal in a given pulse i and the average of weather echoes power, as reported in Equation 7.14. Since this metric is used to valuate the mitigation solution, the $ISR_{mitigation}$ is computed as difference of the processed signals ISR and the received signals ISR.

$$ISR_i = \frac{P_{RFI}}{< P_{weather} >} \tag{7.14}$$

$$ISR_{mitigation} = ISR_{processed} - ISR_{received} \tag{7.15}$$

For every pulse identified as affected by interference, the ISR is computed on the mitigated and raw signals. In Figure 7.30, the histogram of the ISR difference, computed on the previously described study case, is shown. Depending on the interference power respect to the weather echoes power, the proposed mitigation solution, in average, decreases the impact of the interfering signal from 5dB to 15dB. In some pulses, where a harmful interference is removed, the ISR difference can be as low as -20dB to -35dB. This quantitative estimate highlights the capability of the proposed method to mitigate the impact of interfering signals during weather events.

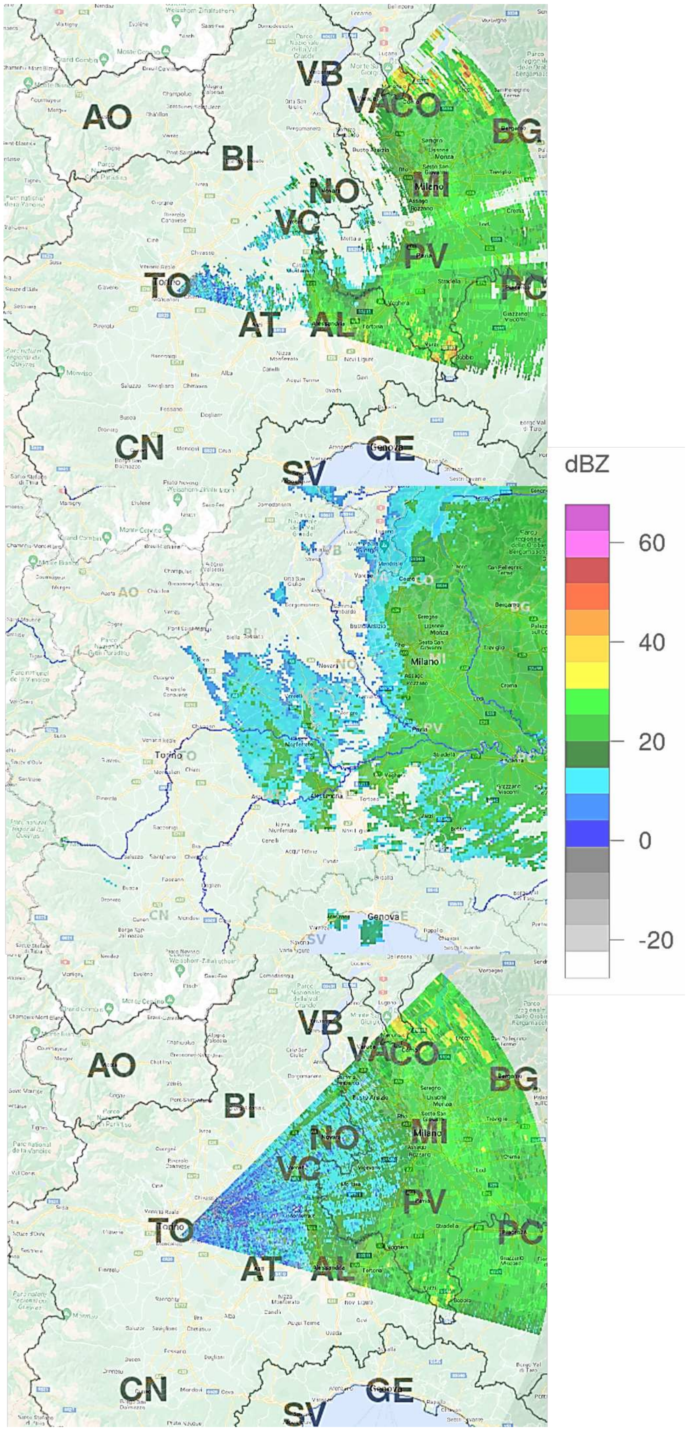

Figure 7.29: Validation of the proposed mitigation solution in precipitation. From top: Z computed by the radar signal processor (SQI filtering only), Z from Monte Lema radar as reference, Z computed after the proposed mitigation. Note that Monte Lema radar detects precipitation in the Est side of the Bric della Croce radar domain, where the SQI filtered Z does not contains weather echoes.

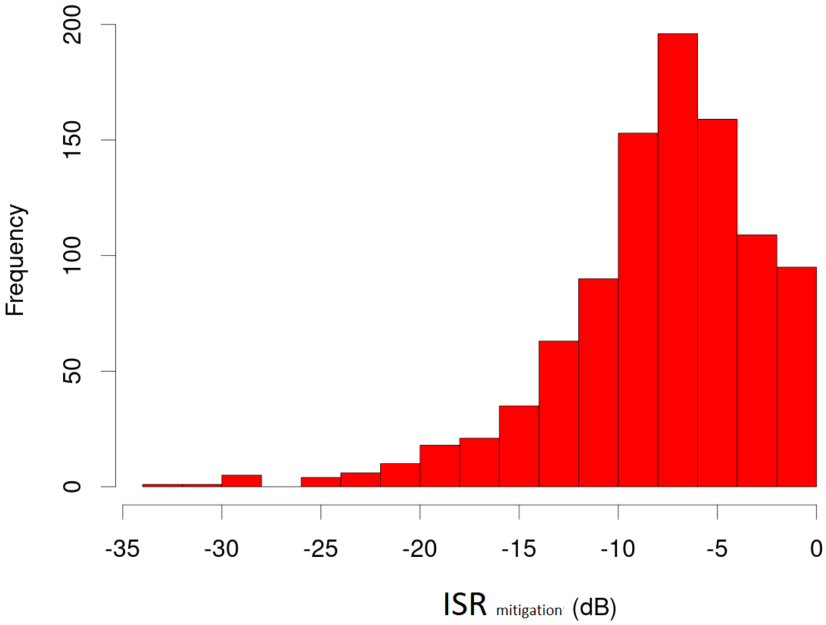

Figure 7.30: Difference of Interference to Signal Ratio computed on the processed and received signals of the study case. This metric applied to evaluate the mitigation performance.

7.6 Mitigation procedure

In this section the mitigation technique described in the previous pages is summarized to define a procedure that can be easily implemented by weather services or weather radar managers. In case the raw data at the signal processor level are not accessible, the mitigation technique based on the image processing can be implemented (see Chapter 6). The proposed procedure consists in three steps: RFI signal acquisition, thresholds adjustment in the mitigation code and mitigation tool implementation. It is suggested to collect IQ data of interfering signals in clear sky condition over several azimuths and elevations, even if the lowest elevation is commonly the most affected by RFI. This dataset is required to investigate the interfering signal modulation and polarization features on which the mitigation tool is based. Based on the retrieved features, thresholds of polarization and modulation can be adjust to fit the collected data. The code than can be implemented in the radar signal processor during the IQ processing to generate radar products.

Chapter 8

Summary and future developments

This presented dissertation has two main goals: (i) to collect evidence prevent the new installation or changes of telecommunication towers operating in a given radar band during the telecommunication authorization process, and (ii) to remove and mitigate the effect of RFI in the radar products. The first goal has been reached by implementing the an algorithm which can be used in the telecommunication authorization processes, according to national and regional laws. The proposed method identifies the towers that may interfere with a given radar. It has been tested and implemented in the database of electromagnetic sources of Piemonte region (Italy) and it selects the sources according to the criteria discussed in Chapter 4. The results of the proposed model have been verified during field measurements where the likely interfering sources, output of the proposed method, have been identified by their SSIDs.

The second goal of RFI mitigation is discussed and implemented in two different ways: (i) as image processing for radar product, in case the national weather service, which manages an interfered radar, cannot operate at the radar signal processor level, and (ii) as IQ analysis in the radar signal processor. The first method have good performances when the RFIs are not overlapped with meteorological echoes. In the second method, the interfering signals are removed and the radar echoes are reconstructed even in case of overlapping with weather echoes. In order to perform this second method, the features of the interfering signals need to be investigated. At C-band the interfering sources are identified decoding the transmitted SSID and BSSID, since the nature of the sources is known (WLAN, RLAN). Instead, at X-band, the RFI are a new nuisance for these radars. The interfering signals have been acquired by the mobile X-band radar managed by Arpa Piemonte and also using the Keysight FieldFox vector spectrum analyzer. Further actions to identify the sources will be taken in collaboration with the National Regulation Authority.

The interfering signals analysis has shown specific features in terms of modulation and polarization which are used to discriminate the IQ data related to RFI. The proposed mitigation tool acts on IQ pulses to perform analysis on the acquired data to identify likely interfering signals. The analysis is performed by cluster areas over the range axes, corresponding to the radial distance. If a cluster meets the RFI features, the corresponding IQ data for both polarization channels are set as invalid and removed in the following elaborations. The aim of the proposed algorithm is to restore the echoes that are overlapped with interfering signals. So, where the IQ data are recognized as interference the algorithm reconstructs the likely radar echo by averaging the previous non-interference data. Finally, the IQ data matrix can be used to generate radar products. The algorithm has been tested during clear sky conditions with good performances. The execution time on a commercial laptop is in the order of few seconds which allows to implement the proposed mitigation tool in the radar signal processor without any additional processing delay.

The C-band radar was deployed to collect IQ data during precipitation. The precipitation areas over the East side of Piemonte region during the 22 November 2022 have been selected to test the mitigation solution. The algorithm is applied to the raw IQ data to remove interfering signals and to reconstruct the removed data. The radar reflectivity is computed from the processed IQ data and it is compared to the operational radar Z product. In this study case, to assess the presence of RFI, the reflectivity in the precipitation area is compared to the observation of a C-band radar operating out of the 5.6GHz band. The Swiss radar of Monte Lema has been selected as reference since it covers the same precipitation area. The interfering signals are properly detected and removed. The missing data in the pulses are computed by smoothing from adjacent range gates and pulses. Actually, removing only the interfering signals inside the radar pulse the proposed solution is able to preserve the meteorological echoes which lead to a better estimate of the reflectivity values, especially in case of weak echoes (i.e. light rain, drizzle or ice-phase phenomena). In fact, where electromagnetic interference is overlapped with weather echoes, the spatial reflectivity pattern and values, computed after the proposed mitigation, are comparable to those acquired by the Monte Lema (CH) radar, while the SQI filtered reflectivity does not show precipitation.

The Interference to Signal Ratio (ISR) is considered the metric to quantitatively evaluate the mitigation performance as ISR difference between processed and received signals. The proposed mitigation solution, in average, decreases the impact of the interfering signal from 5dB to 15dB. In some pulses, up to 20dB suppression can be achieved. This quantitative estimate highlights the capability of the proposed method to mitigate the impact of interfering signals in case of weather events.

Future works will be conducted on advanced signal processing thecniques for the acquired IQ data to better identify the RFI features. The proposed mitigation tools will be also implemented in the X-band radar, after the radar maintenance. Finally, the algorithm will be applied on radar data in case of low reflectivity events, such as snow, to evaluate its performances.

Bibliography

[1] Radio Regulations. Itu. *Geneva, Switzerland*, 2012.

[2] V. N. Bringi and V. Chandrasekar. *Polarimetric Doppler Weather Radar, principles and applications*. Cambridge University Press, 2001.

[3] Robert Palmer, David Whelan, David Bodine, Pierre Kirstetter, Matthew Kumjian, Justin Metcalf, Mark Yeary, Tian-You Yu, Ramesh Rao, John Cho, et al. The need for spectrum and the impact on weather observations. *Bulletin of the American Meteorological Society*, pages 1–13, 2021.

[4] IATA. Problem statement - 5g interference with radar altimeter frequency band. In *ICAO Meeting, Montreal, 2020*.

[5] Elena Saltikoff, John YN Cho, Philippe Tristant, Asko Huuskonen, Lynn Allmon, Russell Cook, Erik Becker, and Paul Joe. The threat to weather radars by wireless technology. *Bulletin of the American Meteorological Society*, 97(7):1159–1167, 2016.

[6] Suzan Bayhan, Gürkan Gür, and Anatolij Zubow. The future is unlicensed: Coexistence in the unlicensed spectrum for 5g. *arXiv preprint arXiv:1801.04964*, 2018.

[7] Stephen Itschner and Xin Li. Radio frequency interference (rfi) detection in instrumentation radar systems: a deep learning approach. In *2019 IEEE Radar Conference (RadarConf)*, pages 1–5, 2019.

[8] Jiapeng Yin, Peter Hoogeboom, Christine Unal, and Herman Russchenberg. Radio frequency interference characterization and mitigation for polarimetric weather radar: A study case. *IEEE Transactions on Geoscience and Remote Sensing*, 60:1–16, 2022.

[9] Qing Cao and Michael Knight. Mitigation of radio frequency pulse interference on dual-pol weather radar. In *American Meteorological Society 99th annual meeting*, pages 6–10, 2019.

[10] Renzo Bechini and V Chandrasekar. A semisupervised robust hydrometeor classification method for dual-polarization radar applications. *Journal of Atmospheric and Oceanic Technology*, 32(1):22–47, 2015.

[11] Ivan ARIAS and V. CHANDRASEKAR. Cross validation of the network of ground-based radar with gpm during the remote sensing of electrification, lightning, and mesoscale/microscale processes with adaptive ground observations (relampago) field campaign. *Journal of the Meteorological Society of Japan. Ser. II*, 99(6):1423–1438, 2021.

[12] International Telecommunication Union. Itu resolution 229. 2003.

[13] Martin Cave and William Webb. *Spectrum management: using the airwaves for maximum social and economic benefit*. Cambridge University Press, 2015.

[14] M. Vaccarono, V. Chandrasekar, R. Bechini, R. Cremonini, P. P. Alberoni, and F. Pizzotti. Interferenze elettromagnetiche nei sistemi radar meteorologici: le esperienze di arpa piemonte ed arpae emilia-romagna. In *RadMet.2021 - IV Italian National Congress of Radarmeteorology*, 2021.

[15] John Canny. A computational approach to edge detection. *Pattern Analysis and Machine Intelligence, IEEE Transactions on*, PAMI-8(6):679–698, Nov 1986.

[16] Richard O. Duda and Peter E. Hart. Use of the hough transformation to detect lines and curves in pictures. *Commun. ACM*, 15(1):11–15, Jan 1972.

[17] Athanasios Papoulis. Random variables and stochastic processes. 1965.

[18] Mao Tian. Radiation characterization of slant polarization antennas. *Microwave Journal*, 42(5):312–316, 1999.

[19] Shengrong Lu, Yang-Han Lee, Yi-Lun Chen, Hsien-Wei Tseng, Chun-Chi Chen, Jhih-Hong Chen, Hen-Wai Tsao, and Jing-Shown Wu. Application of zadoff–chu sequences in through-

put balancing control of self-organizing long term evolution communication network. *Sensors and Materials*, 33(5):1619–1629, 2021.